Alma Mater Studiorum – Università di Bologna

DOTTORATO DI RICERCA IN

Scienze Ambientali: tutela e gestione delle risorse naturali

Ciclo _XXIII_

Settore Concorsuale di afferenza: ___04/A4_____

Settore Scientifico disciplinare:____GEO/12_____

TITOLO TESI

Sea-level climate variability in the Mediterranean Sea

Presentata da: __**Antonio Bonaduce**_____

Coordinatore Dottorato
Prof. Enrico Dinelli

_____

Relatore
Prof.ssa Nadia Pinardi

_____

Esame finale anno 2012

Sea-level climate variability in the Mediterranean Sea

Student: Antonio Bonaduce

Advisor: Prof. Nadia Pinardi

Environmental Science

Alma Mater Studiorm-University of Bologna

A thesis submitted for the degree of

Doctor of Philosophy

2011/2012

Contents

List of Figures

List of Tables

Abbreviations and Acronyms

h_{IB} Inverse Barometer Effect

$AVISO$ Archiving, Validation and Interpretation of Satellite Oceanographic Data

$CANTICO$ Climate and ANthropogenic drivers and impacts for the TunisIan COastal areas

$EGWs$ External Gravity Waves

EKE Eddy Kinetic Energy

$EuroGOOS$ European Global Ocean Observing System

GIA Glacial Isostatic Adjustment

$GMSL$ Global Mean Sea Level

$GOOS$ Global Ocean Observing System

$ICZM$ Integrated Coastal Zone Management

$IPCC$ Intergovernamental Panel on Climate Change

$ISPRA$ Italian Institute for Environmental Research and Protection

MFS Mediterranean Forecasting System

OPA Mean Sea Level Equations

$MSLP$ Mean Sea Level Pressure

NAO North Atlantic Oscillation

$NCEP$ National Center for Atmospheric Research

$NCEP$ National Centers for Environmental Prediction

$NEMO$ Nucleus for European Modelling of the Ocean

$OGCM$ Ocean General Circulation Model

OPA Ocean PArallelise code

SDE Stochastic Differential Equation

TP Topex/Poseidon

$UNFCCC$ United Nations Framework Convention on Climate Change

Chapter 1

Introduction

Sea-level variability is characterized by multiple interacting factors described in the Fourth Assessment Report (Bindoff *et al.*, 2007) of the Intergovernamental Panel on Climate Change (IPCC) that act over wide spectra of temporal and spatial scales. Over time scales ranging from centuries to millenia, a leading role is played by very slow and continuous processes such as lithospheric and mantle deformation due to the the melting of ice sheets inducing the process of glacio-isostatic adjustment (GIA) (Spada *et al.*, 2006), giving a contribution to sea-level trends. Sea-level changes at decadal and interannual time scales are due to density and water-mass distribution variations in the ocean, driven by wind, atmospheric pressure (Chapters 2 and 5) and heat and water fluxes. Wind stress and pressure produce, through mechanical stress, a displacement of the water mass involving sea-level variations due to barotropic displacement of the water column. Variations of temperature and salinity due to heat and water fluxes tend to modify the density structure of the water column (the steric effect), which in turn changes the height of the water column.

Sea-level changes in the global ocean are mainly driven by water flux (precipitation, evaporation, river run-off and ice melting), which represents the sea-level variability component due to mass variations, and by heat flux, which accounts for the steric component (Chapter 4). The most recent study on global sea level estimates a global sea-level rise of $3.2 \pm 0.4\ mm\ yr^{-1}$ from satellite altimetry and $2.8 \pm 0.8\ mm\ yr^{-1}$ from in-situ data during the period between 1993 and 2009, while the linear trend obtained from Global Mean Sea Level (GMSL) recon-

struction (Chapter 3) during the period from 1900 to 2009 is $1.7 \pm 0.2\ mm\ yr^{-1}$ (Church & White, 2011).

At the regional scale, lateral fluxes also contribute to sea-level variability, adding complexity to sea-level dynamics (Chapter 4). In the case of the Mediterranean, Marcos & Tsimplis (2007) estimates a trend of $0.9 \pm 0.4\ mm\ yr^{-1}$ from in-situ data for the period 1960-2000. The first Mediterranean sea-level reconstruction was realized by Calafat & Gomis (2009) for the period 19452000, giving a trend of $0.7 \pm 0.2\ mm\ yr^{-1}$.

In Church *et al.* (2010) sea-level variability and changes are defined as manifestations of climate variability and change. The European Environmental Agency (EEA) defines sea level as one of most important indicators for monitoring climate change, as it integrates the response of different components of the Earths system and is also affected by anthropogenic contributions (EEA, 2011). This last aspect can be explained by human activities that contribute to groundwater storage. Human-induced sea-level rise is mainly due to the concentration of the world population along the coasts: the development of mega-cities and the concentration of human activities in these areas have lead to wetland loss and subsidence mainly as a result of the overuse of groundwater (Nichols, 2004). This process is responsible for increased salt-water intrusion into aquifers (Nicholls & Mimura, 1998), thus establishing a positive feedback between the exploitation of resources and environmental impact. High demographic density in coastal areas tends to amplify the effects of extreme events such as hurricanes and storm surges, which are the main drivers of coastal flooding events (such as Katrina along the Louisiana coast in 2005).

In this context, Integrated Coastal Zone Management (ICZM) as promoted since 1995 by the Barcelona Convention assumes increasing importance. The United Nations Framework Convention on Climate Change (UNFCCC)(COP17, Durban, South Africa, 2011) underlines the importance of integrated management of coastal zones (Article 4 of the UNFCCC [1]) as an adaptation to the impact of climate change and the uncertainty it causes.

The balance between the different sea-level contributions represents an important source of uncertainty, involving stochastic processes that are very difficult to

[1] UNFCCC web portal: full text of the Convenction.

describe and understand in detail, to the point that they are defined as an enigma in Munk (2002). Sea-level rate estimates are affected by all these uncertainties, in particular if we look at possible responses to sea-level contributions to future climate.

The study of historical sea-level data is a means for understanding and quantifying these many uncertainties (Church *et al.*, 2010). The development over the last 20 years of satellite altimetry has radically improved our capacity to understand sea-level dynamics at the global (Cabanes *et al.*, 2001) and regional (Pujol & Larnicol, 2005) scales.

The advent of operational oceanography has had a major impact on numerical models of large-scale circulation (Oddo *et al.*, 2009), as they can now be accurately calibrated with observed data. The development of real-time monitoring systems, such as the Global Ocean Observing System (GOOS) and EuroGOOS for the European seas, allows the realization of high-resolution global (Masina *et al.*, 2004) and regional (Adani *et al.*, 2010) ocean re-analysis, realized with a relevant number of observations and calibrated models. Both model calibration with observed data and the continuous improvement of the physical representation of oceanic processes allow models to simulate the sea-level variability at global and regional scales realistically.

The research strategy adopted in this work to approach such an interesting and challenging topic has been to develop an objective methodology to study sea-level variability at different temporal and spatial scales, applicable in each part of the Mediterranean basin in particular, and in the global ocean in general, using all the best calibrated sources of data (for the Mediterranean): in-situ, remote-sensig and OGCM data. In-situ data time series cover the last century with monthly records, while altimeter data is available only since the beginning of the nineteen-nineties. The balance between sea-level observational data availability, used also to validate numerical model outputs, and the temporal scales of the main sea-level change drivers (i.e., GIA, density and water-mass distribution variations), has led to structuring this study in such a way as to look at sea-level variability over temporal scales that range from monthly to decadal up to multidecadal.

The global objective of this work was to achieve a deep understanding of all of the components of the sea-level signal contributing to sea-level variability,

tendency and trend and to quantify them.

Chapter 2 presents a study of sea-level variability in the Mediterranean basin at a decadal time scale using in-situ and remote sensing data. Sea-level variability is investigated at a centennial time scale, using sea level reconstruction techniques in Chapter 3. Chapter 4 describes the fully consistent Mean Sea Level Equation and its application in the Mediterranean basin. Chapter 5 presents a study of the atmospheric pressure effect on the sea-level signal using numerical models of large-scale circulation and in-situ data.

Chapter 2

Low frequency sea-level variability over decadal period

2.1 Sea level from observational instruments

The problem of rising global sea levels has attracted a great deal of attention over the past ten years. The difficulties in estimating a reliable rate of sea-level change are due mainly to two categories of factors: the dataset used (whether tide gauges or satellite altimetry) and the period for which the rate is estimated. Before the beginning of what is known as the satellite era (1992 onwards) and the availability of a certain number of years of data, sea-level trends were estimated using long time series of tide-gauge data. Today, the availability of satellite altimetry data spanning a period of under 20 years means that trends are also estimated over shorter periods. Thus, differences in the dataset and time period considered means that many different sea-level rise values are given both at the global and regional scales.

Global sea-level trends are dominated by the steric component and ocean mass increase (Levitus *et al.*, 2000; Domingues *et al.*, 2008). Coastal and island tide-gauge data show that sea levels rose by just under 20 cm between 1870 and 2001, with an average rise of 1.7 $mm\ yr^{-1}$ for the period 1950-2000 (Holgate, 2004). The first global sea-level reconstruction (Church *et al.*, 2004a), covering the period 1950-2000 is an agreement with the previous value, proposing a global sea-level

rise of 1.8 ± 0.3 $mm\ yr^{-1}$ between 1950 and 2000. Extending the reconstruction period to between 1870 and 2004, Church (2006) found that the total global mean sea-level rise is 195 mm, an average of 1.44 $mm\ yr^{-1}$, and that for the 20th century the rise is about 160 mm at a rate of 1.7 ± 0.3 $mm\ yr^{-1}$, also considering in the error the effect of glacial isostatic adjustment (GIA). By dividing the analysis period into two sub-periods, 1870-1935 and 1936-2001 (change of slope ∼ 1930), and performing linear regressions on the two halves of the records,Church (2006) found that the slopes are 0.71 ± 0.40 and 1.84 ± 0.19 $mm\ yr^{-1}$ respectively, implying an acceleration of 0.017 ± 0.007 $mm\ yr^{-2}$ in the last 65 years.

Since the end of 1992, near-global measurements of sea levels (between 60° N and 60° S) made by high-precision satellite altimeters have been available. In Cazenave *et al.* (2003) Topex/Poseidon data indicate global average sea level has risen at 3.2 ± 0.4 $mm\ yr^{-1}$ between 1993 and 1998 and 2.4 ± 0.1 $mm\ yr^{-1}$ between 1992 and 2001. Cabanes *et al.* (2001) also used Topex/Poseidon data, and applied a low pass filter at each grid point to remove short-period (≤1 year) signals; a rate of global sea-level rise of 2.5± 0.2 $mm\ yr^{-1}$ between January 1993 and December 2000 was found. In the sea-level rate values estimated in both Cabanes *et al.* (2001) and Cazenave *et al.* (2003), the GIA contribution is not subtracted. According to Leuliette *et al.* (2004), the GIA should be subtracted from the global average trend of 2.8 ± 0.4 $mm\ yr^{-1}$, found using Topex/Poseidon and Jason data for the period 1992-2004, with a mean rate value of - 0.3 $mm\ yr^{-1}$ (Douglas & Peltier, 2002).

In the Mediterranean, atmospheric pressure has a strong influence on sea-level trends (Tsimplis *et al.*, 2005; Marcos & Tsimplis, 2007; Gomis *et al.*, 2008). Tsimplis *et al.* (2005) calculated trend, corrected for meteorological effects, using the 9 longest time series of tide-gauge station data available in the Mediterranean basin (located in the western basin and Adriatic Sea). For the period 1958 to 2001, a sea-level rise varying from ∼ 0.3±0.4 $mm\ yr^{-1}$ to ∼ 1.3±0.4 $mm\ yr^{-1}$ was found, though between 1993 and 2001 the tide-gauge stations in the Adriatic show residual trends of 5 to 10 $mm\ yr^{-1}$.

In Marcos & Tsimplis (2007) the data of 11 tide-gauge stations (located in the western part of the basin as well as in the Adriatic) were used to compute the basin mean sea-level trend between 1960 and 2000 (∼ 0.9 ±0.4 $mm\ yr^{-1}$), taking

the atmospheric forcing effect into consideration(- 0.7±0.1 $mm\ yr^{-1}$) and correcting the residual trend for post-glacial rebound processes (- 0.2±0.3 $mm\ yr^{-1}$). Marcos & Tsimplis (2008), using 21 tide-gauge stations with more than 35 years of data, estimated the sea-level trends corrected for meteorological effects for the period 1960-2000 underlying the sea-level trend variability found in the basin: between 2.0 and 2.2 ± 0.4 $mm\ yr^{-1}$ along the northern Spanish coast, between 0.0 ± 0.2 and 0.7 ± 0.2 $mm\ yr^{-1}$ in the western basin and between 0.4 ± 0.3 and 0.9 ± 0.3 $mm\ yr^{-1}$ in the Adriatic.

Klein & Lichter (2009) divided the tide-gauge time series into two sets of records (up to 1959 and from 1960 onwards), finding that trends (obtained calculating linear regressions on the time series) in the Mediterranean over the 20th century have been quite similar to the average global sea-level rise (0.5 - 2.5 $mm\ yr^{-1}$), but for the sub-period 1990-2003 (filtering out the atmospherical contribution from the data) in most of the Mediterranean (twenty-one out of twenty-nine stations analysed), the trends are 5 to 10 times higher than the 20th century mean.

Cazenave *et al.* (2002), using Topex/Poseidon data from 1993 to 1998 and ERS-1/2 data from 1992 to 1996 (seasonal signal removed and low pass filter applied at each grid point), estimated a mean basin sea-level rise for the period 1993 - 1998 of 7 ± 1.5 $mm\ yr^{-1}$. In their previous study Cazenave *et al.* (2001), using Topex/Poseidon data only (filtered as in Cazenave *et al.* (2002)) from 1993 to 1999, it was shown how the Western basin (5 to 10 $mmyr^{-1}$) and the Levantine Basin (average rates of ∼ 20 $mmyr^{-1}$) have been continuously rising over this period, while the Ionian Basin shows evidence of sea-level falls reaching a rate of -10 $mmyr^{-1}$, marking the start of an important change in the circulation observed in this basin (Demirov & Pinardi, 2002).

The first sea-level reconstruction for the Mediterranean Sea to use both satellite and tide-gauge data was realized by Calafat & Gomis (2009) for the period 1945-2000, estimating the basin-averaged trend over 55 years at 0.7 ± 0.2 $mm\ yr^{-1}$, finding, even in this case, differences between the various sub-basins: a positive trend (1.2 $mm\ yr^{-1}$) is obtained for the Ionian Sea, whereas a negative trend was observed for the previous period, with a negative peak in the Levantine Basin (- 0.5 $mm\ yr^{-1}$, south-east of Crete). The results between 1993 and 2000

are significantly different: positive trend values above 10 $mm\ yr^{-1}$ were found in the eastern Mediterranean and smaller rates (less than 5 $mm\ yr^{-1}$) in the western Mediterranean. A marked negative trend of more than -15 $mm\ yr^{-1}$ is observed in the Ionian.

Looking at this marked spatial-temporal variability of the sea level in the basin, one of the specific purposes of this work is to describe and understand the sea-level variability in the Mediterranean using all available best-calibrated observational data-sets for a common period in order to obtain consistent results. To acheive this objective, two sea-level observational datasets have been considered, comparing 18 years of data (1993 - 2010): 1) for tide-gauges, the *Revised Local Reference* data-set, provided by the *Permanent Service for Mean Sea Level* (PSMSL); 2) the *Delayed Time Sea Level Anomaly* (DT SLA) data-set from the AVISO agency.

A second objective of this analysis is to evaluate how satellite altimetry data resolve the sea level near the coasts, in order to understand if the offshore sea-level altimetry signals are representative of the local sea level recorded by tide-gauges along the basin coasts.

The reminder of this chapter is organized as follows. In Section 2 we select the data to be used in the sea-level signal analysis. The method used to compare the tide-gauge and satellite altimetry datasets is described in Section 3. The coastal sea level from tide gauges and the open-ocean sea level from altimetry are compared and analysed in Section 4: first we look at the correlation between the two datasets and at the sea-level trends estimated from both; in the second part of this section, the sea-level trend spatial and temporal variability is analysed using satellite altimetry data. All the results are summarized in Section 5.

2.2 Data

2.2.1 In-situ data

The PSMSL data set is available from around 1900 and up to 2008 but has a discontinuous spatial distribution and a significant gap in the southern part of the basin (North Africa). In-situ sea-level data are provided by the PSMSL as

monthly means. In particular, attention will be i focused on the Revised Local Reference (RLR) dataset (Woodworth & Player, 2003), which, for scientific purposes, results as superior to simple metric data. The PSMSL reduces all the records collected to a common datum for the analysis of time series. This reduction is performed using the tide-gauge datum history and a common denominator of 7000 mm below the average sea level (Klein & Lichter, 2009) , in order to avoid negative numbers in the resulting RLR monthly and annual mean values.

In the Mediterranean basin there are 63 tide-gauge stations of the RLR dataset covering the period between 1993 an 2010 (satellite time window). Only half of these show complete time series: in particular, 31 stations have at least 70 % of the complete time series during the analysis period. In Figure 2.1 the spatial distribution of tide-gauge stations over the basin is shown: green points represent the stations with the most complete time series. These stations represent the target areas selected for this study (Table 2.2).

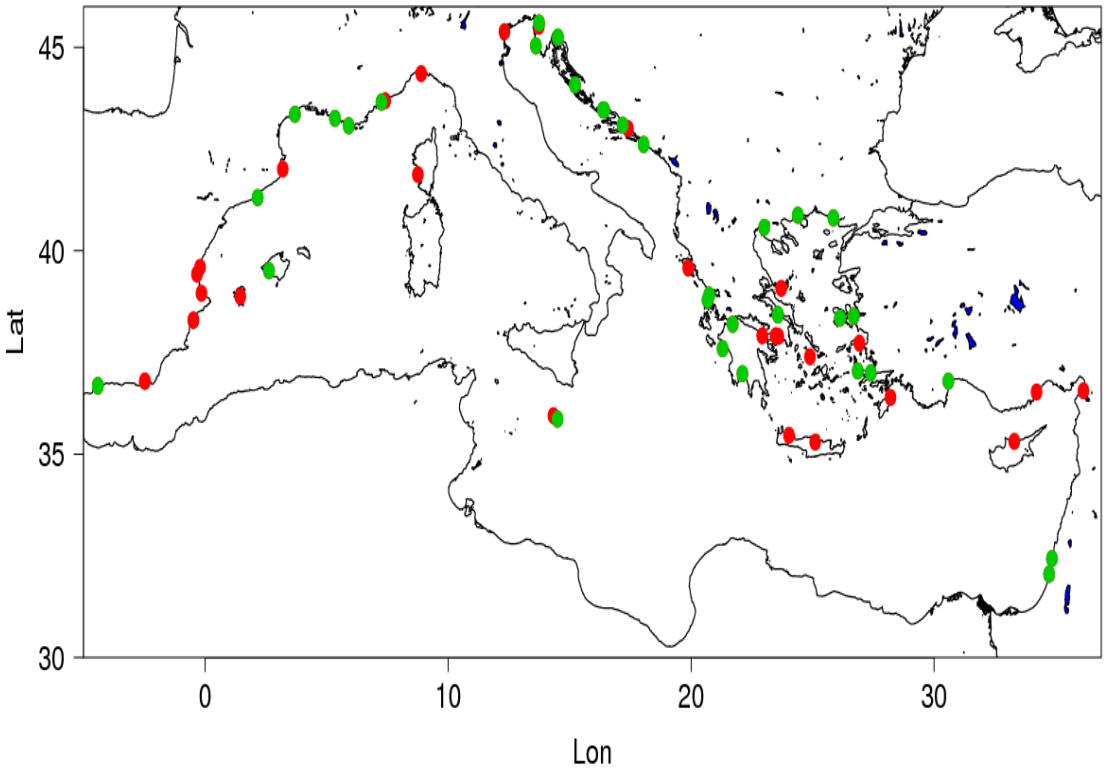

Figure 2.1: Tide-gauge station distribution in the Mediterranean. Green points represent the tide-gauge stations having the most complete time series (at least 70 %) during the period between 1993 and 2010.

2.2.2 Remote-sensing data

The specific satellite Sea Level Anomaly (SLA) fields used in this study are described by Pujol & Larnicol (2005). Data are interpolated over a regular grid every 7 days using an objective method combining the different altimeter missions (Ducet *et al.*, 2000; Pujol & Larnicol, 2005). It uses a debiasing filter for along-track long wavelength (Traon *et al.*, 1998, 2003) and the subtraction of the inverse barometer effects as well as wind and tidal effects, ionosphere correction and wet and dry troposphere corrections (see Table **??**), electromagnetic bias, instrumental corrections (altimeter bias and onboard oscillator drift). We used

a homogeneous data set based on 6 satellites: Topex/Poseidon (September 1992 to October 2005) , Jason-1 (August 2002 onwards), Jason-2 (January 2009 onwards), ERS-1 (October 1992 to May 1995), ERS-2 (May 1995 to June 2003), Envisat (June 2003 onwards). Starting with different satellite along-track data, the different SLA signals of the satellite missions named above are combined and interpolated through an objective analysis technique on a regular grid (Ducet *et al.*, 2000) with a horizontal resolution of $1/8^\circ$ ($\sim$ 13 km). Along-track data are truncated at a distance of $\sim$ 30 km from the coast to avoid reflection of the radar signal from the land: this value has been considered as the distance from the coast to define the minimum area around each tide-gauge position for data intercomparison. Data has been averaged monthly in order to use the same temporal resolution as the in-situ data.

	T/P	J1	J2	E1	E2	En
Data period	1992-2005	2002-on*	2009-on	1992-1995	1995-2003	2003-on
Ionosfere	dual frequency altimeter range measurements (Topex), from Doris (Poseidon)	dual frequency altimeter range measurement		Bent model		dual frequency altimeter range measurement
Wet Troposhere	TMR*	ECMWF*		MWR*	applied	ECMWF
Dry Troposhere	ECMWF	ECMWF		ECMWF		ECMWF
Inverse Barometer	ECMWF	ECMWF		ECMWF		ECMWF
Ocean Tide	applied					
Pole Tide	Wahr (1985)					
Solid Earth Tide	Elastic response to tidal potential (Cartwright & Edden, 1973)					
Loading Tide	applied					

Table 2.1: Satellite altimetry data. Corrections applied to the AVISO satellite altimetry Delayed Time products (modified from (AVISO, 2010)). Missions: Topex/Poseidon (T/P), Jason-1/2 (J1; J2), ERS-1/2 (E1; E2), Envisat (En); *on=ongoing. *TOPEX Microwave Radiometer (TMR); *Microwave Radiometer (MWR); *European Centre for Medium-Range Weather Forecasts (ECMWF) .

2.3 How to compare remote-sensing and in-situ data

In order to compare satellite *SLA* and tide-gauge sea-level data we will start defining the sea-level anomaly (*SLA*) signal. The *SLA* is given by the difference between the sea level (η_{sat}) and its mean (η_{sat}^{mean}), calculated over a reference period running from 1993 to 1999 (Pujol & Larnicol, 2005). We assume that η_{sat}^{mean} contains the geoid and the mean dynamic topography and we write:

$$sla_{sat}(x, y, t) = \eta_{sat}(x, y, t) - \eta_{sat}^{mean}(x, y) \tag{2.1}$$

where $\eta_{sat}(x, y, t)$ can be defined as:

$$\eta_{sat}(x, y, t) = \eta_{sat}^{st}(t) + \eta_{sat}^{mean}(x, y) + \eta_{sat}^{var}(x, y, t) \tag{2.2}$$

where $\eta_{sat}^{st}(t)$ is the sea level steric component defined as a time-dependent function only (Mellor & Ezer, 1995), and $\eta_{sat}^{var}(x, y, t)$ is the time- and space-dependent dynamic component. From 2.3 it is evident that if the time average is defined for the same period as η_{sat}^{mean}, $\langle \eta_{sat}^{st} \rangle = 0$, where the brackets indicate the time average.

We define the steric component of satellite sea level as:

$$[[sla_{sat}(x, y, t)]] = \eta_{sat}^{st}(t) \tag{2.3}$$

where the square brackets indicate area average. $\eta_{sat}^{st}(t)$ is monthly mean frequency and we obtain the seasonal steric signal, which we call η_{sat}^{st}, shown in Fig.2.2, during the period from 1993 to 2010.

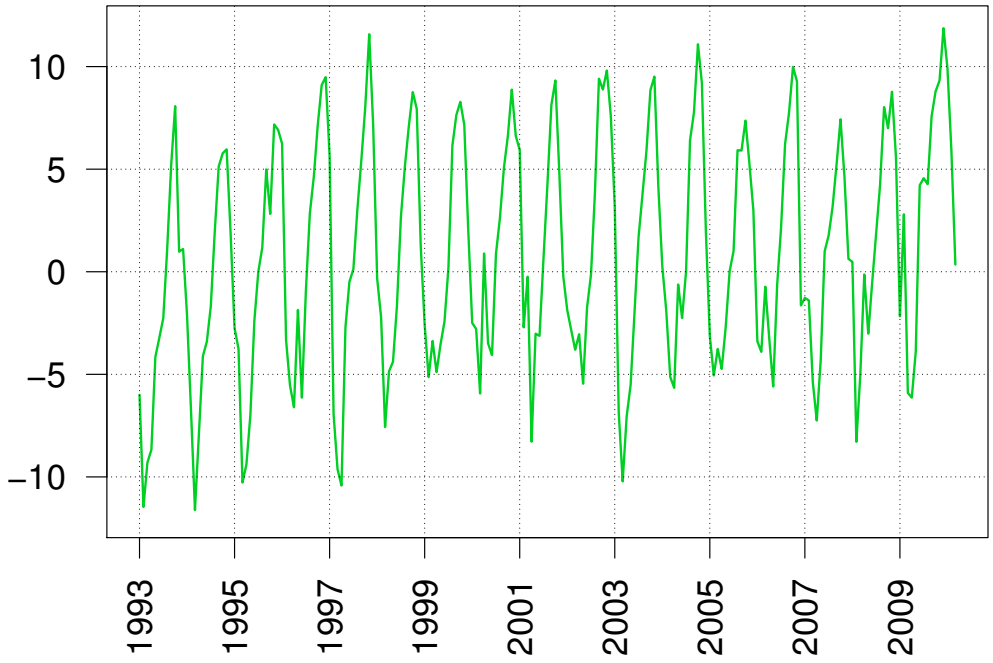

Figure 2.2: Interannual steric component $\eta^{st}_{sat}(t)$ of satellite altimetry data over from 1993 to 2010; y-axis values expressed as $[cm]$.

The steric effect is considered as a time-dependent variable only, following the definition of Greatbatch (1994) and Mellor & Ezer (1995). It assumes that the local elevation change exclusively due to density change is rapidly distributed over the entire domain with a time scale proportional to the basin lateral scale and the barotropic wave speed (Mellor & Ezer, 1995). This definition assumes great importance in a regional basin, where lateral advection can arise variations of density not associated to real variations of the external forcings (i.e., heat and water fluxes; Greatbatch, 1994), which in turn should be the source of steric variations considered as anomalies of water-column density (Mellor & Ezer, 1995). This effect is also minimized considering the steric signal as a basin-averaged time-dependent variable.

To validate the steric signal obtained, the satellite steric term η_{sat}^{st} has been compared with the steric signal obtained subtracting the satellite gravimetry sea-level signal (GRACE), which accounts for the mass-induced sea-level signal variation, from the satellite altimetry data (Garcia *et al.*, 2006). Garcia *et al.* (2010) define the sea-level signal (represented by satellite altimetry) as the result of the steric and mass component, $SL_{TOT} = \eta_{steric} + \eta_{mass}$, defining the deduced steric component as, $\eta_{steric} = SL_{TOT} - \eta_{mass}$. Figure 2.3 shows the signal described above (black line) and the $\eta_{sat}^{st}(t)$ signal (green line). The two curves are very similar, with differences in minimum (2005 and 2006) and maximum peaks (2007), probably due to the coarse resolution of gravimetry data (1 °) which does not allow the resolution of the total intra-annual variability of the steric signal in the Mediterranean.

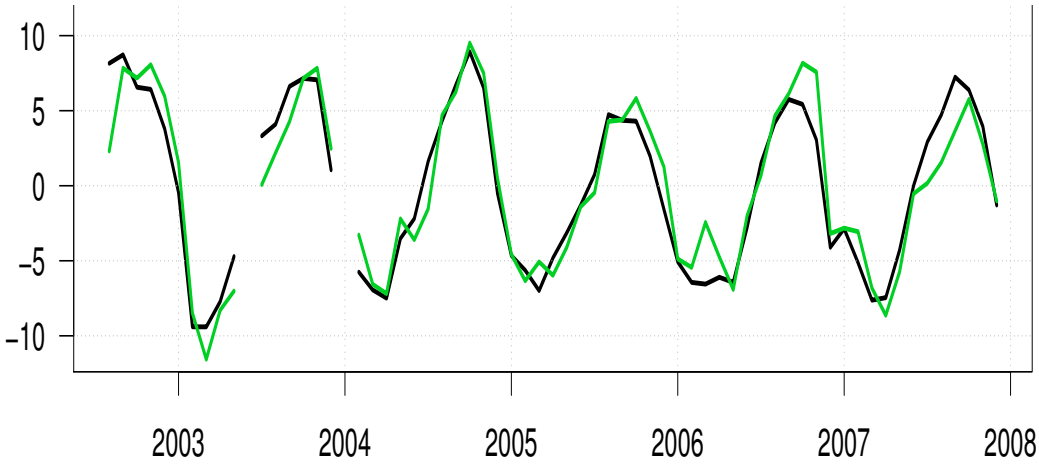

Figure 2.3: $\eta_{sat}^{st}(t)$ of satellite altimetry (green line) and steric signal obtained subtracting the satellite gravimetry (GRACE) signal (black line) from the satellite altimetry signal; y-axis values expressed as $[cm]$.

Just as we did in equation (2.3), we can define the sea level measured by the tide gauges as

$$\eta_{ins}(x_i, y_i, t) = \eta^{st}_{sat}(t) + \eta^{IB}(x_i, y_i, t) + \eta^{mean}_{ins}(x_i, y_i) + \eta^{var}_{ins}(x_i, y_i, t) + C \quad (2.4)$$

where x_i, y_i are the station coordinates, $\eta_{ins}(x_i, y_i, t)$ the in-situ local mean sea level, $\eta^{st}_{sat}(t)$ the sea-level steric component, $\eta^{IB}(x_i, y_i, t)$ the inverse barometer effect, $\eta^{mean}(x_i, y_i)$ the mean dynamic topography over the same reference period (1993 - 1999), $\eta^{var}_{ins}(x, y, t)$ the time- and space-dependent local sea-level component and C the local datum correction. The local datum correction is computed removing the temporal mean from each tide-gauge station time series.

As said in Sub-section 2.2.2, the inverse barometer effect is removed from the altimetry data, and this correction is therefore applied to the tide-gauge data to compare the two signals, considering the inverse barometer effect as described in Dorandeu & Le Traon (1999a):

$$\eta^{IB}(x_i, y_i, t) = -\frac{1}{\rho g}(Pa(x_i, y_i, t) - Pa_{ref}(t)) \quad (2.5)$$

where ρ is the sea water density, Pa the mean seal-level pressure (MSLP), retrieved from the European Centre for Medium-Range Weather Forecasts (ECMWF) Re-analysis dataset (ERA-Interim), for the tide-gauge position, and Pa_{ref} is the MSLP spatial mean over the Mediterranean basin computed during the period 1993-2010. Removing this component from the sea level measured by the tide gauges we obtain:

$$\eta^{*}_{ins}(x_i, y_i, t) = \eta_{ins}(t) - \eta^{IB} \quad (2.6)$$

If we now consider the period 1993-2010 (rather than the reference period 1993-1999), it results that the temporal mean of sla_{sat} and η_{ins} are:

$$\langle sla_{sat} \rangle \neq 0 = \alpha \quad (2.7)$$

$$\langle \eta^{*}_{ins} \rangle = \eta^{mean}_{ins} + \langle \eta^{st}_{sat} \rangle + C = \beta \quad (2.8)$$

To compare the two datasets we therefore subtract $\eta^{st}_{sat}(t)$, α and β respectively

from the satellite and tide-gauge data, obtaining:

$$sla' = sla_{sat} - \eta^{st}_{sat}(t) - \alpha \tag{2.9}$$

$$\eta^{*'}_{ins} = \eta^{*}_{ins} - \eta^{st}_{sat}(t) - \beta \tag{2.10}$$

The sea-level signals sla' and $\eta^{*'}_{ins}$, which account for the low-frequency sea-level variability over the decadal time scale, are used to compare the two datasets in the different parts of the basin during the period between 1993 and 2010.

2.4 Comparison of in-situ and remote-sensing data

This part of the analysis has been realized comparing the time series of the two observational data sets, considering the altimetry-gridded data interpolated over the tide gauges geographical positions (see Table 2.2). The interpolation has been carried out considering at least four grid points around the tide-gauge coordinate, and assigning weights to each one according to their distance from the station position.

Taking into consideration the error associated with the satellite altimetry measurements near the coasts due to the cutting of satellite tracks along the coasts to avoid land reflection and the along track altimetry signal smoothing performed applying signal corrections (see Table 2.2.2), and interpolating over a regular grid (Ducet *et al.*, 2000), we present here the results obtained comparing the two sea-level signals.

The first result is that the two sea-level signals gathered by the two different instruments (tide gauges and satellite), decomposed and filtered in order to investigate their low-frequency variability, do not result as being comparable all over the basin in terms of time evolution and amplitude correlations over all the basin, showing different correlation patterns that strongly depend on the area considered. In the western part of the basin, moving from Gibraltar up to the Gulf of Lion, the two sea-level signals result as being positively correlated to the

order of 0.3, underlining the lack of correlation in this part of basin. In Figures 2.4a and 2.4b the cases of Mlaga and Marseilles respectively are shown.

Higher correlation patterns have been found in the Adriatic, in particular in the upper part, where the continental shelf is most extended. Figure

2.4c shows the case of Trieste where the two time series are highly correlated and the amplitude of local sea level is well reproduced by the altimetry. The same pattern has been found in the case of Dubrovnik (2.4d), except for the positive peaks of the tide gauge signals. In the central part of the basin, looking at the particular case of Valletta (Figure 2.4e), the two signals result as being highly correlated, underlining the fact that the sea-level signal captured by the tide-gauge station in Malta is an open-ocean signal.

The opposing situation has been found in the Levantine basin, where the shelves areas are generally narrow, and the correlation of the two signals tends to decrease up to 0.2, as it does along the Israeli coasts in the case of Hadera, where the altimetry signal range is much smaller than the tide-gauge one (Figure 2.4f).

The continental shelf extension strongly influence the coastal ocean dynamics. The concept of narrow shelves has been reviewed by Sanchez-Arcilla & Simpson (2002) from both morphological (shelf width) and dynamical (along-slope current amplitudes) points of view. It is explained that regions constrained by two boundary layers (one in the near-shore and the other on the slope) that merge and control processes across the continental shelf can be defined as narrow shelves. In narrow-shelf areas the near-shore and slope processes couple these regions to the shelf dynamics, while in wide-shelf areas the three areas are dynamically separated. Assuming along-slope currents of 20-30 $m\ s^{-1}$ over all the Mediterranean basin, Pinardi *et al.* (2005) define a shelf extension of 20-30 km as the critical shelf width for strong nonlinear coupling. Following their characterization of the shelves in the Mediterranean basin, critical shelf widths (20-30 km) can be found in the western part of the basin along the coasts of Morocco, Algeria and Libya; even less extended shelves (10-20 km) are observed along the Spanish coasts in the Alboran Sea and in the Balearic islands (Majorca). In the eastern part of the basin the most critical areas are represented by the Israeli and Cypriot coasts ($<$ 10 km). On the other hand, the Adriatic Sea is the area, together with the Tunisian shelf, where the continental shelf is most extended in the basin (330 530

km).

Shelf extension cannot be the only parameter that affects the sea-level signals recorded by the two instruments, as it does not explain the differences found in areas where the continental shelf is well extended, such as Marseilles and Trieste, nor the differences found in narrow-shelf areas, such as in Valletta and Hadera. Investigation of other sources of local low-frequency sea-level variability will be the object of further studies about this topic, and will look in detail at the local ocean dynamics, focusing on Eddy Kinetic Energy (EKE; Pujol & Larnicol, 2005), heat and water fluxes that characterize the different coastal areas.

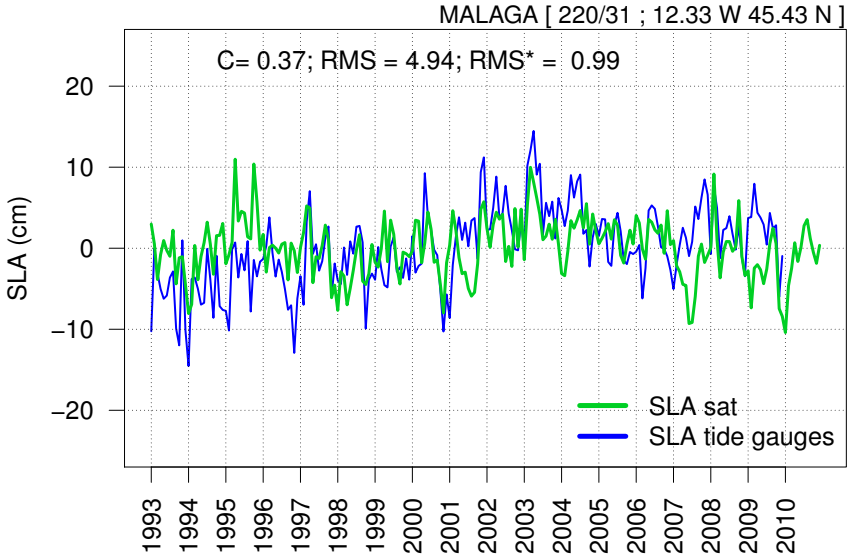

(a) Malaga

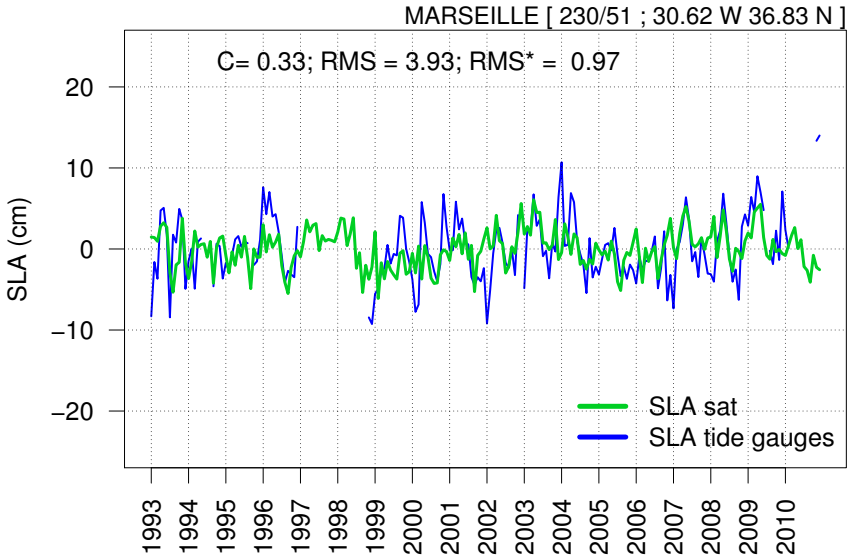

(b) Marseille

Figure 2.4: SLA Time Evolution: tide-gauge and satellite altimetry comparison. From west to east across the basin; the cases of Mlaga (a), Ste (b), Marseilles (c), Dubrovnik (d), Valletta (e) and Hadera (f) are shown.

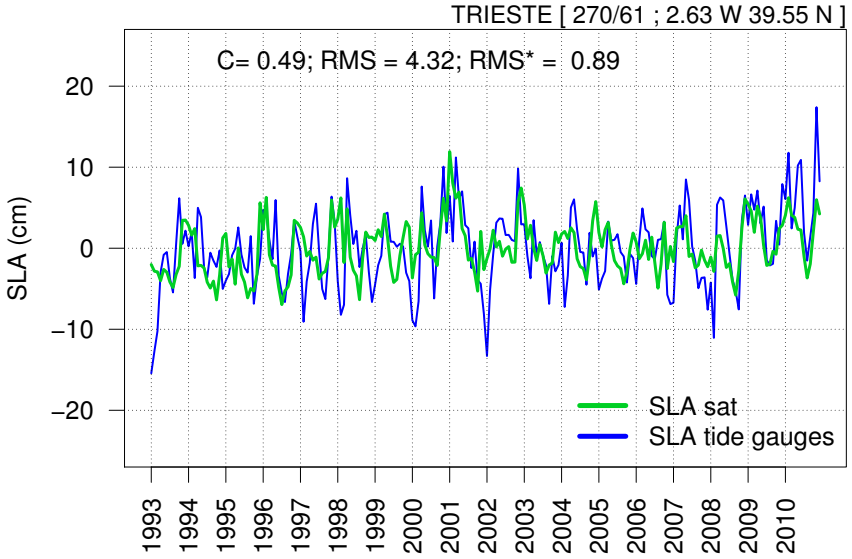

(c) Trieste

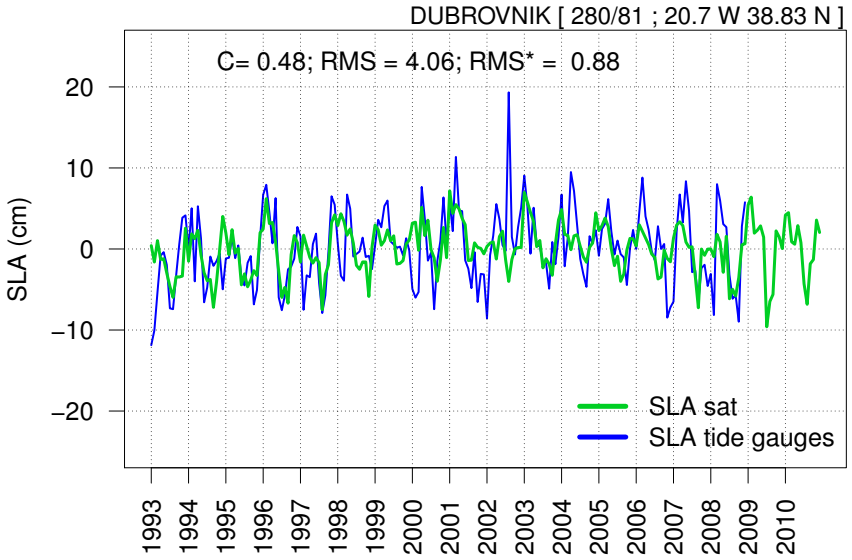

(d) Dubrovnik

Figure 2.4: SLA Time Evolution: tide gauge and satellite altimetry comparison. From west to east across the basin; the cases of Mlaga (a), Ste (b), Marseilles (c), Dubrovnik (d), Valletta (e) and Hadera are shown. (f).

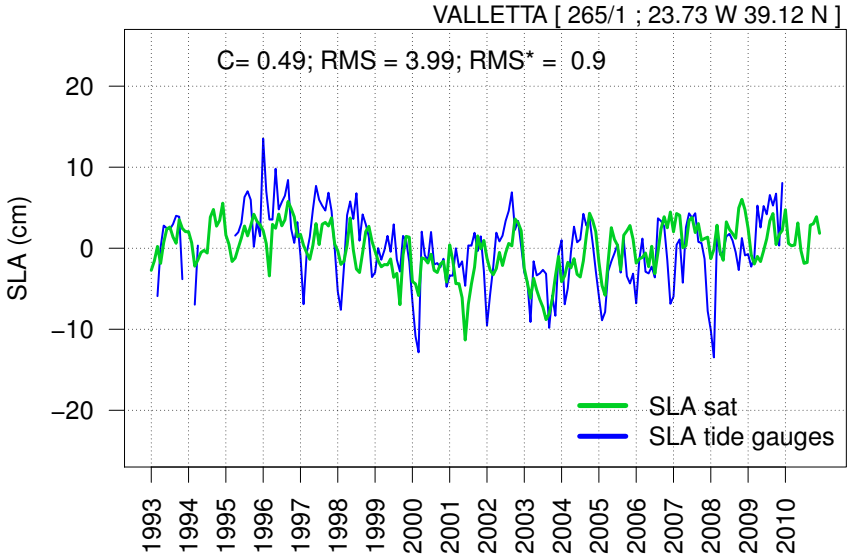

(e) Valletta

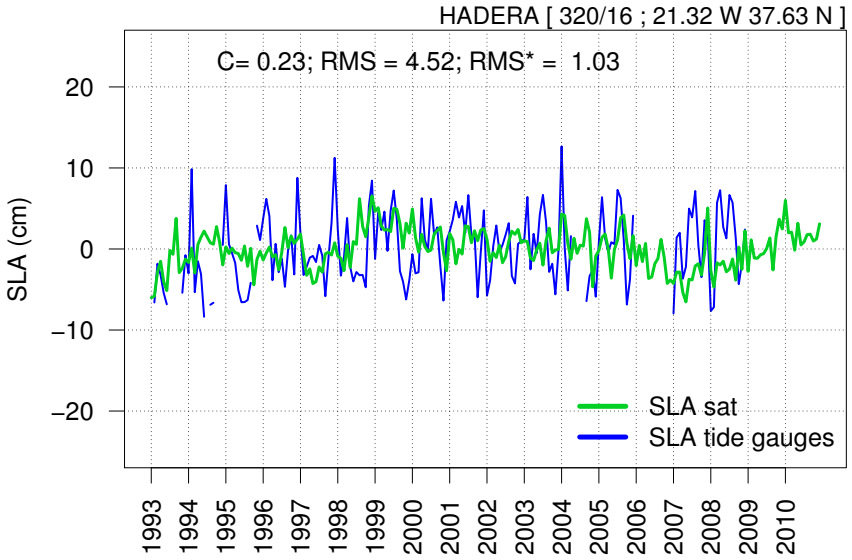

(f) Hadera

Figure 2.4: SLA Time Evolution: tide gauge and satellite altimetry comparison. From west to east across the basin; the cases of Mlaga (a), Ste (b), Marseilles (c), Dubrovnik (d), Valletta (e) and Hadera are shown. (f).

	code	lon	lat	%	C	RMS	RMS*	tide.gauge	satellite	GIA
ALEXANDROUPOLIS	290/65	25.88	40.85	94	0.57	4.43	0.82	2.33±1.38	2.58±0.8	-0.44
ANTALYA II	310/52	30.62	36.83	78	0.43	4.81	0.92	3.84±1.53	0.18±0.84	0.36
BAKAR	280/11	14.53	45.3	89	0.53	4.44	0.85	-0.37±1.62	0.69±0.8	0.71
BARCELONA	220/61	2.17	41.35	80	0.28	4.46	1	7±1.38	2.17±0.68	-2.44
BODRUM II	310/46	27.42	37.03	79	0.22	5.28	0.99	2.59±1.77	2.82±0.51	-2.81
DUBROVNIK	280/81	18.06	42.66	89	0.48	4.06	0.88	1.57±1.4	0.58±0.78	0.01
HADERA	320/16	34.88	32.47	78	0.23	4.52	1.03	2.06±1.48	0.04±0.64	0.08
KALAMAI	290/21	22.13	37.02	92	0.39	4.12	0.93	3.06±1.08	0.54±0.57	-
KATAKOLON	290/17	21.32	37.63	92	0.07	4.58	1.15	1.13±1.05	0.82±0.66	-0.28
KAVALLA	290/61	24.42	40.92	85	0.26	9.96	0.96	-0.46±2.93	1.81±0.71	-0.26
KHALKIS NORTH	290/34	23.6	38.47	92	0.36	4.57	0.94	4.7±1.19	1.09±0.63	-0.03
KHALKIS SOUTH	290/33	23.6	38.47	83	0.16	5.46	1.04	-1.92±1.46	1.09±0.63	-0.03
KHIOS	290/71	26.15	38.38	92	0.43	5.08	0.91	-0.5±1.46	0.47±0.79	-0.03
LEROS	290/91	26.88	37.08	90	0.42	4.15	0.91	-1.7±1.24	0.57±0.59	-0.66
LEVKAS	290/4	20.7	38.83	87	0.27	4.87	0.99	-0.55±1.36	-0.39±0.67	-
MALAGA	220/31	-4.42	36.72	94	0.37	4.94	0.99	5.7±1.2	0.23±0.94	-0.46
MALAGA II	220/32	-4.42	36.72	93	0.39	4.3	1.04	2.57±1.14	0.22±0.94	-0.45
MARSEILLE	230/51	5.35	43.3	84	0.33	3.93	0.97	1.64±1.16	0.92±0.61	-0.4
MENTES/IZMIR	310/42	26.72	38.43	83	0.51	4.29	0.86	2.62±1.5	1.15±0.7	-0.43
NICE	230/81	7.27	43.7	77	0.2	4.61	1.12	0.83±1.26	-0.24±0.78	-0.27
PATRAI	290/14	21.73	38.23	75	0.03	6.13	1.04	10.47±1.69	0.91±0.5	-0.49
PREVEZA	290/1	20.77	38.95	84	0.17	4.86	1.08	-0.44±1.18	-0.5±0.69	-
ROVINJ	280/6	13.63	45.08	89	0.43	4.47	0.98	-0.84±1.4	1.89±0.95	-0.31

SETE	230/21	3.7	43.4	72	0.16	8.83	0.99	2.58±3.16	-0.2±0.69	0.57
SPLIT - GRADSKA LUKA	280/31	16.44	43.51	89	0.55	4.12	0.84	2.37±1.49	1.69±0.85	-0.57
SPLIT RT MARJANA	280/21	16.39	43.51	88	0.59	4.46	0.81	-0.42±1.73	1.67±0.85	-0.55
THESSALONIKI	290/51	23.03	40.62	91	0.4	4.66	0.92	2.33±1.26	0.22±0.65	1.18
TOULON	230/61	5.92	43.12	95	0.35	3.82	0.97	-0.79±1.04	-1.33±0.63	1.56
TRIESTE	270/61	13.76	45.65	100	0.49	4.32	0.89	1.05±1.21	0.03±0.82	1.49
VALLETTA	265/1	14.52	35.9	87	0.49	3.99	0.9	-2.38±1.36	-0.42±0.79	0.42
ZADAR	280/13	15.23	44.12	80	0.04	11.05	1.02	-1.59±3.9	1.17±0.75	0.19

Table 2.2: Satellite altimetry and tide gauges data comparison at the nearest point: sla considered removing the eta steric sat computed as a the spatialm mean of the satellite data,removing the temporal mean for the whole analysis period (1993 - 2010) and the inverse barometer effect from the tide gauges time series. Columns 1 to columns 3 represent the tide gauge stations metadata:n PSLMS code and geographical coordinates. Columns 4 express the percentage of the time series completeness (%). Columns 5 to 7 show basic descriptive statistic of the data-sets comparison: correlation coefficient (C), root mean square error (RMS) and the root mean square error normalized for standard deviation (RMS*). Columns 8 and 9 show the sea level trends estimated by the tide gauges and satellite altimetry respectively [$mm\ yr^{-1}$]. Column 9 is glacio-isosthatic adjustment correction applied to the estimated trends.

2.5 Sea-level trend spatial variability

The trend (least square fitting) estimated from altimetry data shows a sea-level rise of $2.15 \pm 0.7 mm\ yr^{-1}$ (seasonal signal removed and GIA applied) on average in the Mediterranean area

during the period 1993 to 2010. This value, estimated over a relatively short temporal period, should be considered only as a general index of the sea-level *"rise"* in the Mediterranean , and it does not have a continuous pattern in the basin. The significance of the trend found will be discussed in detail in the next section on trend temporal variability. Figure 2.5 shows the marked spatial variability of the sea-level trend in the Mediterranaean. It is interesting to notice how in the Adriatic and Aegean Seas high positive trends are found. More than 5 $mm\ yr^{-1}$ are observed in the Adriatic Sea and up to 3 $mm\ yr^{-1}$ along the Tunisian coast. These are the most extended shallow water areas in the basin (Pinardi *et al.*, 2005), and are also more sensitive to the effects of the external forcings, such as heat and water fluxes, compared to deep ocean areas. In these areas the changes of the climatic variables have the strongest signature, which evidently results in high positive sea-level trends being resultant of the interaction of many of them.

Higher positive value are also observed in a large part of the Eastern basin, locally underlining the presence of recurent gyres and eddies in the circulation. Maximun positive peaks, with more than 8 $mm\ yr^{-1}$, have been found in the Levantine basin, south-eat of Crete (Ierapetra gyre) and west of Crete (Pelops gyre) (Pinardi *et al.*, 2005). Similar peaks are indicated at the location of the Mersa Matruh gyre. On the other hand, a strong negative trend (less than -8 $mm\ yr^{-1}$) is observed in the Ionian Sea as a consequence of an important change in the circulation observed in this basin since the beginning of the nineteen-nineties (Demirov & Pinardi, 2002).

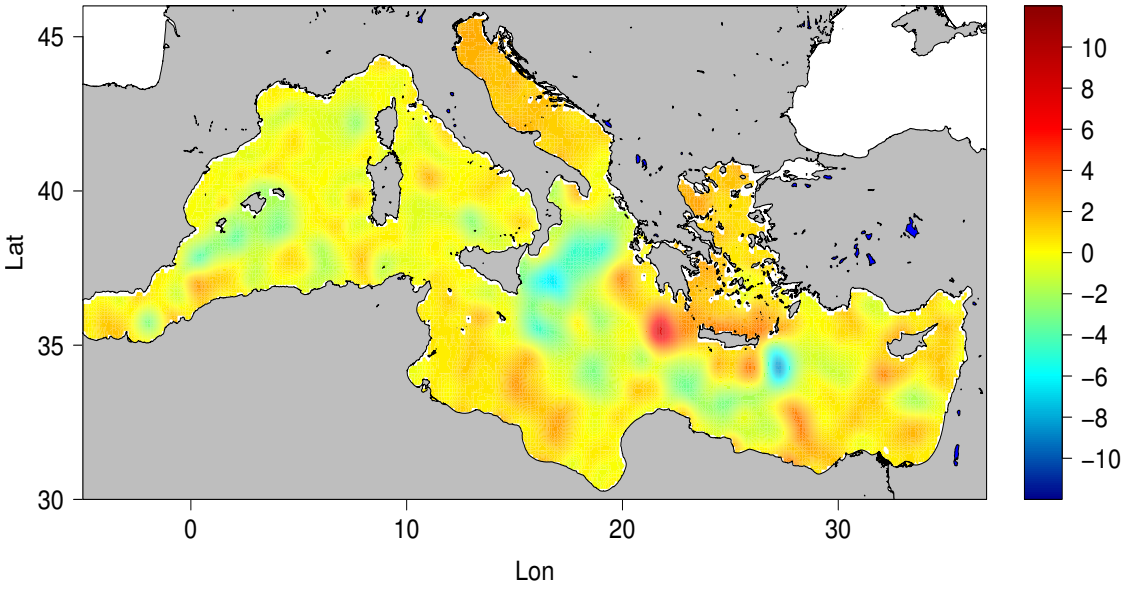

Figure 2.5: Satellite altimetry trend $[mm\ yr^{-1}]$ spatial variability in the Mediterranean during the period 1993-2010. Steric signal removed, glacial-isostatic adjustment (GIA) applied.

2.6 Sea-level trend temporal variability

The sea-level trend in the Mediterranean also shows a high temporal variability. Adopting the method described in Liebmann *et al.* (2010) to estimate the global surface temperature trends, in Figure 2.6a every possible trend $(mm\ yr^{-1})$ computed as a function of the length of the period considered (1-year changes discarded) is shown. Each point of the diagram indicates sea-level trend up to a specific year (x-axis) obtained considering the number of years expressed on the y-axis. In this way it is possible to note all the sea-level changes occuring over the last 18 years (1993-2010). One of the most interesting results of this analysis is that during the period between 1998 and 2010 it is almost impossible to recognize any trend without considering at least 10 years of data, as confirmed by the T-test trend significance analysis (Figure 2.6b). This analysis also underlines the fact that to find a stable and significative positive trend in the Mediterranean basin it is necessary to consider at least 14 years of data, from 1993 to 2007, and more then 15 years to obtain a high significant trend. Sea-level change occurring

over a short time period does not result as significant, and does not account for the signal of the low-frequency sea-level variability and trend. These results, also confirmed performing bootstrap analysis (Liebmann *et al.*, 2010), also show that the period considered to obtain the trend spatial varibility, even when obtianed starting from only 17 years of data, allow a trend significance level of 99.9 % to be obtained.

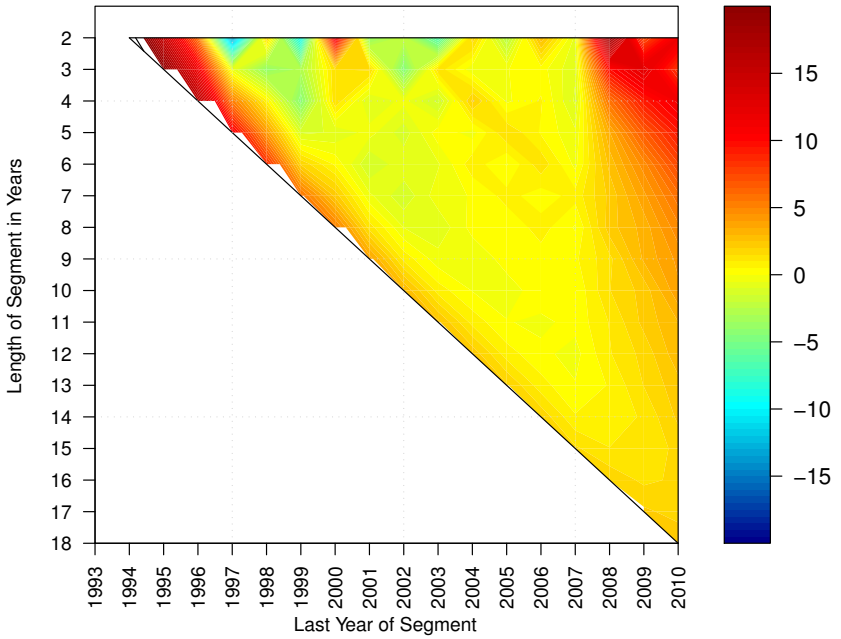

(a) SLA Trend as function of length of segment and ending year of calculation ($mm\ \ yr^{-1}$).

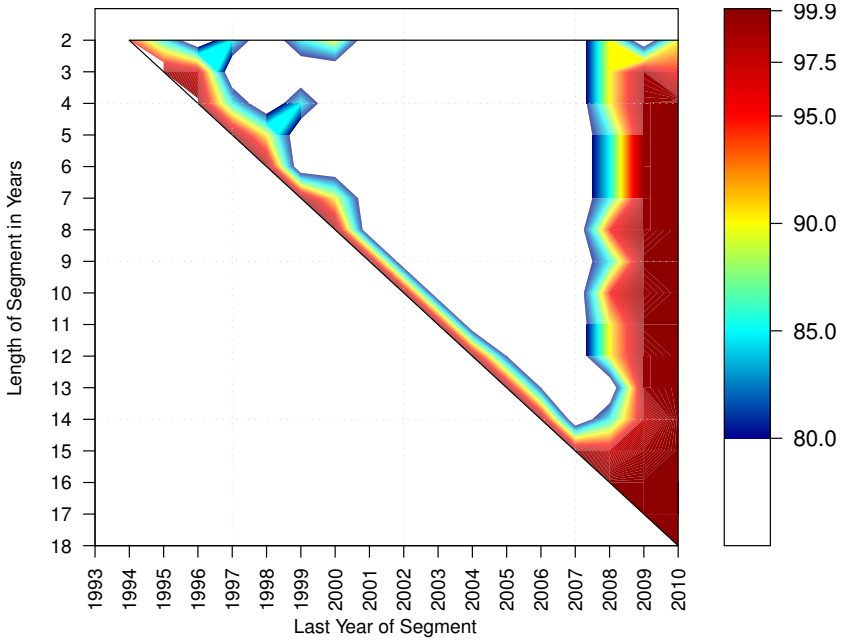

(b) Rank of observed changes using T - test (%).

Figure 2.6: Satellite Trend as function of the length of the period considered. Panel (a) shows all the possible trends ending at the year indicated in the x-axis, obatained considering the number of years shown over the y-axis. Thus, considering the point x=2000 and y=10, it express the sea-level trend value up to the year 2000, obtained considering 10 years of data. Panel (b) shows the trend significance obtained performing a T-test; values below 80 % are not shown.

2.7 Summary

A method to decompose the sea-level signal of in-situ and remote-sensing observations is proposed in order to compare tide-gauge and altimetry sea-level low-frequency variability. An interesting result is that the tide-gauge coastal sea-level signal is a large-scale signal and results as being well comparable with satellite altimetry data in the basin areas where the continental shelf is extended. In particular, the two signals result as being well correlated in the Adriatic and off Malta; the latter represents a particular case of an open-ocean island tide-gauge that captures a sea-level signal similar to the satellite altimetry in the area. Moving towards the Levantin basin, the shelf extension generally decreases, and the two datasets tend to be less comparable in terms of correlation, although it remains positive with a root mean square error that remains under 5 cm (Hadera).

Shelf extension does not explain the differences found in areas where the continental shelf is well extended, such as Marseilles and Trieste, nor the differences found in narrow-shelf areas, such as in Valletta and Hadera. Local low-frequency sea-level variability will be the object of further studies, and will look in detail at specific ocean dynamics (i.e., Eddy Kinetic Energy, heat and water fluxes) at the local scale.

Looking at the basin trend, a positive trend of $2.15 \pm 0.7 mm\ yr^{-1}$ is observed in the Mediterranean basin between 1993 and 2010. The basin trend presents a marked spatial variability, mainly characterized by strong positive trends in the shelf areas and negative trends in the Ionian, due to a strong change of the circulation in this basin. The study on the trend variations as function of the number of years considered shows that in ordert to obtain a significant and stable positive trend during the period between 1993 and 2010 at least 15 years of data should be considered.

One of the points of weakness of this study is the total lack of in-situ data in the southern part of the basin. This is an issue that affects every study about sea level in the Mediterranean, and has been faced several times during this research.

Chapter 3

Sea-level variability over a centennial time period

3.1 Sea-level studies over a centennial time scale

Changes in sea-level are one of the most important indexes of climate change, as they are caused by many processes that act at different spatial and temporal scales. One of the biggest sources of uncertainty related to sea-level change is that we still do not know what the sea-level response to climate change scenarios is (Church *et al.*, 2010). (Bindoff *et al.*, 2007) aims at providing the changes over the coming century, which are affected by great uncertainties. The best possible strategy to minimize this future uncertainty is to look at the past and try to understand in details all sea-level variability components.

In this context, all observational instruments, such as altimetry and tide gauges, provide very important information for understanding sea-level change dynamics. Tide-gauge data have very long time series that can provide useful information over decadal time scales, but are spatially discontinuous. Satellite altimetry, on the other hand, is almost homogeneous in the spatial domain, but the data only spans the past 20 years.

Sea-level reconstruction is a method capable of merging the altimetry and tide-gauge sea-level signals, taking spatial information from the former and temporal amplitude from the latter (Kaplan *et al.*, 2000). Over the last ten years, many

efforts have been made to realize various sea-level reconstructions at both global (Church, 2006; Church *et al.*, 2004a; Church & White, 2011) and regional scales. The first sea-level reconstruction for the Mediterranean, was realized by (Calafat & Gomis, 2009) using satellite altimetry data with a horizontal resolution of 1/4 ° and tide gauges for the period 1945-2004, later updated up to 2008 using 1/8 ° x 1/8 ° satellite data in Calafat & Jordà (2011), looking in particular at errors associated with seal-level reconstructions. Meyssignac *et al.* (2011) offers a comparison between satellite-based and model-based reconstructions obtained using outputs from numerical models for the period 1976-2000.

The general objective of this work is to attempt a sea-level reconstruction in the Mediterranean over a centennial time scale (from the end of the nineteenth century to 2010). To achieve this objective, satellite altimetry and tide-gauge data have been merged through a reduced-space optimal interpolation technique as described in Church *et al.* (2004a). This method allows sea-level spatial varibility acquired from the altimetry leading EOFs to be fitted to temporal variability from tide-gauges. The specific objectives are: i) to validate results obtained at the basin scale with satellite altimetry data, for the satellite era, as well as locally with tide-gauge time series over the remaining reconstruction period; ii) to investigate sea-level trend spatial and temporal variability over the last century, paying particular attention to low-frequency variability (decadal and multidecadal).

This chapter in organized as follows: a description of the method used to perform the sea-level reconstruction is given in Section 3.3. Section 3.2 shows the satellite altimetry data and tide-gauge stations used for the reconstruction.

Section 3.5 shows the validation of the sea-level reconstruction with a comparison with the altimetry data for the period 1993-2010, as well as a comparison with tide-gauge observations during reconstruction sub-periods. In the second part of the section, the results obtained for the entire reconstruction period are discussed, with particular attention paid to trend variations at the decadal time scales. Section 3.6 illustrates a case study of the Tunisian coasts, where sea-level reconstruction data has been used to look at long-term sea level trends in target sensitive areas. All the results obtained are summarized in Section 3.7.

3.2 Data processing

Here we illustrate the data processingof the satellite altimetry and tide-gauge datasets

in order to prepare the data for sea-level reconstruction.Tide-gauge and altimetry data have been corrected as described in the previous chapter (section 2.3) in order to obtain from both datasets physically coherent sea-level signals.

3.2.1 The tide-gauge dataset

The RLR dataset distributed by the PSMSL (Woodworth & Player, 2003) is composed, in the Mediterranean basin, of 93 stations, with records that start in 1872. RLR datasets reduce tide-gauge time series to a common datum (see Section 2.2) using a tide-gauge history datum provided by the supplying authority (see Table 2.2, last column). Time series length depends on the station considered: 4 stations in the Mediterranean basin have a range longer than 100 years, as shown in Table 3.1. The distribution and temporal coverage of the entire dataset are shown in Appendix A. The reconstruction period has been divided into differents sub-periods according to in-situ data availability. The gaps in the dataset have been filled with spline interpolation for gaps up to 6 months, and multiple linear regressions (Calafat & Jordà, 2011) for gaps up to 12 months, while tide-gauge stations with gaps longer than 12 months during each specific sub-period have been filtered out of the reconstruction. These periods have an overlapping period of 12 months, which is a necessary condition for integrating EOF amplitudes change backwards in time (Church *et al.*, 2004b). The total reconstruction period is from 1885 to 2010, divided into 8 sub-periods spanning 15 years each. The tide-gauge stations considered for each sub-period are shown in Figure 3.1.

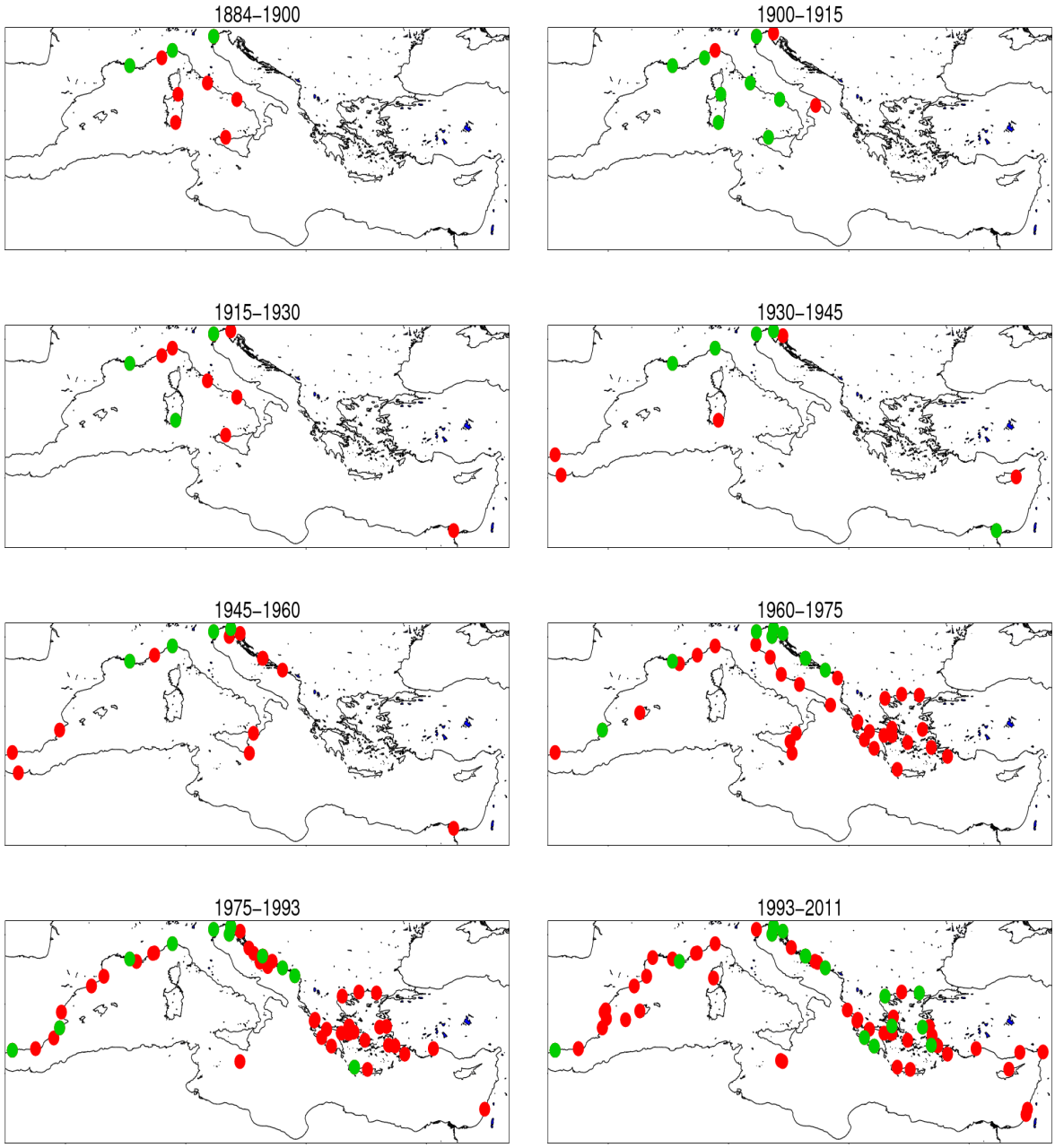

Figure 3.1: Tide-gauge stations positions. In each panel the number and positions of tide-gauge stations used in the specific reconstruction period are shown. Red dots represent the total number of stations available in the specific temporal periods indicated above. Green dots indicate the actual amount of tide-gauge stations considered, representing the stations with the most complete time series.

	code	lon	lat	range	years	n.years	%	ref
TRIESTE	270/61	13.76	45.65	1905-2010	106	100	94	-9.4
GENOVA	250/11	8.9	44.4	1884-1997	114	90	78	-10.2
MARSEILLE	230/51	5.35	43.3	1885-2010	126	122	97	-8.5
VENEZIA 1	270/54	12.33	45.43	1909-2000	92	87	94	-6.8
VENEZIA 2	270/51	12.33	45.42	1872-1920	49	48	98	-9.9
VENEZIA 3	270/41	12.35	45.42	1889-1913	25	24	96	-10.5

Table 3.1: Tide gauge stations RLR in the Mediterranean Sea, with time series that span a period longer 100 years. Columns 4 ad 5 express the period and the number of years covered by the station data. Columns 6 and 7 show the amout of data available once rmoved the missing data as numbers of yeasr and percentage (%) respectively. Column 8 indicates tide-gauges benchmarks $[m]$ (see Appendix 1). We consider also the three tide gauges stations located in Venezia that considered togheter cover a period longer that 100 years. In Column 1, VENEZIA 1 correspond to Venezia Punta della Salute, VENEZIA 2 is Venezia Santo Stefano and VENEZIA 3 represent Venezia Arsenale.

3.2.2 Satellite Altimetry dataset

The satellite altimetry data (Pujol & Larnicol, 2005) corrected as described in Chapter 2 has been used here to retrieve the sea-level reconstruction spatial variability. Data have been selected for the period from January 1993 to December 2010 as monthly means. The data have been pre-processed removing the seasonal cycle and subtracting the mean sea-level trend (see Chapter 3), in order to obtain unbiased EOFs (Kaplan *et al.*, 1997). Since EOFs account only for the spatial variability, the reconstructed sea-level trend (if present) will be obtained from the tide-gauge records temporal variability. Following (Meyssignac *et al.*, 2011), GIA correction provided by Stocchi & Spada (2009), which is of the order of -0.25 $mmyr^{-1}$, has been applied to the data.

3.3 Merging remote-sensing and in-situ sea-level signals: statistical reconstruction method

The method used to reconstruct the sea-level field during the last century is a reduced-space optimal interpolation described by Kaplan *et al.* (2000), applied as in Church *et al.* (2004a) and Calafat & Gomis (2009) for global and regional sea-level reconstructions respectively.

The first step, called *feature extraction*, is to get spatial information from the satellite data that will provide the reconstruction spatial variability. Organizing the altimetry data in a matrix that contain in the rows (m) the spatial grid points, and in the columns (n), all the time steps, an m x n matrix (Z) is obtained. The matrix Z can be separated into three matrices by using a singular value decomposition (SVD) :

$$Z = ULV^T \tag{3.1}$$

where U is an m x n matrix that contain the left singular vectors of the matrix Z (eigenvectors of the covariance matix $\mathrm{Z^TZ}$, EOFs), L is an n x n diagonal matrix that contains the singular values (γ, square root of the eigenvalues of the covariance matrix) of Z, and V is an n x n matrix the columns of which are the right singular vectors of Z (eigenvectors of the covariance matix $\mathrm{ZZ^T}$)(Bjornsson & Venegas, 1997). Eigenvalues are related to the singular values by $\lambda_i = s_i^2/n$, where n is the number of grid points (Storch & Zwiers, 1999). Each eigenvalue gives a fraction of the total variance in the covariance matrix explained by each mode. The variance (Y) explained by each EOF_i is therefore obtained dividing the relative eigenvalue (λ_i) by the sum of all the other eigenvalues (Bjornsson & Venegas, 1997):

$$Y_i = \lambda_i / \sum_{i=1}^{n} \lambda_i \tag{3.2}$$

The expression (3.1) can also be written as :

$$Z_M \backsimeq U_M L_M V_M^T$$

where $L_M$is the diagonal matrix that contains the largest eigenvalues in the *reduced phase space*. U_M is the matrix with the the columns which are eigenvectors (EOFs) corresponding to the eigenvalues contained in L_M respectively. The leading U_M eigenvectors define the reduced space of the main modes of large-scale variability in which we will be looking for an analysed solution. The discarded part of the total space is assumed to be contaminated by noise (Kaplan *et al.*, 2000).

The singular value decomposition divides the initial field into a space-dependent component ($U(x, y)$) and a time-dependent one (($V(t)$). It is thus possible to approximate the initial $Z(x, y, t)$ matrix, considering only the lowest modes ("M") which explain most of the variance:

$$Z_M(x, y, t) = U_M(x, y) * L_M * V_M^T(t) = U_M(x, y) * \tilde{\alpha}(t) \tag{3.3}$$

with $\tilde{\alpha(t)}$, determined by the satellite data, is an m x n matrix the rows of which are the time series of the amplitude for the lowest EOFs (Calafat & Gomis, 2009).

We want to estimate instead

$$Z_M^*(x, y, t) = U_M * \alpha(t) \tag{3.4}$$

with $\alpha(t)$ estimated starting from the tide-gauge data.

The second step of this method is to find the set of $\tilde{\alpha}(t)$ that find the best fit to the tide-gauges by optimal interpolation as described by Kaplan *et al.* (2000). For each time step (month) in the record, the reduced-space optimal interpolation solution for $\alpha(t)$ is the one that minimizes the cost function:

$$S(\alpha) = (HU_M\tilde{\alpha} - Z^0)^T R^{-1}(HU_M\tilde{\alpha} - Z^0) + \tilde{\alpha}^T\Lambda^{-1}\tilde{\alpha} \tag{3.5}$$

where Z^0 is a matrix of the available tide-gauges observations, the rows of which represent each tide-gauge station available and the time steps in the column. H is a transfer operator from the full grid representation of the satellite altimetry field to the available observations, Λ is a diagonal matrix of the eigen-

values of the covariance matrix. R is the error covariance matrix represented by two terms:

$$R = \Sigma + HU'L'U'^{T}H^{T} \tag{3.6}$$

The term Σ is the data error covariance matrix accounting for the sampling error (spatially uncorrelated, to the order of $\sim$ 5 cm) . The second term in R contains the covariance of the truncated modes. It accounts for the errors introduced by ignoring higher-order EOFs in the reconstruction.

Tide-gauge observations are relative to their own local datum. Following Church *et al.* (2004b), to eliminate the reliance we consider the change in height between adjacent time steps. In (3.4), the EOFs are functions of space only and the amplitudes are functions of time only. Thus for adjacent times t_n and t_{n+1}, we can rewrite (3.4) as

$$Z^*_M(x, y, t_{n+1}) - Z^*_M(x, y, t_n) = U_M(x, y) \cdot [\alpha(t_{n+1}) - \alpha(t_n)] \tag{3.7}$$

$$\Delta Z^*_M = U_M(x, y) \cdot \Delta\alpha(t_n) \tag{3.8}$$

Because of the first term in the formulation of the cost function (3.5), the minimization of S will constrain the solution to be close to the observed data (within the uncertainty defined by observational error). The second term confines the distribution of energy over the modes of variability to that found in the data (i.e., a derived temporal coefficient of a given eigenvector cannot have more variance than the corresponding eigenvalue Kaplan *et al.*, 2000).

The change in amplitudes of the leading EOFs between each time step can be obtained minimizing the cost function (3.5). Minimizing S gives the optimal interpolation solution:

$$\Delta\alpha = PU^T_M H^T R^{-1} \Delta Z^0 \tag{3.9}$$

where

$$\Delta Z^0 = Z^0(x, y, t_{n+1}) - Z^0(x, y, t_n) \tag{3.10}$$

and

$$P = (U_M^T H^T R^{-1} H U_M + \Lambda^{-1})^{-1} \tag{3.11}$$

is a theoretical estimate for error covariance in the solution (Kalman gain).

Once the chage in amplitude of EOFs for each time step has been obtained, the amplitudes can be obtained integrating backward in time as described in Church *et al.* (2004b) and Calafat & Jordà (2011) for global and regional cases respectively.

The reduced-space optimal interpolation solution can be converted into its full grid representation by sustituting the estimated amplitudes $\alpha(t)$ in the expression (3.4), obtaining the whole sea-level recontruction.

3.3.1 EOFs selection

In order to define the optimal number of EOFs to be used to perform the sea-level reconstruction, we follow the method described in (Calafat & Jordà, 2011).

A crucial point of the reconstruction method is the selection of the number of EOFs, which depends strictly on the number of observations used. If a high number of EOFs are selected, the reconstruction will result as having a high skill during the period when the EOFs were computed (satellite altimetry period), but the error will significantly increase for the rest of the reconstruction period.

Repeating the experiment realized in Calafat & Jordà (2011) for our sea-level reconstruction set-up, the optimal number of EOFs is found comparing the reconstructed and satellite fields during a period different from that used to compute EOFs. Following the definitions of Calafat & Jordà (2011), these period are defined as the validation period (1993-2001) and the training period (2002-2010) respectively. An ideal dataset of observation has been used to carry out this test experiment; this is represented by the satellite data sampled in the

tide-gauge positions (see Appendix A, Figure 1). Figure 3.2 shows the results of this analysis in terms of root mean square error (rmse) variations against the increasing number of EOFs considered in the reconstructions. During the training period the rmse gets lower as the number of EOFs used in the recostruction increases. In the validation period we observe that the rmse tends to increase as expected, but a minimum is obtained for around 4-5 EOFs. If a larger number of EOFs are considered the rmse tends to increase, indicating that the reconstruction is overfitting the starting data distribution. Table 3.2 shows the variance, as a percentage, of the five leading altimetry EOFs, which expresses the best balance for capturing a larger amount of field variance without introducing noise into the reconstruction. The lowest EOF modes are shown in Figure 3.3.

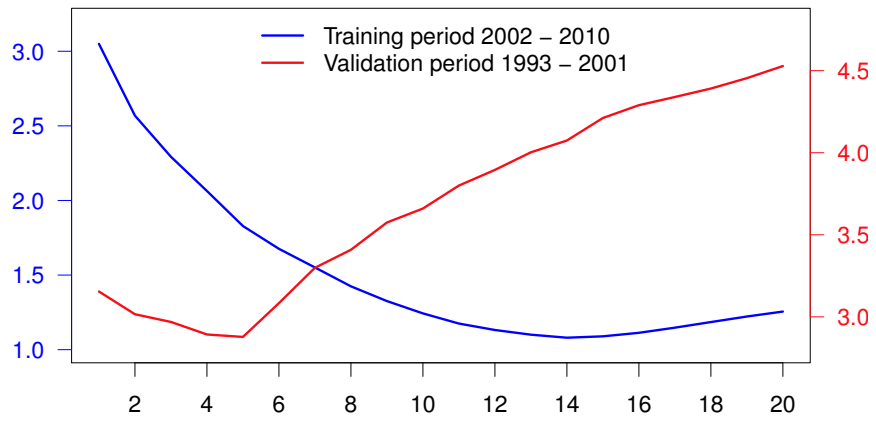

Figure 3.2: Optimal EOFs number selection. The x-axis is the number of EOFs considered; the y-axis indicates the rmse [cm] obtained comparing altimetry and reconstructions over the training period (2002 - 2010; blue line). The 2nd y-axis indicates as before the rmse [cm] between the two datasets obtained over the validation period (1993 - 2001; red line).

	Variance
EOF 1	38.07
EOF 2	11.34
EOF 3	5.68
EOF 4	5.37
EOF 5	3.48
Tot	63.9

Table 3.2: Variance accounted by EOFs (%)

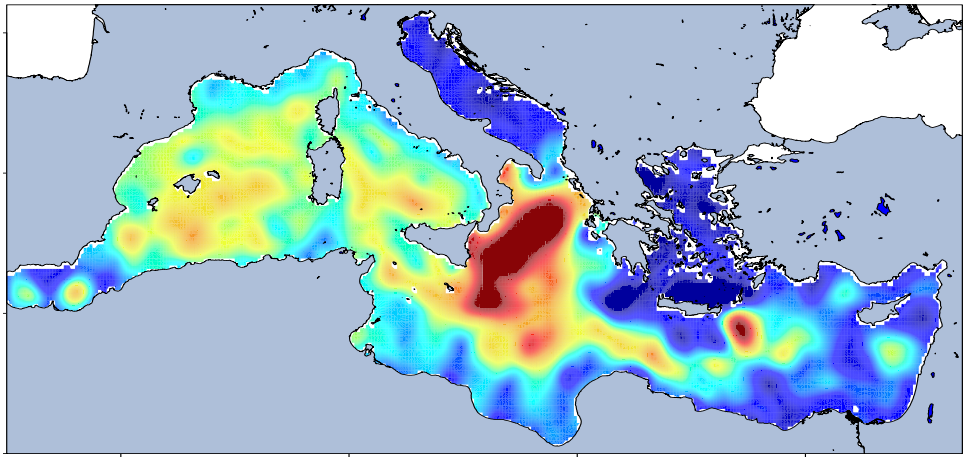

(a) EOF1

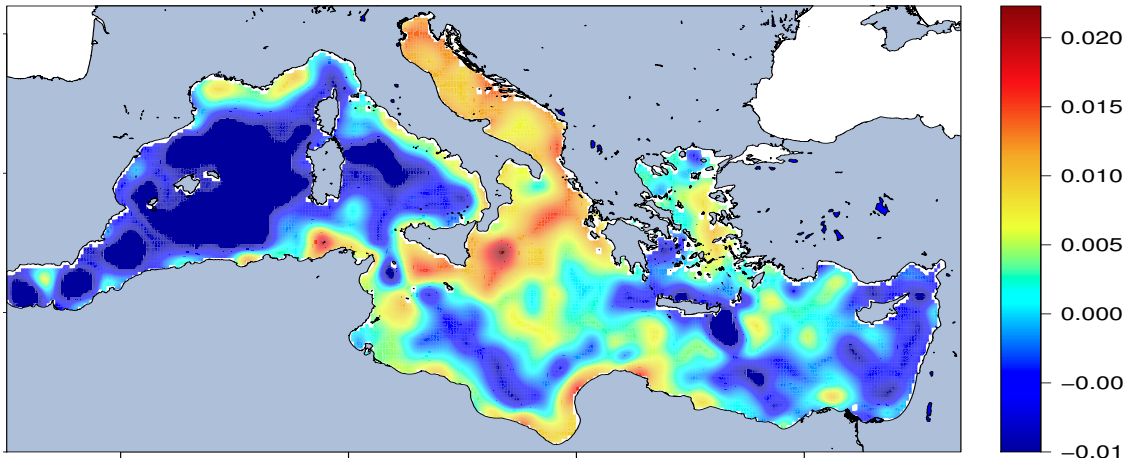

(b) EOF2

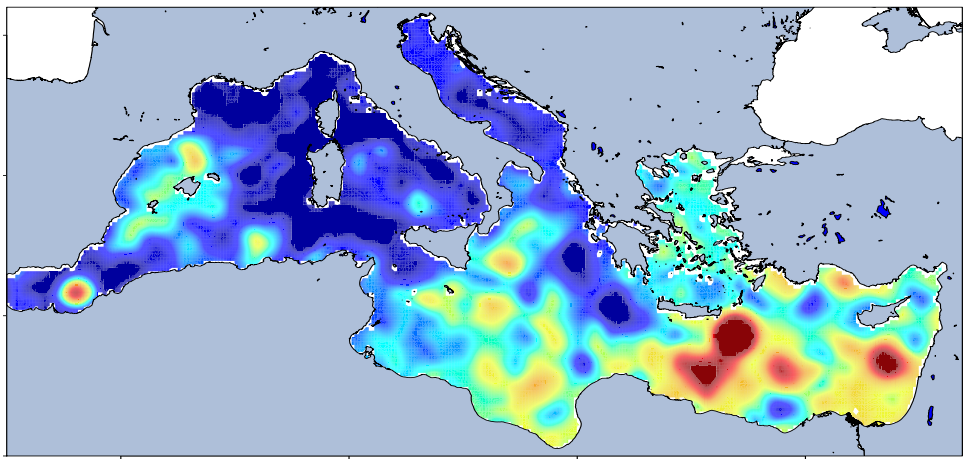

(c) EOF3

Figure 3.3: Satellite altimetry EOFs.

3.4 Reconstruction validation for the satellite era

The sea-level reconstruction obtained has been validated at the basin scale using satellite altimetry data from the period 1993 to 2010. The reconstructed field capture the sea-level spatial variability expressed by the satellite altimetry maps, in particular in coastal areas where the shelf is extended, and in general where the mesoscale activity is not intense.

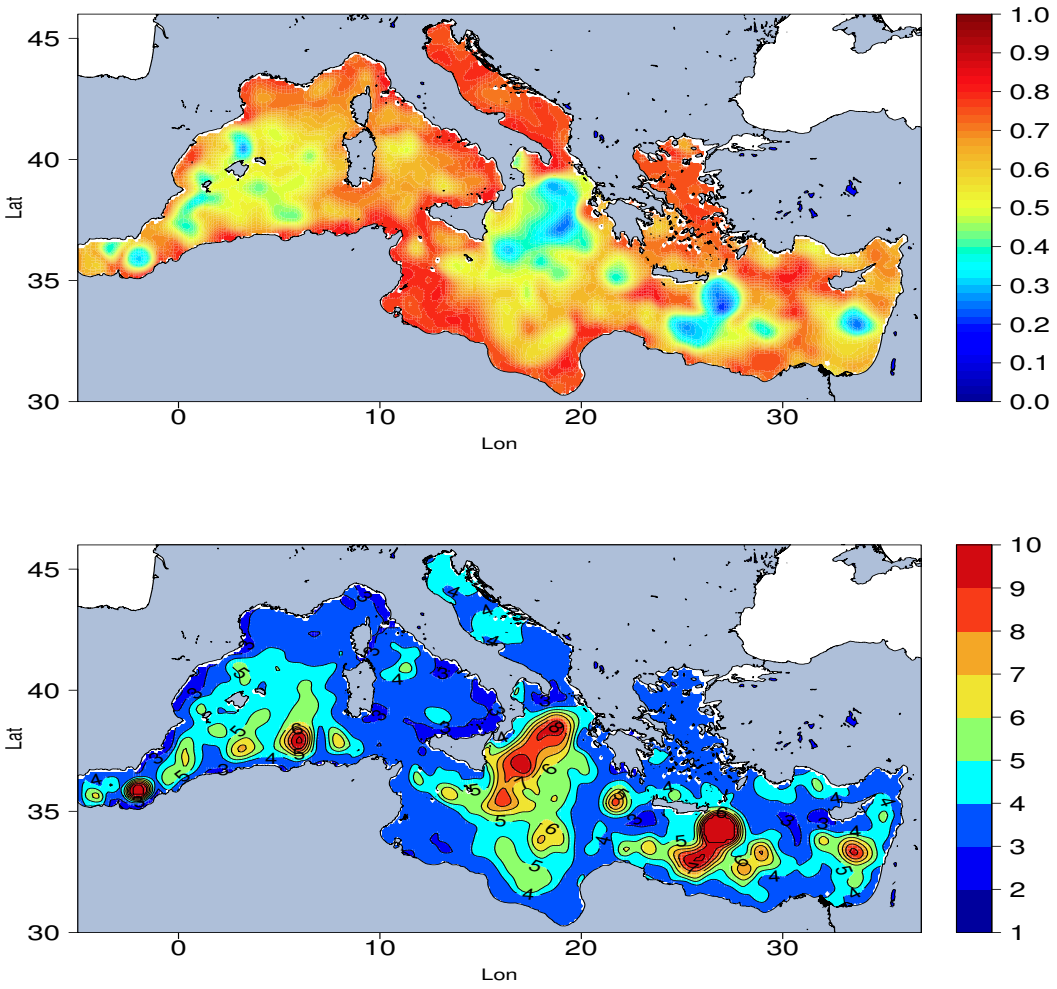

Figure 3.3: Reconstruction and satellite altimetry comparison (1993 - 2010). Top panel: correlation map. Bottom panel: root mean square error $[cm]$; contour lines interval 1 cm.

Figure 3.3 shows the correlation pattern and the root mean square error between satellite altimetry and reconstructed sea level for the satellite era. The two fields are highly correlated in the shallow water areas of the basin, while low correlation patterns are observed in those areas characterized by high variability in sea-level dynamics, as well as the high mesoscale structures of the basin, such as the South Cretan, Ierapetra, Shikmona and Mersa Matruh gyres in the Levantine basin, and the Alboran gyre in the western part of the basin. Even the Ionian gyre reversal is not well reproduced by the reconstruction. Low correlation patterns could be due to a number of factors: i) the EOF space reduction used in the reconstruction method does not permit resolution of the sea-level field in these high variability areas; ii) unnormalized EOFs have been used for sea-level reconstruction, which tends to capture most of the sea-level signal variance in the shallow water areas; iii) EOF stability in the different parts of the basin. This last aspect involves the definition of sub-regions in order to obtain different set of EOFs in different areas. Sub-regions should be defined considering as sub-domains boundary areas where variance tends to zero. Often the choice of sub-domains for EOF analysis is carried out arbitrarily, avoiding cutting regions characterized by high signal variance. A method to account for EOF domain shape dependency and sub-domain instability is to consider rotated EOFs (Richman, 1986). Further analysis will be carried out in order to perform sea-level reconstructions obtained using normalized and rotated EOFs.

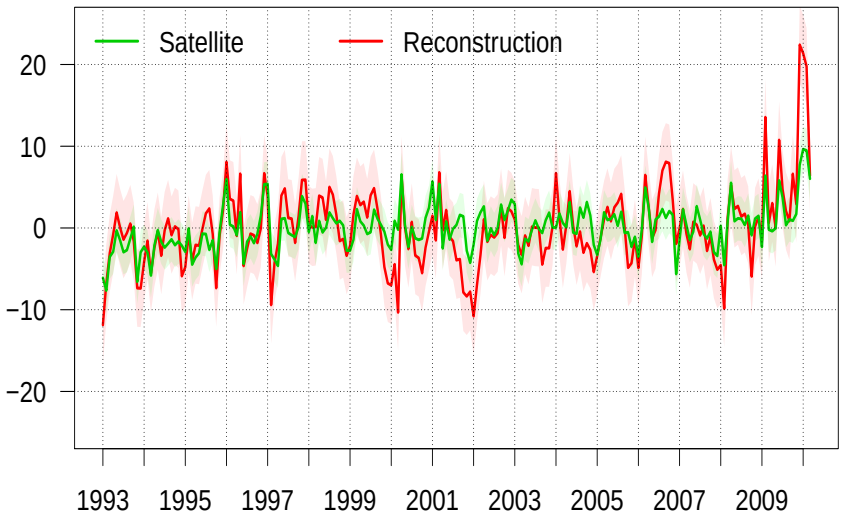

Figure 3.4: Basin mean sea level [cm] from reconstruction (red line) and satellite altimetry (green line).

The basin mean reconstructed sea level is closely comparable with the altimetry over the entire time period, with a correlation of 0.8 and a root mean square error of 2.7 cm (Figure 3.4) .

3.5 Reconstruction validation before than satellite era

One way to validate the reconstruction in the period before 1993 is to compare the results with tide-gauge time series locally. Sampling the reconstructed sea level in the tide-gauge positions, the two datasets have been compared during each reconstruction sub-period. Figure 3.4 shows the comparison between the reconstruction and tide gauges throughout the basin. In the northern part of the basin (where tide-gauge stations are concentrated), the reconstruction, as expected, reproduces the local sea level variability represented by tide-gauge records well. It is interesting to notice that the same condition is found relative to stations located in the southern part of the basin (Port Said, Egypt) and in areas where

the sea-level dynamic is very complex, such as around Crete (Souda). In general, the two datasets are highly correlated at the local scale during each sub-period, ranging between correlation coefficients of 0.8 and 0.9, both as signal amplitude and time evolution.

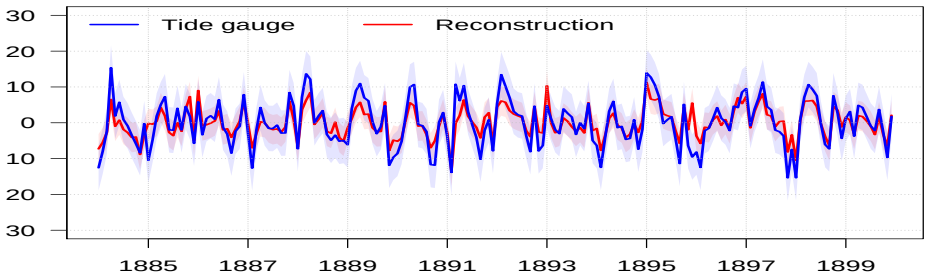

(a) Genova

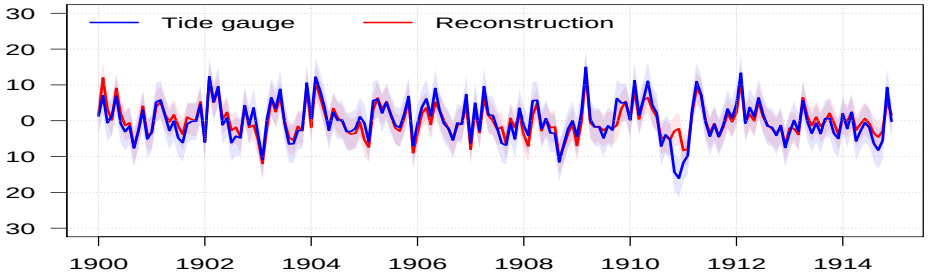

(b) Palermo

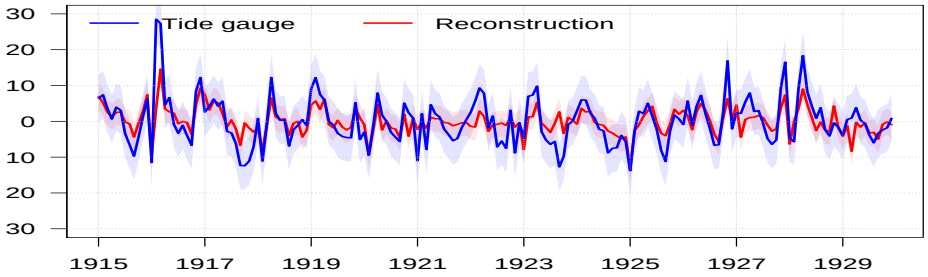

(c) Marseille

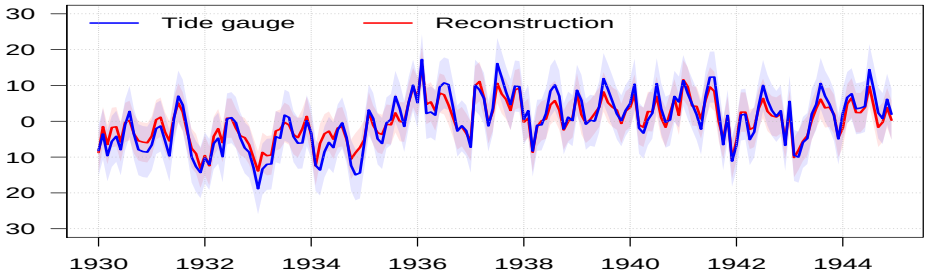

(d) Port Said

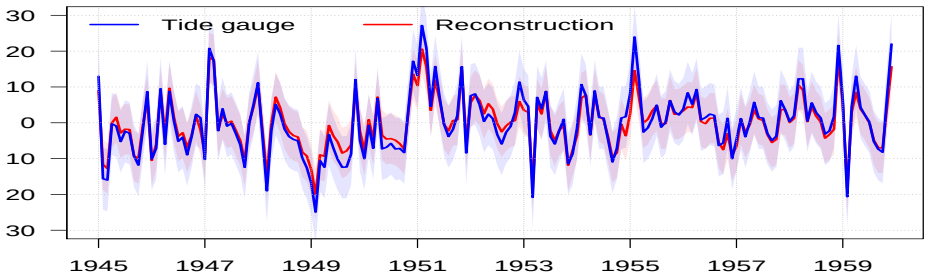

(e) Venezia

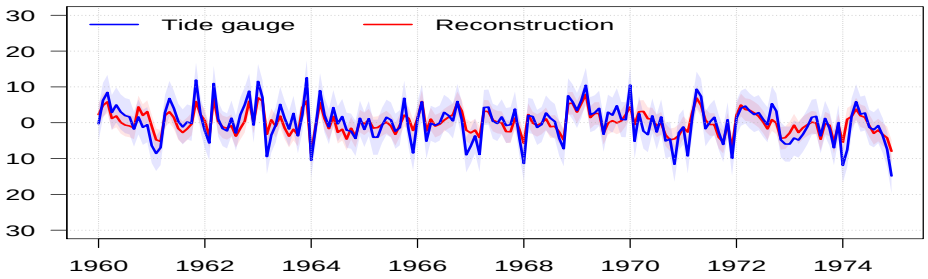

(f) Alicante

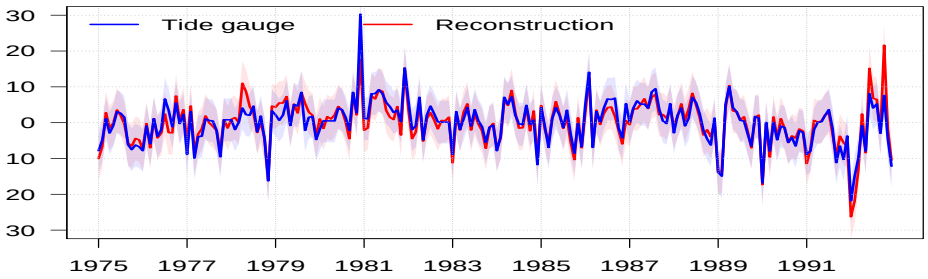

(g) Souda

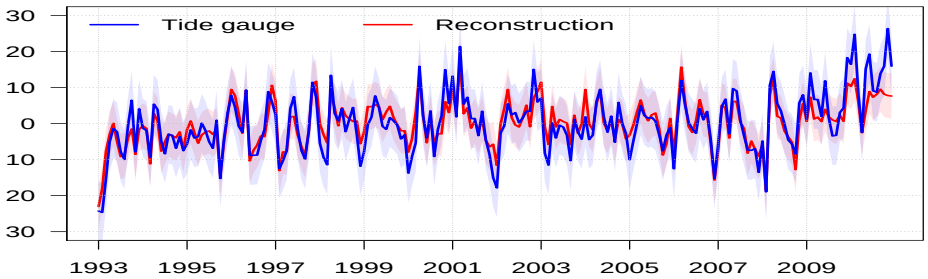

(h) Trieste

Figure 3.4: Comparison between reconstruction and tide-gauges.

3.5.1 Sea-level trends over decadal time scales

Sea-level trend spatial variability estimated from the reconstructed field is comparable with that obtained directly from altimetry data for the period 1993-2010 (see Chapter 2, Figure 2.5). Positive sea-level trends have been found in the western ($3mm\ yr^{-1}$) and Levantine basins ($10\ mm\ yr^{-1}$; Pelops gyre), and more than $5\ mm\ yr^{-1}$ are observed in the northern Adriatic. The reconstruction also reproduces the negative trend of more than -10 $mm\ yr^{-1}$ observed in the Ionian Sea from the altimetry. Figure 3.2 shows the differences between the reconstruction and altimetry trend spatial variabilities, where significant (top panel).

Looking at the trend over the multidecadal time scale, over the whole reconstruction period 1885-2010 no significant mean sea-level trend has been found ($0.1 \pm 0.1\ mm\ yr^{-1}$; Figure 3.3). At this time scale, the spatial distribution trend mainly shows the presence of positive rates in the basin, reaching 0.5 mm $mm\ yr^{-1}$ in the eastern part. The Ionian shows a negative rate of ~ 0.3 $mm\ yr^{-1}$, as does the dipole structure of the Ierapetra gyre.

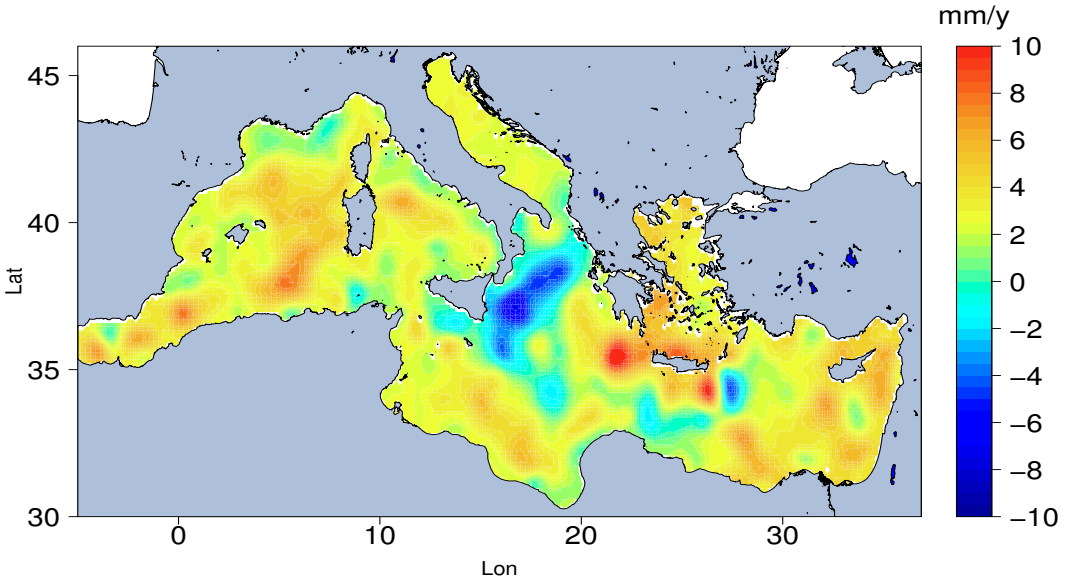

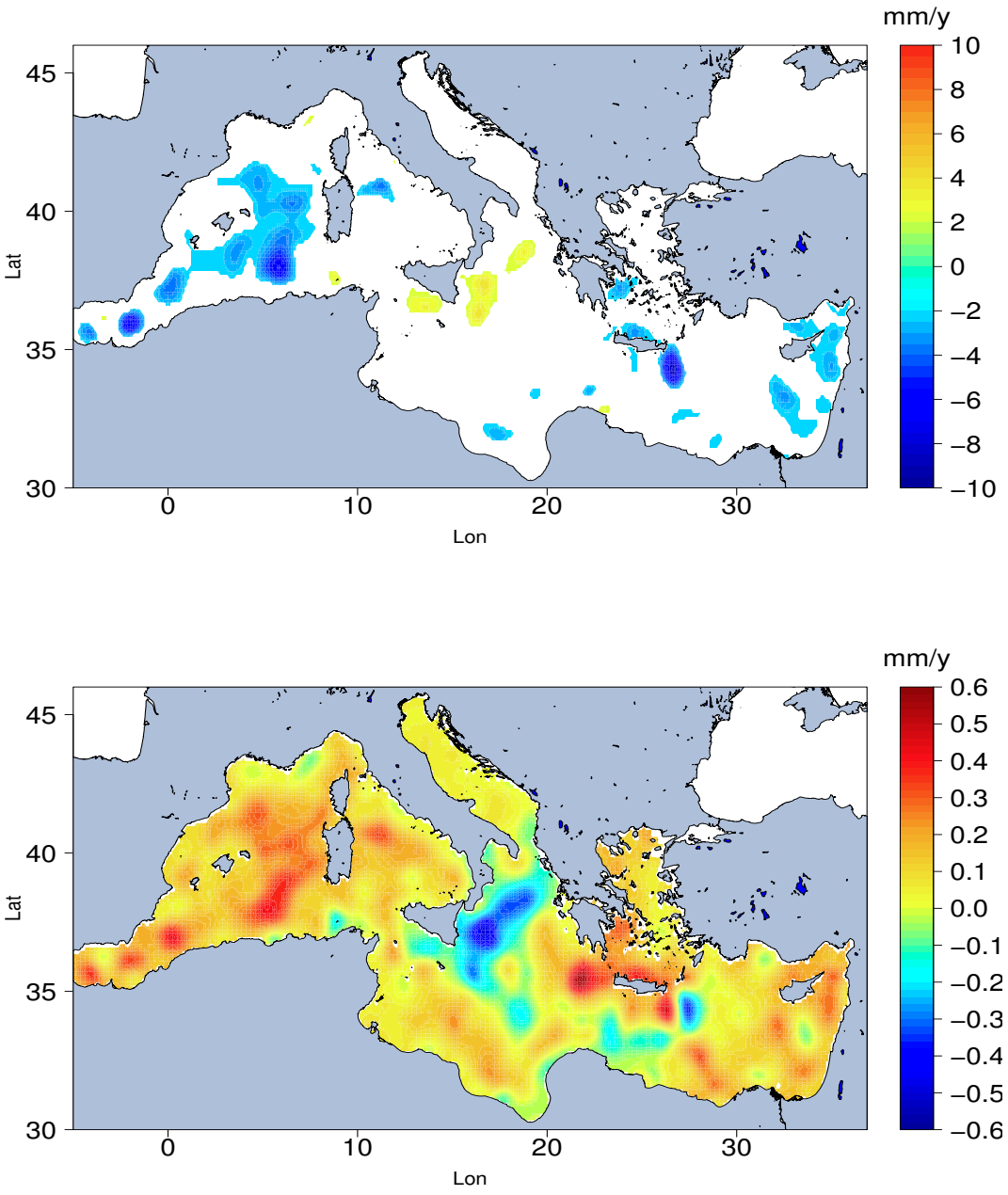

Figure 3.2: Spatial variability of trend. Top panel: reconstructed sea-level trend during the period 1993 - 2010. Middle panel: difference between satellite altimetry and sea-level reconstruction trends, for the period 1993 - 2010. Absolute differences inferior to 2 $mm\ yr^{-1}$ are not shown. Bottom panel: reconstructed sea-level trend during the period 1885 - 2010.

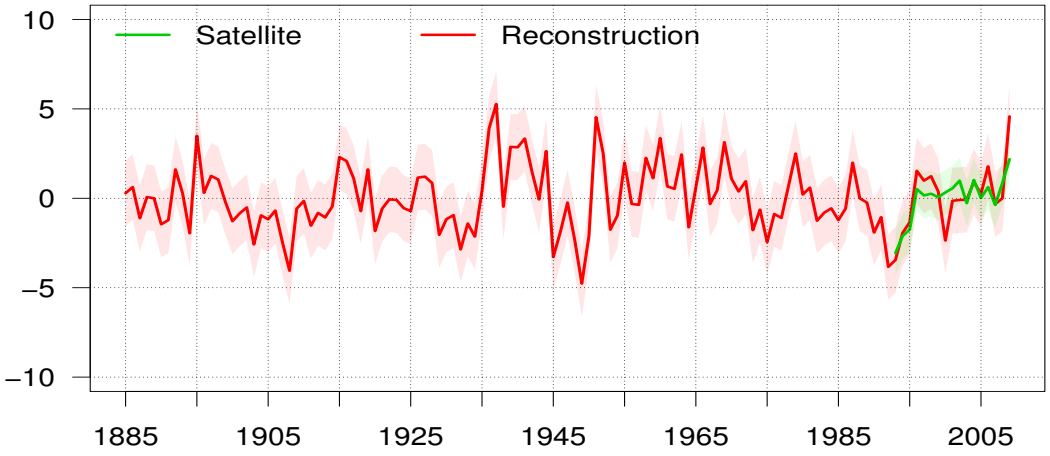

Figure 3.3: Sea-level reconstruction from 1885 to 2009: the red line shows the annual mean of sea-level reconstruction; the green line is the satellite altimetry annual mean during the period 1993-2009. The standard deviation range is shown with shading.

Looking at the mean sea-level time evolution during the whole reconstruction period (1885-2010), we can identify different periods characterized by positive and negative trends (Figure 3.3). In particular, it is interesting to notice the sea-level trend variability over different time scales. Figure 3.4 shows the results obtained considering all the possible sea-level trends as function of the length of the period considered. Values are shown as changes in annual sea level, defined as the trend multiplied by period length (Liebmann *et al.*, 2010), in order to emphasize the trend differences. Over the decadal and multidecadal time scales (up to 25 years), a sea-level trend with alternate positive and negative phases is observed.This is particularly significant (> 95 % t-test) starting from the middle of the twentieth century. Over the long time scale, stable positive trends have been found considering a period of a minimum of 90 years, starting from the eighteen-nineties (99 % t-test).

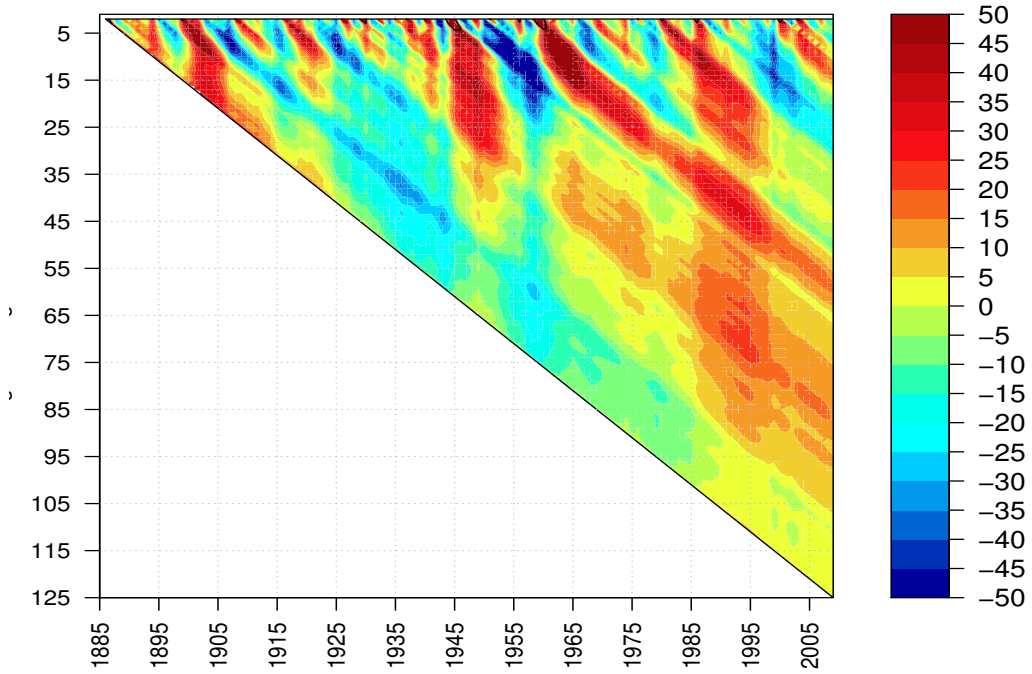

Figure 3.4: Change in reconstructed annual sea-level as a function of the length of the period considered. Change is defined as the sea-level trend multiplied by the number of years over which the trend is estiamted $[mmyr^{-1}]$. The y-axis expresses the length of the period considered (years) for estimating the trend; the x-axis indicates the ending year of the period considered. Year-by-year trends are not shown.

3.6 Case study: the Tunisian coast

The Tunisian coast in general and the area of the Gulf of Gabs in particular, are representative examples of coastal areas, like other Mediterranean coastal areas, exposed to several anthropogenic and natural pressure such as the Nile Delta (Egypt) and the Gulf of Oran (Algeria).

As has already been said, in the southern part of the Mediterranean basin, in-situ data (tide gauges) are not available, and it was thus not possible to use the data of this area for sea-level reconstruction. On the other hand, the total lack of sea-level historical data makes it necessary to look at data sources that can provide at least a basis for knowledge of sea-level variability over a long time scale.

Reconstruction data were validated sub-sampling the satellite altimetry and the reconstruction datasets in the study area and comparing the data in terms of correlation and trend spatial variability for the period 1993-2010. Figure 3.6 (bottom right panel) shows the high correlation between sea-level reconstruction, except in the reconstructions around the areas of the Strait of Sicily, where the high ocean dynamic in this area is not totally resolved by the limited number of EOFs used in the reconstruction (§3.3.1. Satellite altimetry trend distribution has a homogeneous pattern in this part of the basin, showing positive rates in the order of 2 $mm\ yr^{-1}$ (Figure 3.6, top left panel) over the period 1993-2010, which is very well reproduced by the reconstructed sea level (top right panel).

Figure 3.5: Study Area.

Sea-level reconstruction results give a result in the study area close to zero ($\sim 0.15\ mm\ yr^{-1}$) for the whole reconstruction period (bottom left panel). This result is also confirmed locally, selecting the reconstruction data in target positions along the Tunisian coasts corresponding to sensitive areas such as cities along the coast (Gabs, Monastir), islands (Galite, Kerkennah), industrial centers (Sfax) and coastal lagoons (Bizerte). The placemarks in the study area map show the positions of the coastal areas selected (Figure 3.5). The decadal and centennial sea-level trends were estimated in each seleted location in order to be used in the Tunisian coastal areas environmental risk assessment and integrated into itthe framework of the Climate and Anthropogenic Drivers and Impacts for the Tunisian Coastal Area (CANTICO) project (Table 3.3).

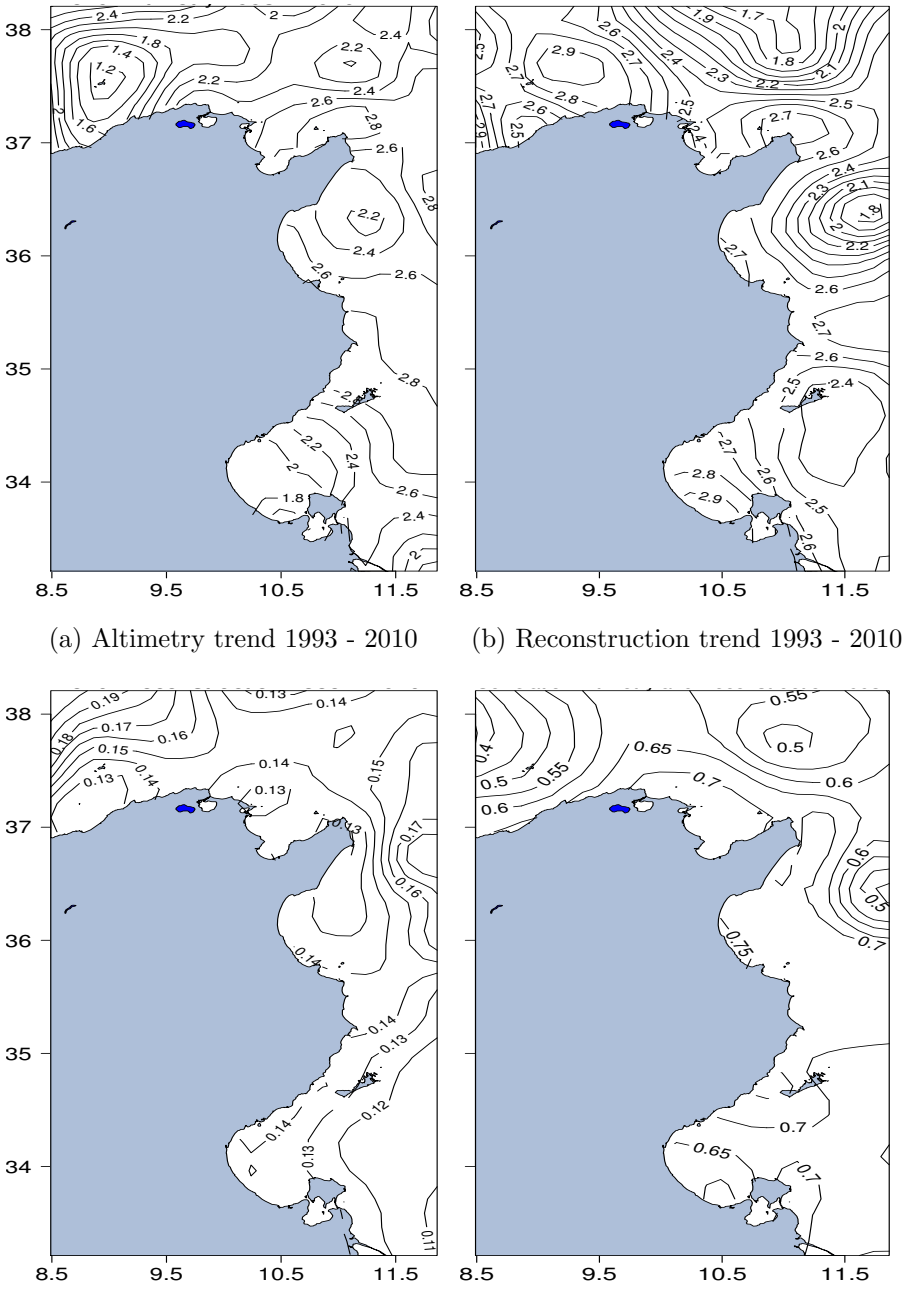

(a) Altimetry trend 1993 - 2010 (b) Reconstruction trend 1993 - 2010

(c) Reconstruction trend 1885 - 2010 (d) Correlation map 1993 - 2010

Figure 3.6: Satellite altimietry and sea-level reconstruction along the Tunisian coasts. Top panels: satellite altimetry (right) and reconstructed sea-level trend spatial variability, for the period 1993 - 2010 $[mm\ yr^{-1}]$. Bottom panels: sea-level reconstruction trend distribution for the period 1885 - 2010 (left)$[mm\ yr^{-1}]$; satellite altimetry and reconstruction correlation pattern for the period 1993 - 2010 (right).

	NAME	lon	lat	C	1885-2010	1993-2010
1	GALITE	8.95	37.50	0.49	0.14	1.93
2	CAPSERRAT	9.22	37.23	0.65	0.13	1.77
3	ZEMBRA_ZEMBRETTA	10.78	37.13	0.72	0.15	2.12
4	KURIAT	10.57	35.88	0.77	0.15	2.21
5	KEKENNAH	11.27	34.75	0.71	0.13	1.86
6	KELIBIA	11.08	36.83	0.70	0.12	1.89
7	NABEUL	10.73	36.43	0.74	0.14	2.07
8	BIZERTE	9.88	37.27	0.70	0.15	2.19
9	RAFRAT	10.18	37.20	0.72	0.14	2.03
10	RADES	10.28	36.77	0.75	0.16	2.13
11	SOLIMAN	10.47	36.73	0.75	0.16	2.13
12	MONASTIR	10.82	35.77	0.74	0.15	2.17
13	CARTHAGE	10.33	36.85	0.75	0.16	2.13
14	GOULETTE	10.32	36.83	0.75	0.16	2.13
15	GAMMARTH	10.27	36.92	0.75	0.16	2.13
16	SOUSE	10.88	34.82	0.76	0.15	2.10
17	QARQANNAH	11.03	34.63	0.72	0.14	2.14
18	SFAX	10.75	33.73	0.65	0.14	2.54
19	GABES	10.13	33.82	0.62	0.15	2.58
20	DJERBA	10.88	33.90	0.64	0.15	2.45
21	AGHIR	11.02	33.75	0.67	0.14	2.45

Table 3.3: Reconstruction and Altimetry comparison in target areas along the Tunisian Coast. Column 3 show the correlation coefficient (C) between the altimetry and the reconstruction time series. Columns 4 and 5 refer to the reconstruction trends computed over the period 1885 - 2010 and 1993 - 2010, respectively. Values expressed in $mm\ yr^{-1.}$

3.7 Summary

In this work the method described by Kaplan *et al.* (1997) and applied at a global scale by Church *et al.* (2004b) and Calafat & Gomis (2009) and Meyssignac *et al.*

(2011) in the Mediterranean has been applied in order to reconstruct the sea-level signal in the Mediterranean basin over the last century.

Observational datasets are fundamental for studying sea-level variability, both as in-situ and remote-sensing data. Tide-gauge data in the Mediterranean have long time series that cover a period of more than 100 years, while satellite altimetry provides spatially continuous information covering a time window of almost 20 years. Sea-level reconstructions aim at merging the two sea-level signals, using leading satellite altimetry EOFs and the tide-gauge time series projected over an altimetry spatial domain. In this sense, the in-situ data distribution plays a key role, conditioning the number of EOFs that it is possible to use to reconstruct the signal, as well as the final skill of the reconstruction. The optimal number of EOFs to be used in the reconstruction has been established repeating an experiment carried out in Calafat & Jordà (2011) for our specific purposes. Defining training (2002-2010) and validation (1993-2010) periods, the best number of EOFs is found comparing the results of several reconstructions obtained increasing the number of EOFs against the altimetry and reconstruction root mean square variations. The results show that considering 5 EOFs is the best solution for resolving a larger amount of field variance ($>$ 60 % of variance), avoiding overfitting.

The reconstruction obtained has been validated through comparison with altimetry during the satellite era (1993-2010). The correlation pattern between reconstructed and satellite-observed sea level shows that reconstruction captures the observed signal all over the basin, except in areas with high mesoscale activity that is not well resolved by the reconstruction due to the limited number of EOFs considered.

The spatial variability trend for the period 1993-2010 is also well reproduced in the reconstruction, showing high positive trends in the eastern part of the basin and smaller positive ones in the western part, up to + 5 $mm\ yr^{-1}$ in the northern Adriatic, and strong negative trends in the Ionian (- 10 $mm\ yr^{-1}$) . The basin mean sea level is well comparable with altimetry, with a correlation of 0.8 and a root mean square error of 2.7 cm.

The reconstruction has been validated for the past comparing the results with tide-gauge records. As expected, in the northern part of basin (where tide-gauge

stations are concentrated), the data are comparable and highly correlated in all the cases considered (0.8 - 0.9). It is interesting to note that the same correlation pattern is also found in the southern part of the basin, in the case of Port Said (Egypt).

Looking at the trend distribution over a centennial time scale, results show a less marked spatial variability trend than is found at a decadal scale, with positive trends all over the basin; these reach 0.6 $mm\ yr^{-1}$ in the eastern part. The Ionian, on the other hand, shows negative rates up to -0.3 $mm\ yr^{-1}$.

Looking at the mean sea level over the last century allows us to identify different periods characterized by positive, negative or neglectable trends. In particular, it is interesting to notice the trend variations at different time scales over such a long time window. Considering sub-periods of 20-25 years (decadal time scale), sea-level trends flip between positive and negative phases, in particular starting from the middle of the last century. On the other hand, considering more than 90 years of data it is possible to observe a stable and significant (99 %) positive trend, starting from the eighteen-nineties.

Sea-level reconstruction is a useful instrument for investigating the sea level in the Mediterranean, and offers a consistent method for compensating the limitations of observational data temporal and spatial distributions.

Sea-level reconstructed data has been used within the framework of the CANTICO project to characterize sea-level variability over the last century along the Tunisian coast, where long in-situ temporal records are not available. In this part of the basin, focusing in particular in the Gulf of Gabs, we observe a reconstructed sea-level trend close to zero (0.15 $mm\ yr^{-1}$) over the whole reconstruction period (1885-2010). Sea-level trends estimated in target sensitive coastal areas have been integrated into the study area environmental risk assessment within the framework of the CANTICO project.

Chapter 4

The Mean Sea-Level equation and its application to the Mediterranean Sea

4.1 Sea-level theoretical studies

The global mean sea-level trend has been shown to be a useful indicator of climate change and ocean heat content variability (IPCC, 2007). Recently, satellite altimetry analysis studies (Cazenave & Llovel, 2010) have re-evaluated the mean sea-level trend from satellite altimetry and tide-gauge records and found that thermal expansion and mass changes may be equally important contributors to the global mean sea-level trend. However, theoretical investigations into the dynamics of the mean sea level have received relatively less attention. Greatbatch (1994) proposed a simplified version of the Mean Sea-Level Equation (MSLE). In our study we formulate a fully consistent MSLE that takes into account all processes contributing to it. Such an equation can be used to test different dynamical hypotheses and allows the diagnosis from complex datasets of the terms responsible for the trend. The MSLE can then be used to estimate the mean sea-level tendency and trends from numerical models or observational datasets. We will construct a consolidated formalism for the mean sea-level equation that can be used for reference in different studies.

Greatbatch (1994) and Mellor & Ezer (1995) were the first to try to to define the mean sea-level equations and contributing factors, and they succeeded in showing the importance of steric effects in determining mean sea-level changes. We want to generalize their approach and write a complete mean sea-level equation for any limited region, as well as for the global ocean. We will then apply the formalism to the Mediterranean, where important lateral fluxes at Gibraltar add complexity to the dynamics of the mean sea-level change, and determine for the first time the different dynamical contributions to the mean sea-level trend in this region. We will use the recent high-resolution re-analysis data set computed for the Mediterranean Sea (Adani *et al.*, 2010) in order to study a realistic model solution. The aim is to understand the balance between the steric and mass effects in this region and extract the contribution of each term to the regional mean sea-level tendency.

The paper is constructed as follows: Section 4.2 illustrates the formalism and writes the mean sea-level equation. Section 4.3 evaluates the different terms contributing to the Mediterranean mean sea-level tendency equation due to each of them. Section 4.4 overviews the conclusions for the Mediterranean and discusses issues related to the required accuracy of the estimates of terms contributing to the mean sea-level tendency.

4.2 Mean sea-level equations (MSLEs): global and regional MSLs

The sea-level equation is normally obtained considering the continuity equation (Gill, 1982; Pedlosky, 1987; Mellor & Ezer, 1995)

$$\nabla \cdot \vec{u} = -\frac{1}{\rho}\frac{D\rho}{Dt} \tag{4.1}$$

where $\frac{D}{Dt} = \frac{\partial}{\partial t} + \vec{u} \cdot \nabla, \vec{u} = (u, v, w)$ is the three-dimensional velocity field and ρ the ocean density field. In order to obtain the sea-level equation we need to vertically integrate

(4.1) between η and H (Fig. 4.1) using the kinematic and dynamic boundary

conditions at

the two vertical boundaries of the fluid (Apel, 1987), i.e.:

$$w_{z=\eta} = \frac{D_2\eta}{Dt} + q_w \tag{4.2}$$

$$w_{z=-H} = -\vec{u}_{z=-H} \cdot \nabla H \tag{4.3}$$

where η is the sea level, $\frac{D_2}{Dt} = \frac{\partial}{\partial t} + u \cdot \nabla, (u_z = \eta, v_z = \eta)$ and

$$q_w = E - P - \sum_i R_i/A_i - M_G/C \tag{4.4}$$

is the fresh water flux composed of E evaporation, P precipitation, R_i river runoff and A_i their cross-sectional areas. M_G is the fresh water runoff from glacier melting and C the cross-sectional area over which the melting-ice runoff occurs. The freshwater budget is composed of the land (R_i and M_G) and ocean (E and P) components of the water cycle. The different terms have widely differing time scales and variability, and they result in a multiple-time-scale forcing term.

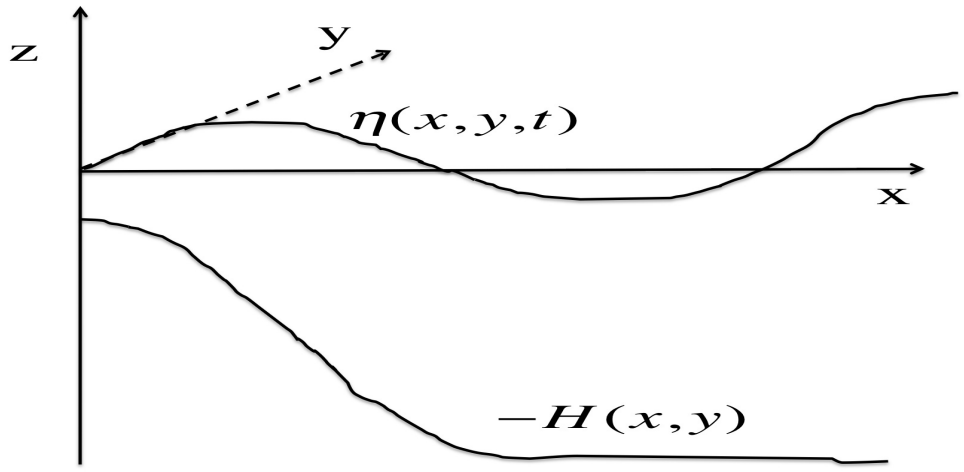

Figure 4.1: The notation of the paper and the system of reference: η is the free surface and $-H$ the bottom topography.

Before integrating in the vertical we make the assumption that $\rho = \rho_0 + \rho^{'}$, where ρ_0 is a constant such that $\frac{\rho^{'}}{\rho_0} << 0$ (Cushman-Roisin, 1994) and (4.1) can be written as

$$\nabla \cdot \vec{u} = -\frac{1}{\rho_0}\frac{D\rho'}{Dt} \tag{4.5}$$

Integrating in the vertical (4.5) we now obtain the compressible sea-level equation:

$$\frac{\partial \eta}{\partial t} + \nabla \cdot [(H+\eta)\vec{\bar{u}}] = -q_w - \frac{1}{\rho_0}\int_{-H}^{\eta} \frac{D\rho'}{Dt} dz' \tag{4.6}$$

where

$$\vec{\bar{u}} = \frac{1}{H+\eta}\int_{-H}^{\eta} \vec{u} dz'$$

is the barotropic velocity field. We now need to simplify the right-hand side of (4.6) and in order to do so we consider the following explicit form of the equation

of state:

$$\rho = \rho_0 + \rho' = \rho_0 + \rho_f[-\alpha_T(T - T_f) + \beta(S - S_f)] \tag{4.7}$$

where $\alpha_T = -\frac{1}{\rho_f}\frac{\partial}{\partial T}\,|_{T=T_f}$ is the thermal expansion and $\beta = -\frac{1}{\rho_f}\frac{\partial}{\partial S}\,|_{S=S_f}$ is the haline contraction coefficient as a function of z, (T_f, S_f) are reference temperature and salinity profiles and ρ_f is a constant reference value for the density anomaly (Marshall & Plumb, 2008).

Given (4.7), we can re-write the right-hand side of (4.6) using the first law of thermodynamics and the salinity equation (Pedlosky, 1987):

$$\frac{D\rho'}{Dt} = \nabla \cdot (K_h \nabla \rho') + \frac{\partial}{\partial z}(K_v \frac{\partial \rho'}{\partial z}) \tag{4.8}$$

where K_h is the horizontal and K_v the vertical diffusion coefficient. The surface boundary condition for (4.8) is

$$K_v \frac{\partial \rho'}{\partial z}\,|_{z=\eta} = -B \tag{4.9}$$

where B is the scaled buoyancy flux (Marshall & Plumb, 2008):

$$B = \alpha_T \frac{Q}{C_w} - \rho_f \beta S_0 q_w \tag{4.10}$$

where S_0 is the surface salinity field, Q is the net flux of heat into the ocean (negative during the night), C_w is the specific heat capacity of seawater, and the remaining symbols have already been discussed. If we now substitute the right-hand side of (4.8) into (4.6) and take the vertical integral we obtain

$$\frac{\partial \eta}{\partial t} + \nabla \cdot [(H + \eta)\vec{u}] = -q_w - \frac{1}{\rho_0}\left[\int_{-H}^{\eta} \nabla \cdot (K_h \nabla \rho')dz' - B\right] \tag{4.11}$$

where we assumed the bottom density flux to be zero. The mean sea level, indicated by $\langle \eta \rangle$, is calculated by taking the average value of η over the area Ω using the operator:

$$\left\langle \right\rangle = \frac{1}{\Omega}\int\int_{\Omega} d\Omega$$

Finally the mean sea-level equation is then written as:

$$\frac{d\langle\eta\rangle}{dt} = -\frac{T_r}{\Omega} - \langle q_w\rangle + \frac{\langle B\rangle}{\rho_0} - \frac{F_p}{\rho_0} \tag{4.12}$$

Here we considered for general purposes an open domain where:

$$T_r = \int\int_{\Omega} \nabla\cdot\vec{u}d\Omega = \oint_{\partial\Omega} \vec{u}\cdot\vec{n}dl$$

$$F_p = \int\int_{\Omega} \nabla\cdot(K_h\nabla\rho')d\Omega = \oint_{\partial\Omega} K_h\nabla\rho'\cdot\vec{n}\cdot dl$$

T_r is the net volume transport out of the domain and F_p is the outward flux of density, and both are positive in the regional outward direction. If we now insert the definition of B into (4.12), we obtain the final form of the mean sea-level equation:

$$\frac{d\langle\eta\rangle}{dt} = -\frac{T_r}{\Omega} - \langle q_w\rangle - \frac{\rho_f\beta\langle S_0 q_w\rangle}{\rho_0} + \frac{1}{\rho_0}\langle\alpha_T\frac{Q}{C_w}\rangle - \frac{1}{\rho_0}\int_{-H}^{\eta}\oint_{\partial\Omega} K_h\nabla\rho'\cdot\vec{n}\cdot dl \tag{4.13}$$

$$= \quad (1) \quad (2) \quad (3) \quad (4) \quad (5)$$

There are five terms contributing to the mean sea-level tendency. Term (1) is the net lateral volume transport across the domain which decreases the mass in the domain if T_r is positive (i.e., in the outward direction) and term (2) is the net addition of water by surface and lateral land runoff processes. These two terms correspond to the mass tendency terms and compose the mean sea-level tendency in incompressible models. We will call them collectively the incompressible terms. The other three terms come from the compressible part of the continuity equation and are often referred to as steric effect terms, even though they have not been explicitly written this way before. Term (3) is a term due to the salinity vertical boundary effects which we call halosteric, but, to the best of our knowledge, it has never been explored before. Term (4) is the thermosteric flux term and (5)

the diffusive density flux out of the domain. The latter depends on the volume transport and density at the lateral open boundary (i.e., in the Mediterranean the Strait of Gibraltar). A simplified form of Eq. (4.14) has been studied by Greatbatch (1994) for the global ocean only, and only with thermosteric effects. If the domain is the global ocean, the boundary terms disappear and for the global mean sea level, $\langle \eta_G \rangle$, the tendency equation is:

$$\frac{d\langle \eta_G \rangle}{dt} = -\langle q_w \rangle - \frac{\rho_f \beta \langle S_0 q_w \rangle}{\rho_0} + \frac{1}{\rho_0} \langle \alpha_T \frac{Q}{C_w} \rangle \tag{4.14}$$

4.3 Evaluation of the mean sea-level in the Mediterranean Sea

A re-analysis of Mediterranean Sea climate state variables for the past 23 years has recently been produced (Adani *et al.*, 2010). The re-analysis is 1/16 x 1/16 degrees with 71 vertical levels of resolution, and covers the period from January 1985 to December 2007. The hydrodynamics model uses incompressible primitive equations and the domain extends into the Atlantic, so the fluxes at the Strait of Gibraltar are determined by the combined dynamics of surface fluxes and lateral inflow. In this section we will evaluate the single terms in Eq. (4.13) using monthly mean re-analysis fields, determining the different contributions to the mean sea-level tendency.

The model is Boussinesq, incompressible and hydrostatic, and thus uses a simplified form of Eq (4.5), i.e.:

$$\vec{\nabla} \cdot \vec{u} = 0$$

In order to evaluate the mean sea-level tendency due to both incompressible and steric terms, we will evaluate all the terms in Eq. (4.13) a posteriori from the model re-analysis. Mellor & Ezer (1995) has indicated that such a procedure is valid for long time scales and large basin scales.

In Figure 4.2 (top panel) we show all five terms in Eq. (4.13): as expected the transport at Gibraltar, the water flux term and the thermosteric term are the largest contributors, followed by the halosteric term and, finally, the density

advection term, which is seven orders of magnitude smaller than the first ones. We note that the Gibraltar transport and water flux terms almost balance to zero, thus giving an overall small contribution to the tendency. The thermosteric term oscillates around zero and in a time-integral sense will dominate the mean sea-level fluctuations, as shown in Figure 4.2.

The MSLE thus contains a periodic term from the thermosteric and halosteric terms and a small stochastic noise term given by the mass terms. It is very challenging to integrate in time this kind of equation, a stochastic differential equation (SDE). The stochastic part is due the balance between water flux and the transport at Gibraltar (Figure 4.2, middle panel), which does not happen synchronously, but rather with a temporal delay that results in stochastic variations of the sea-level tendency. This temporal delayed balancing process between transport at Gibraltar and water flux increases the high variability of the mean sea-level tendency mass component. As investigating the mean sea-level tendency variability is the one of the general objectives of this study, we look at the mean sea-level tendency signal without introducing any lag correction for mass terms balance, which would reduce their temporal discrepancy.

Integrating the MSLE numerically in time, this stochastic component can cause a numerical error that tends to grow very quickly.

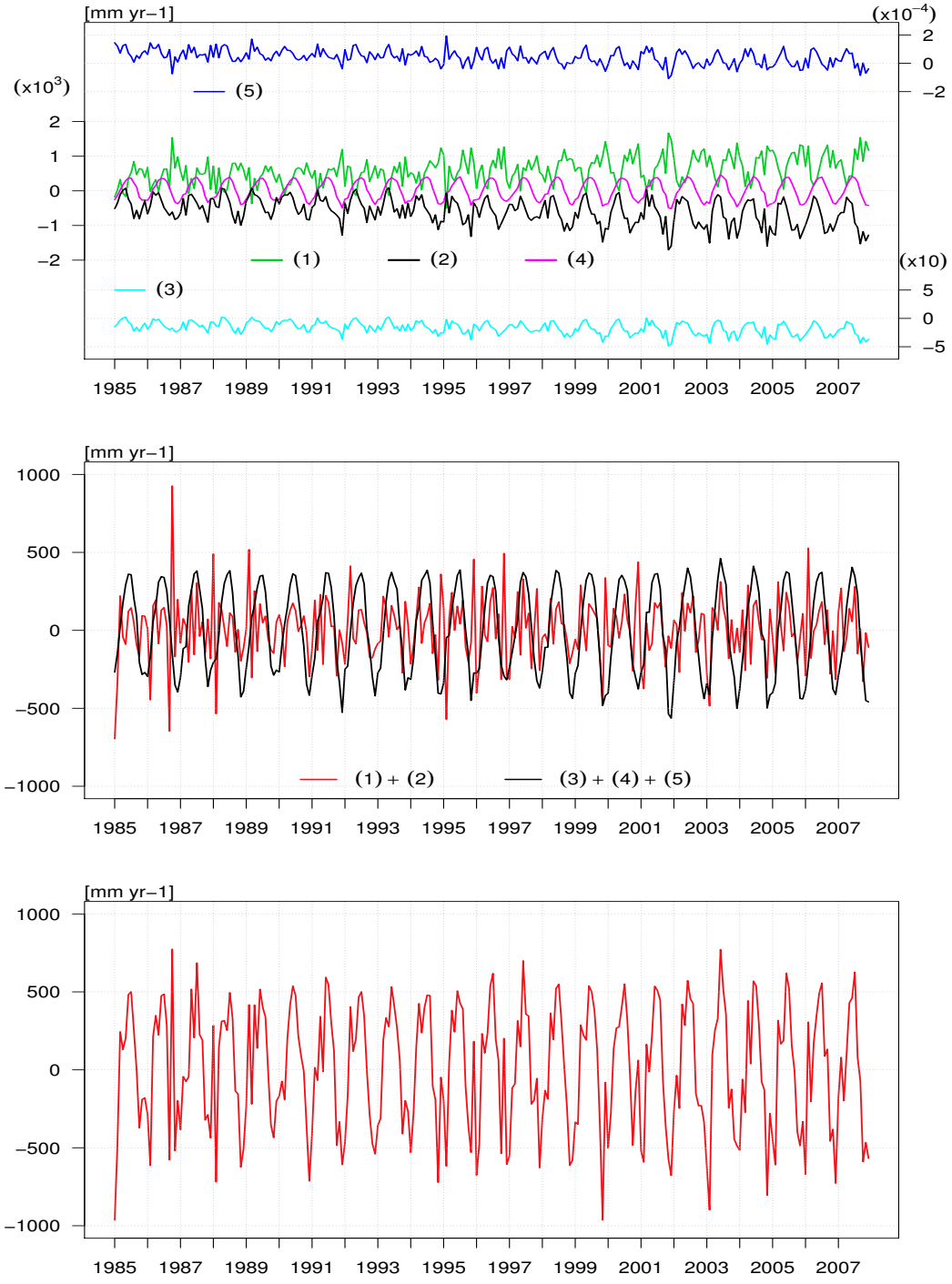

Figure 4.2: Mean sea-level tendency from re-analysis dataset. Top panel: mean sea-level tendency contributions. Numbers refer to the terms of Eq. 4.13: transport at Gibraltar (1; green line), water flux (2; black line), halosteric term (3; cyan line), thermosteric term (4; violet line) and trasport of density (5; blue line). Middle panel: sea-level tendency mass and steric contribution. Mass and steric contributions as resultant of terms (1) + (2) (red line) and (3) + (4) + (5) (black line) respectively. Bottom panel: resultant mean sea-level tendency (red line). Values expressed as $[mm\,yr^{-1}]$.

A sensitivity study was carried out looking at the integration numerical error variations, sampling the model data with a different temporal frequency. The mean sea-surface height of the numerical model, which as said before accounts only for the incompressible part of the equation, has been considered as a test variable, as it results only from the terms (1) and (2) of Eq. (4.13).

Considering monthly data, numerical error increases after a few iterations to values comparable with the order of magnitude of the variable, even when using a Runge-Kutta second-order accuracy integration method.

Using the NEMO Ocean General Circulation Model (OGCM) (Oddo *et al.*, 2009), a simulation was performed to study the application of MSLE in the Mediterranean and investigate numerical error, according to the sampling frequency of terms (1) and (2) of Eq. (4.13). Sampling the data at the same temporal frequency that the model uses to integrate the variables (at the model time step of 600 sec.) it was possible to integrate the mass contribution terms (1) and (2), obtaining a numerical error one order of magnitude lower than that of the variable. Figure 4.3 (top panel) shows the numerical error for a sampling frequency of 600 sec. Even when considering the data at each time step, the integration numerical error tends to grow. Figure 4.3, bottom panel, shows the comparison between the model sea-surface height (solid blue line) and the solution obtained integrating terms (1) and (2) (dashed red line) restarted every year. In this way we can reduce the error to values of 1-2 % (3 mm) with respect to the absolute $\langle \eta \rangle$ changes between seasons. The choice of restarting has been adopted to minimize the numerical error, as well as not to affect the intra-annual variability of MSLE terms in order to obtain a consistent final solution. Runge-Kutta integration methods (Cash & Karp, 1990) are in general more computationally expensive than the simple Euler forward method. We notice that restarting the numerical integration every year results as being no more computationally expensive than integrating the MSLE terms with a second order Runge-Kutta method providing a unique initial condition.

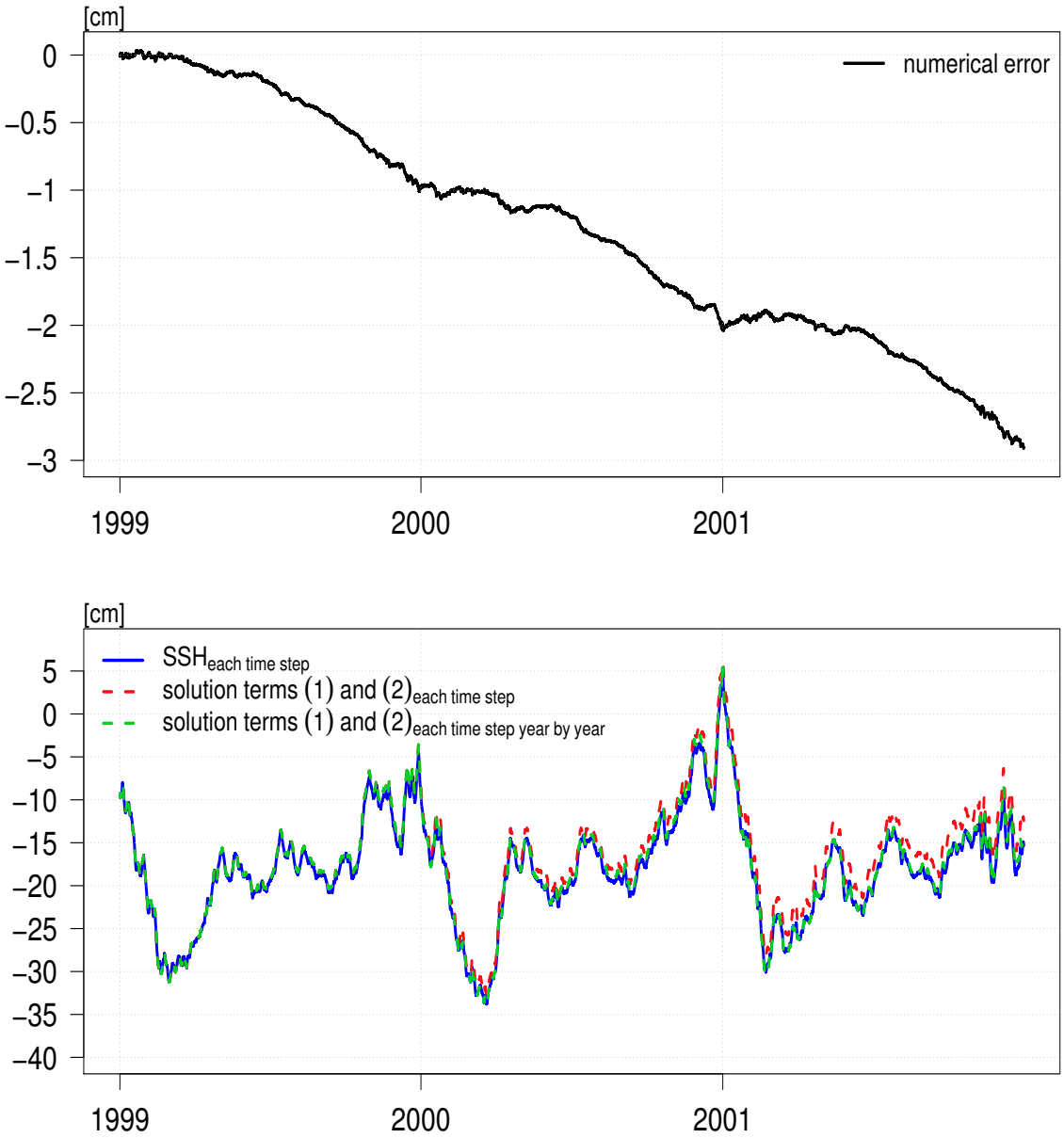

Figure 4.3: Comparison between sea-surface height and mean sea-level equation terms (1) and (2). Top panel: integration numerical error (black line), considering model data at each model time step (600 sec.). Bottom panel: sea-surface height model variable (solid blue line); water flux(1) and transport (2) time integration considering the entire time window (1999 to 2001; dashed red line) and integrating between adjacent years (dashed green line). Values expressed as $[mm\,yr^{-1}]$ (monthly mean).

Looking at the mean sea-level components estimated from the simulated data, results confirm those obtained using re-analysis data. Figure 4.4 show the results obtained with the model simulation for the period 1999-2001. Results are shown as monthly means so as to be comparable with those obtained using the re-analysis dataset. A difference between the two datasets is found in the contribution of the the lateral flux at Gibraltar (Figure 4.4, green line), which shows a larger range of variation in the simulation dataset. This difference is attributable to the different systems used: re-analysis was realized using a closed domain model (Adani *et al.*, 2010), while the model used in the simulation is an Atlantic-Mediterranean nested model (Oddo *et al.*, 2009) with open boundary conditions.

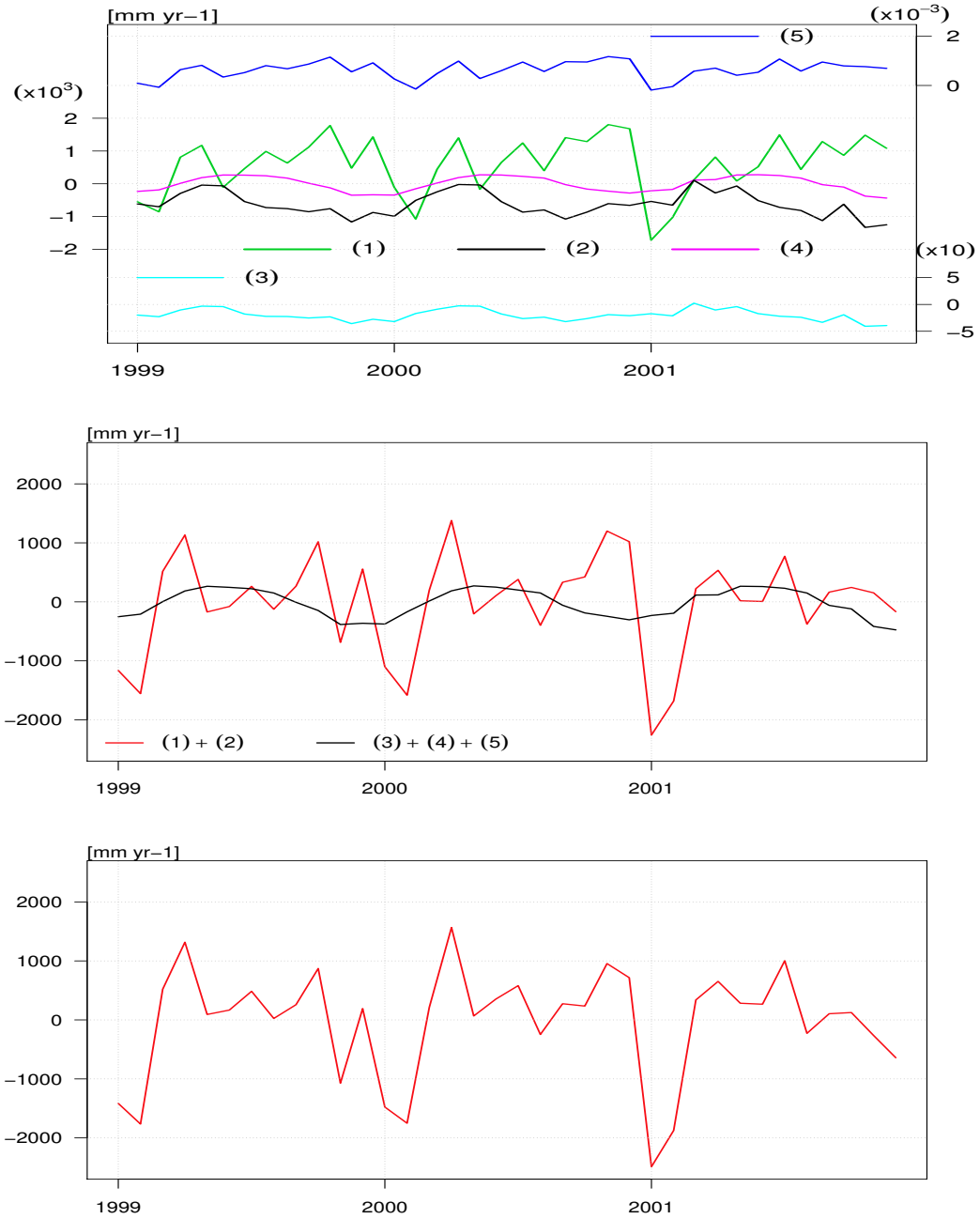

Figure 4.4: Mean sea-level tendency from model simulation data. Top panel: mean sea-level tendency contributions. Numbers refer to the terms of Eq. 4.13: transport at Gibraltar (1; green line), water flux (2; black line), halosteric term (3; cyan line), thermosteric term (4; violet line) and the term due to the trasport of density (5; blue line). Middle panel: sea-level tendency mass and steric contribution. Mass and steric contributions as resultant of terms (1) + (2) (red line) and (3) + (4) + (5) (black line) respectively. Bottom panel: resultant mean sea-level tendency (red line). Values expressed as $[mm\,yr^{-1}]$ (monthly mean).

4.4 Summary

In this work a fully consistent MSLE has been formulated. At the global scale the contributions are due to water flux (2) (as defined in 4.2), which accounts for the mass variation component, and the halosteric (3) and thermosteric (4) components, which together represent the steric variations (Eq. 4.14). Considering a regional basin it is also necessary to consider the mass flux due to lateral fluxes, which in our particular case is the volume transport (1) and the density flux (5) at Gibraltar.

The case study of the Mediterranean Sea has been considered to evaluate the terms in the MSLE. The values of all 5 terms of the mean sea-level equation, have been estimated starting from the Mediterranean Sea Ocean Re-analysis monthly mean data (Adani *et al.*, 2010). Water flux and transport make an important contributon to the mean sea-level tendency in the basin, with a transport that tends to balance loss of water associated with water flux, which is typical of an evaporative basin such as the Mediterranean. The thermosteric component also makes an important contribution, with an expected periodic temporal variability, followed by the halosteric component and density advection component, which have smaller amplitudes.

The balance between Gibraltar transport and water fluxes produces a term that has a stochastic form. This represents the stochastic part of the mean sea-level equation which is similar to a stochastic differential equation. Integrating this kind of equation is very difficult, as the stochastic component can cause a large numerical error. To investigate the integration numerical error variations, we considered the time step sampling frequency from a numerical model simulation and it was found that it is possible to reduce the integration error significantly if a restart is done every year (i.e., after approximately 50000 time steps).

Comparing the results obtained using ocean re-analysis and simulation datasets, differences have been found in the Gibraltar transport amplitudes. Simulation data shows a larger range of variation associated with the lateral volume transport with respect to the one obtained using re-analysis data. This is due to the different model configuration between re-analysis and simulation: the former was realized using a closed domain model, while the latter is an Atlantic-Mediterranean nested

model with open boundary conditions. Simulation shows a dominance of mean sea-level tendency mass contribution with respect to the steric one during the period 1999 to 2001, which could be due to the capability of nested models also to consider the Atlantic waters mass increase associated with ice melting.

More work is needed to reach conclusions about the possible causes of MSL variability, taking into consideration an analysis period of at least 10 years.

Chapter 5

Atmospheric pressure effects on sea-level variability over a medimum range temporal scale

5.1 Sea-level response to atmospheric pressure

Sea-level changes are the result of various processes acting at different temporal and spatial scales. Over the medium-range temporal scale (from monthly to interannual), atmospheric pressure is one of the main drivers of sea-level change, contributing, with the wind, to water mass redistribution.

The North Atlantic Oscillation (NAO; Figure 5.1) is a large-scale variation in atmospheric pressure between the Azores and Iceland that dominates the atmosheric variability in the Atlantic (Hurrell, 1995), and also influence the heat and water fluxes in southern Europe and in Mediterranean (Hurrell & Deser, 2009; Pettenuzzo *et al.*, 2010). The NAO can affect freshwater fluxes that contribute to the sea-level mass balance, and sea-level pressure anomalies that produce the inverse barometer effect (Tsimplis & Josey, 2001).

Several studies in the literature focus on the sea-level response to atmospheric forcings using observations and model data. In the past, most studies about sea-level response to barometric forcings were realized using global barotropic genearl circulation models (Ponte *et al.*, 1991), which consider a constant density ocean

and do not allow vertical stratification. With the advent of the satellite altimetry era, this kind of data has also been used to investigate effects of pressure on sea level (Dorandeu & Le Traon, 1999b), which underlines the importance of considering a non-constant mean atmospheric pressure to improve the inverse barometer effect evaluation.

Studies in the Mediterranean show that the sea-level response to atmospheric pressure is a process that is strictly time-frequency dependent. Using T/P altimetry, ECMWF atmospheric pressure data for 3 years (October 1992-October 1995), and a simplified analytical circulation model (Candela, 1991), Le Traon & Gauzelin (1997) finds an improvement in the coherence of inverse barometer effect calculated from observations and models filtering out the higher frequencies from mean sea-level and atmospheric pressure signals. Tsimplis (1995) focuses attention on the temporal scale of the atmospheric pressure changes, looking at the response of the sea level when a low pressure cell establishes itself rapidly, representing the initial phase of sea-level extreme events . Tsimplis *et al.* (2005), studying the atmospheric pressure and wind contributions to sea-level trends using the tide-gauges data in the Adriatic, and the NCEP/NCAR re-analysis (Kalnay *et al.*, 1996), argues that the atmospheric forcings amplify or decrease sea-level trends following the NAO phases. Marcos & Tsimplis (2007), using tide-gauge data and numerical ocean model data forced by a dynamic downscaling of the NCEP/NCAR dataset (Sotillo *et al.*, 2005), shows that both atmospheric pressure and wind make an important contribution to sea level in the Mediterranean, tending to lower the sea-level trend during the period between 1960 and 2000.

The improvement of the capabilities of the numerical models to simulate the sea-level dynamic, moving to free-surface formulations instead of rigid lid approximations, allows studies on sea-level response to forcings, both in the present and in climate scenarios (Somot *et al.*, 2006).

This work aims to evaluate the effect of atmospheric pressure on sea-level in the Mediterranean in terms of variability, temporal evolution, phase and signal composition. In order to achieve this objective, the model data of the Mediterranean Forecasting System (MFS; Oddo *et al.*, 2009; Pinardi & Coppini, 2010), obtained considering implicit and explicit free-surface formulations, have been

used, applying the ECMWF (6h; 0.5°) atmospheric pressure forcing at the model vertical boundary. In particular, the Italian tide-gauge stations along the Italian coast have been chosen to understand the sea-level response to different forcings and model numerical approximations.

This chapter is organized as follows: Section 5.2 describes the model configuration and experiment set-ups chosen to investigate atmospheric pressure influence on sea level. In Section 5.3 the Italian tide-gauge network is described and the model simulations are validated. In Section 5.4 a description of the atmospheric forcings distributed by the European Center for Medium-Range Weather Forecasts (ECMWF) is given referring to the mean sea-level pressure (MSLP) and the atmospheric set-up of the sea surface. In the second part of the section, the data processing to compare model output with in-situ data is described. Section 5.5 shows the comparison between satellite altimetry data and model simulations at basin scale. Section 5.6 shows the results of the comparison between observations and model datasets for sea-level time evolution and spectral analysis. All the specific results described in the previous sections are summarized in Section 5.7.

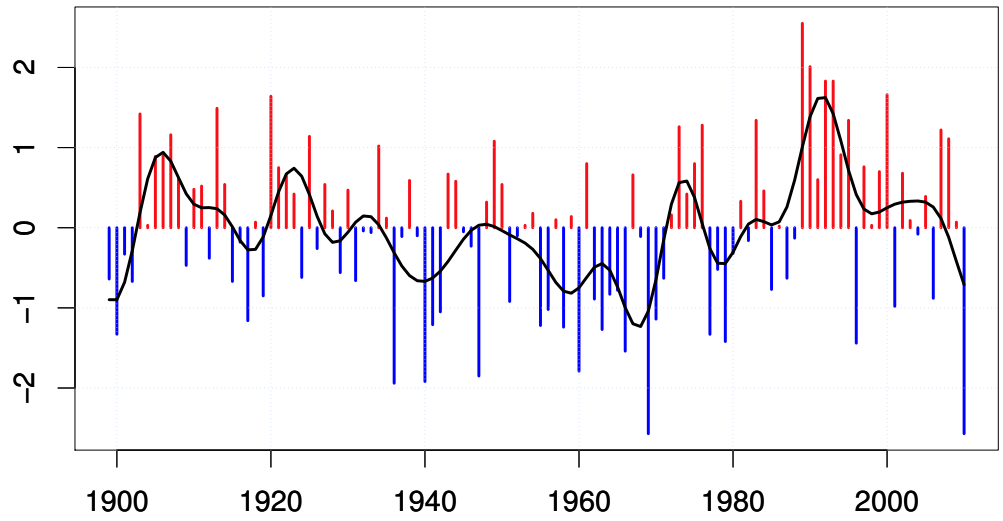

Figure 5.1: Mean Winter (DJFM) North Atlantic Oscillation (NAO). Black solid line show the smoothing applied to remove fluctuations with a period shorter then 4 years (Hurrell & Deser, 2009) .

5.2 Experiment design

The OGCM used in this work is a free-surface version of the Ocean PArallelise code (OPA, Madec, 2008). The model domain covers the entire Mediterranean basin and a part of the Atlantic (Figure 2.1), with a horizontal resolution of 1/16 ° and 72 unevenly spaced vertical z-levels, with vertical partial cells to resolve the ocean bottom (Oddo *et al.*, 2009). The model is forced by momentum, water and heat fluxes interactively computed by bulk formulae using the 6-h, 0.5° horizontal-resolution operational analyses from the European Centre for Medium Range Weather Forecasts (ECMWF) (Pinardi *et al.*, 2003; Pettenuzzo *et al.*, 2010).

The free-surface forlmulation of the model involves the consideration of External Gravity Waves (EGWs) as a solution of the equations (Madec, 2008). Assuming the hydrostatic approximation, these waves are exclusively barotropic

with short temporal scales compared to the other wave-like processes inherit to the primitive equation dynamic. In the implicit free surface formulation (Roullet & Madec, 2000) these waves are filtered out. On the other hand, in order to consider the processes with short time scales as well, a non-linear free-surface formulation is necessary (Griffies, 2004).

Using both the implicit free-surface, hereafter called Filtered Free-Surface Model (FFSM), and the explicit formulations, hereafter called Time-Splitting Model (TSM), four simulations have been realized considering the atmospheric pressure forcing. Two simulations, hereafter DA1 and DA2, consider the FFSM and the TSM respectively, not applying atmospheric pressure forcing. Two other simulations, DA3 and DA4, have been set up like the other two, but consider the pressure atmospheric forcing. The experiments are summarized in Table 5.1.

In all the experiments, the model simulation data have been considered for the period from 2004 to 2007,as 10-day snapshots (as in Oddo *et al.*, 2009).

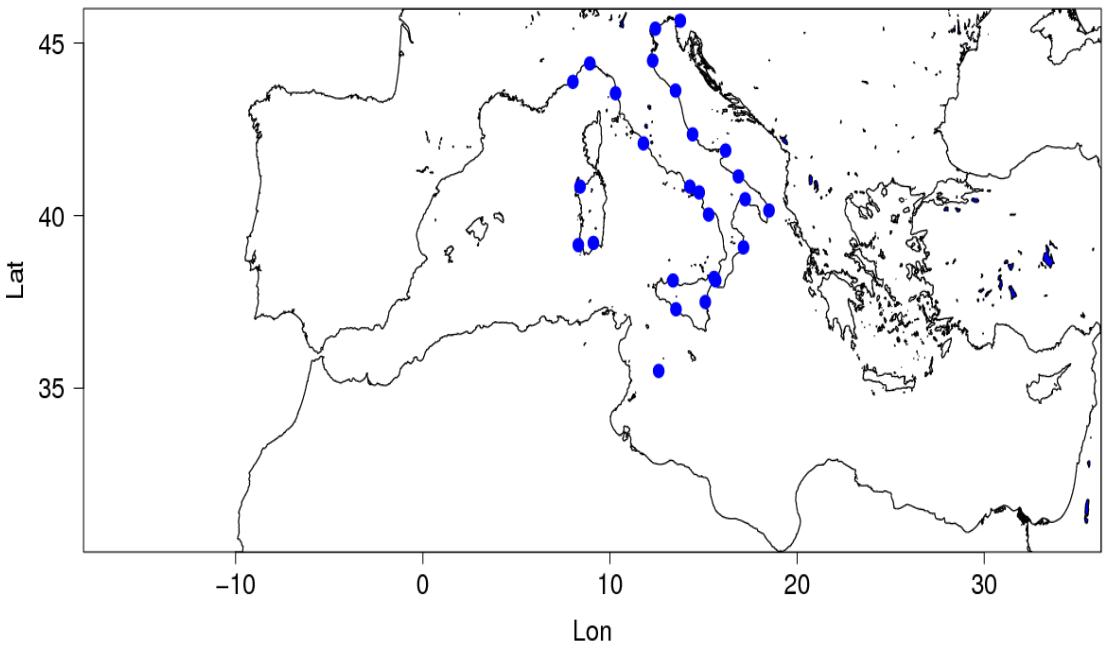

Figure 5.2: MFS spatial domain. Blue dots indicate the positions of ISPRA tide-gauge stations.

	Free Surface formulation	Atmosheric Pressure
DA1	Filtered Free Surface	NO
DA2	Time-Splitting	NO
DA3	Filtered Free Surface	YES
DA4	Time-Splitting	YES

Table 5.1: NEMO OGCM Configurations and Experiments set up. DA1 and DA2 experimens use the Filtered Free Surface and the Time-Splitting surface pressure gradient formulations respectively, without considering the atmospheric pressure at open lateral boundary conditions. DA3 and DA4 experiments have the same surface pressure gradient formulations of the previous two experiments, but consider the atmospheric pressure vertical boundary conditions.

5.3 Italian tide-gauge network

The Italian coastal tide-gauge network is managed by the Italian Institute for Environmental Research and Protection (ISPRA [1]), and it is compsed of 26 stations located all along the coasts of the Italian peninsula and islands. The longest time series cover a period from 1968 onwards. For the purpose of this study. tide-gauge data are sampled every ten days at midnight in order to consider exactly the same temporal frequency as the model simulations.

5.4 Atmospheric pressure data and inverse barometer effect

Atmospheric pressure data are derived from ECMWF operational products. The data have a temporal resolution of 6 hours and a horizontal resolution of 0.5 ° .

[1]ISPRA tide gauge network web portal: http://www.idromare.it.

These data are used as forcings for the model simulations, as well as to compute the sea-level inverse barometer (h_{IB}) [1] effect at the tide-gauge positions, following the formulation of (Dorandeu & Le Traon, 1999b):

$$h_{IB} = -\frac{1}{\rho_0 g} \ (Pa - P_{ref}) \tag{5.1}$$

MFS model adopts incompressibility and Boussinesq approximations and do not consider volume variations of the water column. This aspect means that the steric component has to be added to the sea-surface height output of the models in order to be comparable with observations in terms of physical signals

[1] From the hydrostatic equation:

$$\begin{aligned} P(x,y,t) &= Pa(x,y,t) + \int_z^h \rho g dz = \\ &= \int_0^h \rho_0 g dz + g \int_z^0 \rho dz = \\ &= Pa + \rho_0 g h + g \int_z^0 \rho dz \end{aligned}$$

where P is the sea surface pressure, Pa is the atmospheric pressure, ρ is the ocean density and ρ_0 the ocean reference density.

Considering now the equation:

$$\frac{Du}{Dt} - fv = -\frac{1}{\rho_0}\frac{\partial P}{\partial x} + Ib$$

and substituting we obtain

$$\frac{Du}{Dt} - fv = -\frac{1}{\rho_0}\frac{\partial Pa}{\partial x} - g\frac{\partial h}{\partial x} - \frac{g}{\rho_0}\frac{\partial}{\partial x}\int_z^0 \rho dz + Ib$$

In the previous equations the inverse barometer effect Ib is the process for which exists a free surface, called h_{IB}, for which:

$$-\frac{1}{\rho_0}\frac{\partial Pa}{\partial x} = g \ \frac{\partial h_{IB}}{\partial x}$$

$$h_{IB} = -\frac{1}{\rho_0 g} \ Pa$$

Pa can be defined as the anamoly with respect to a reference pressure value (P_{ref}) in order to not consider a mean h_{IB}:

$$h_{IB} = -\frac{1}{\rho_0 g}(Pa - P_{ref})$$

represented. In order to compare the model simulation results with observations, the steric effect has therefore been superimposed on the data following Mellor & Ezer (1995) :

$$\eta_{steric} = -\frac{1}{A} \int\int_A \left(\int_{-H}^{\eta} \frac{\rho - \rho_0}{\rho_0} dz \right) da \tag{5.2}$$

where A is the Mediterranean basin area, ρ is the ocean density (T, S, P) and ρ_0 is the reference density. Tide-gauge time series contain the entire sea-level signal. In order to compare the observations with model output not considering atmospheric pressure, the IB (§5.4) has been removed from tide-gauge data. Time-series analysis has been performed in order to compare coherent sea-level signals: 1) the data from the DA1 and DA2 simulations, once the steric component has been added, have been compared with tide-gauge data with the IB correction applied; 2) in the cases of DA3 and DA4, only the steric component has been added to the model data, keeping tide-gauge data with full signal.

In order to compare the model simulations with observations, the simulated data have been interpolated over the tide-gauge position, as described in Chapter 3.

The simulated and observed data have been analysed looking at the sea-level signal composition, performing a spectral analysis and applying a filter to the data in order to separate the low from the fast temporal scales of the processes contained in the signals.

5.5 Intercomparison between models and satellite data

Satellite altimetry data have been used to validate the model output all over the basin in order to estimate the models skill in reproducing the sea-level signal. Satellite altimetry data, as described in the previous chapters, are corrected for the inverse barometer effect, and therefore we present here the results of the comparison between satellite altimetry and model simulations DA1 and DA2, which do not consider the atmospheric pressure as vertical (Figure 5.3). Satellite

altimetry and numerical model data are compared over the same grid (1/8 °) and with the same sampling frequency (10 days).

Both model simulations have a high skill to reproduce altimetry data. In particular, model simulation DA2, which considers Time-Splitting as a free-surface formulation, shows higher correlation with satellite altimetry (0.9) and lower root mean square error (3 cm) with respect to simulation DA1 (0.8; 6 cm).

These first results indicate that at basin scale the sea-level signal is very well captured by the model, in particular using a Time-Splitting free-surface formulation that allows better resolution of the processes that have a faster temporal scale.

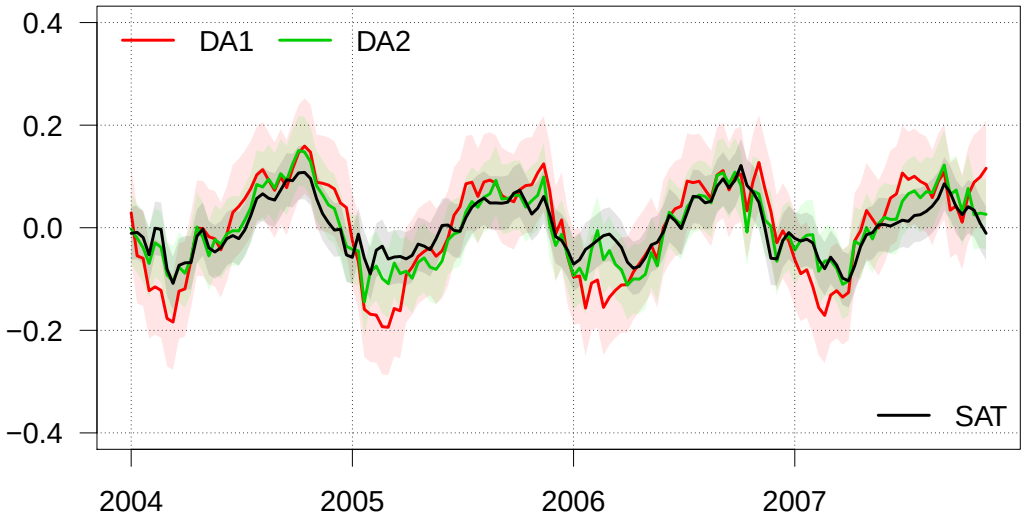

Figure 5.3: Mean sea-level time series from satellite observations (black line) and simulations DA1 (red line), DA2 (green line), DA3 (blue line) and DA4 (purple line). Shaded areas show the two standard deviation range.

5.6 Intercomparison between models and tide-gauge data

This section shows the results obatained averaging all the available data from tide-gauge station and models (sampled in station positions), comparing them as time series and power spectra. Table 5.2 summerizes the results obtained in the time-series analysis. In Figure 5.4 the mean sea-level time series obtained from simulations and observation datasets is shown, considering for each its own full signal.

Simulations DA3 and DA4 result as the most comparable with observations. In particular, DA4 is the simulation that best reproduces the sea-level amplitude and maximum and minimum peaks. DA1 results as the least correlated with observations, while DA2 and DA3 give similar results in terms of correlation pattern, though the latter shows a root mean square error (9 cm) higher than the former (7 cm), and signal amplitude results as being overestimated.

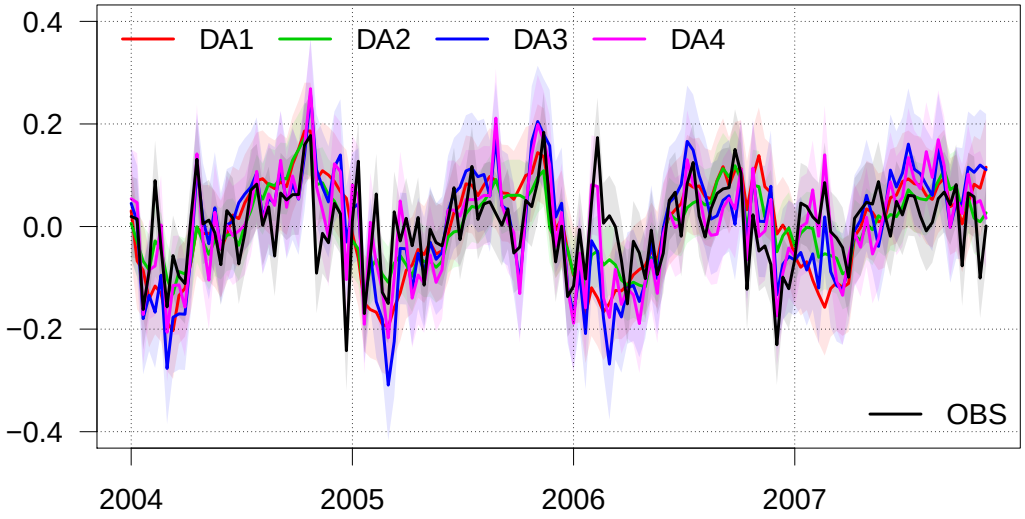

Figure 5.4: Mean sea-level time series from observations (black line) and simulations DA1 (red line), DA2 (green line), DA3 (blue line) and DA4 (purple line). Shaded areas show the two standard deviation range.

Once the IB has been removed from the observations, the results for DA1 and DA2 become very similar, although the phase and amplitude of the observation is better captured in DA2 (Figure 5.5). These results indicate that the atmospheric contribution adds a relative high-frequency signal to the sea level, which is not well captured by the DA1 model, which tends to filter out the high-frequency processes. On the other hand, in DA4, where a smaller time step is considered to resolve the barotropic variables and the atmospheric pressure, the sea-surface height is highly correlated with observations (~ 0.7). Once the atmospheric signal has been removed, the sea-level signal results as being mainly composed of slow processes (i.e., season cycle), and the DA1 model is capable of simulating the sea-surface elevation in a similar way to DA2.

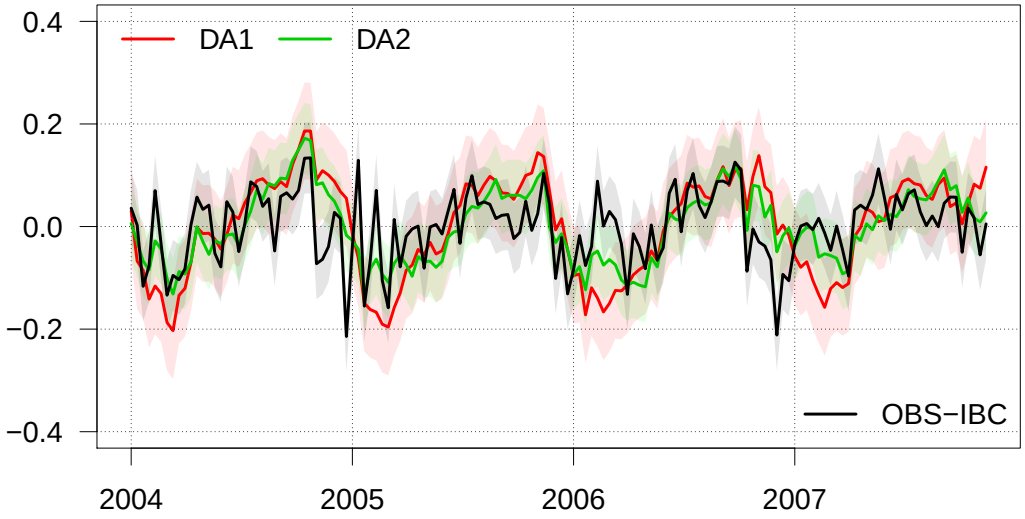

Figure 5.5: Mean sea-level time series from observations with the inverse barometer correction applied (OBS-IBC; black line), and simulations DA1 (red line), DA2 (green line) that do not consider the atmospheric pressure contribution. Shaded areas show the two standard deviation range.

This is also confirmed looking at the IB effect applied to the obserservation. Figure 5.6 shows the conparison between the IB directly computed from the ECWMF data, and atmospheric pressure contribution deducted from the model simulations (DA3-DA1 and DA4-DA2). In both the amplitude is overestimated, while maximun anomalies are captured, resulting in a signal correlation to the order of 0.5 with an *rmse* of 5 cm.

Signal	DA1		DA2		DA3		DA4	
	C	RMS	C	RMS	C	RMS	C	RMS
OBS	0.44	0.09	0.57	0.07	0.58	0.09	0.69	0.07
OBS-IBC	0.5	0.08	0.58	0.06				

Signal	DA3-DA1		DA4-DA2	
	C	RMS	C	RMS
IBC	0.5	0.05	0.58	0.05

Table 5.2: Mean sea level from model simulations and observations. C is correlation pattern coefficient; RMS is the root mean square error $[m]$. From top to bottom: tide-gauges full signal (OBS) compared with all the models simulations sea-level signals (Figure 5.4); inverse barometer correction applied to observations (OBS-IBC) and compared with model simulations (DA1 and DA2) where the the atmosheric pressure is not considered (Figure 5.5); inverse barometer correction (IBC) applied to the observations and subtracted from model simulations (DA3-DA1; DA4-DA2; Figure 5.6).

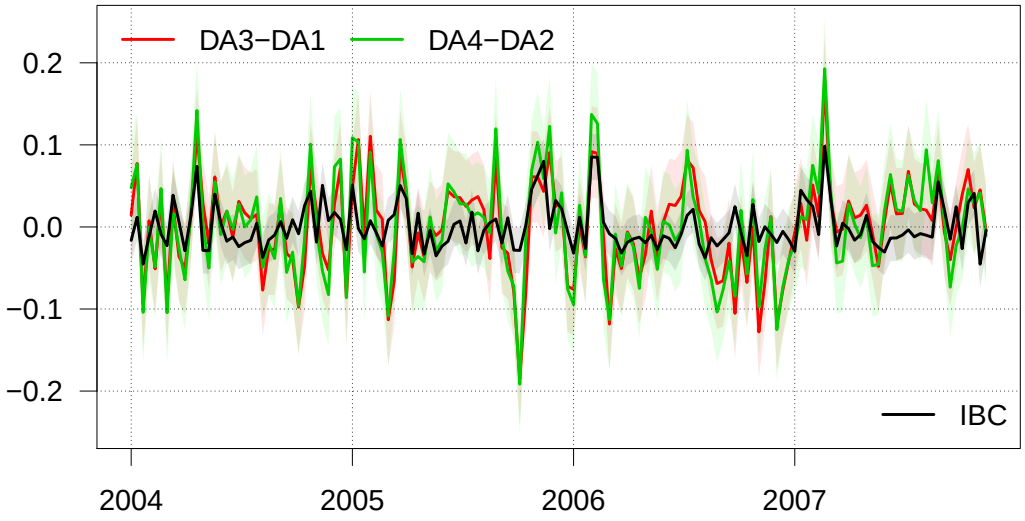

Figure 5.6: Inverse barometer effect applied to the tide-gauge stations (IBC; black line) and deducted from model simulations for the filtered free surface (DA3-DA1; red line) and time-splitting (DA4-DA2; green line) formulations. Shaded areas show the two standard deviation range.

Looking in detail at sea-sevel signal composition, we discuss below the results obtained performing a spectral analysis with all the datasets. Table 5.3 shows a summarized version of the results obtained. The power spectra of each tide-gauge station and of the model simulations sampled in the station posititions are shown in Figure 5.9.

In the observations only 30 % (0.11 m^2) of the variance is explained by the low temporal frequencies corresponding at 12, 6, and 4 months, while more than 40 % is explained by high frequency corresponding at 2 months (0.063 m^2) and 1 month (0.131 m^2). On the contrary, in DA1 and DA2 the 12-month oscillation explains most of the variance of the signal, 80 %, but with a different associated energy content: 0.51 m^2 in the DA1, and 0.28 m^2 in the DA2. In DA3 more than 60 % of variance is explained by the 12-, 6- and 4-month oscillations, but in this case too a certain energy amount is associated with high-frequency oscillations, accounting for 15 % of the variance.

Finally, DA4 has an energy content that is the most comparable with observations: 45 % of variance is associated with low frequencies oscillations (12, 6, 4 months), and almost 30 % with the 2-month (17 %) and 1-month (11 %) frequencies.

$Month^{-1}$	OBS		DA1		DA2		DA3		DA4	
	E	Var	E	Var	E	Var	E	Var	E	Var
12	0.07	16	0.51	80	0.28	81	0.467	55	0.263	39
6	0.011	3	0.003	~ 0	0.02	~ 0	0.03	3	0.021	3
4	0.029	11	0.015	2	0.04	1	0.046	5	0.032	5
2	0.063	14	0.018	3	0.012	3	0.086	10	0.112	17
1	0.131	30	0.007	1	0.01	3	0.04	5	0.075	11
Tot	0.304	70	0.55	86	0.307	88	0.67	78	0.503	75

Table 5.3: Observations and model power spectra (Figure 5.7 and 5.8). The table indicates the energy content (E) expressed in m^2, and the variance accounted (Var) as a pecentage (%), by the frequencies indicated in the first column ($Month^{-1}$).

The different sea-level signals have been compared, applying an 80-day low and high pass filter in order to separate the slow from the fast temporal scales.

Figure 5.7 shows the power spectrum of sea-level signals with the low pass filter applied and sea-level time series obtained considering only the low frequencies. Figure 5.8 shows the spectrum and time series considering only the residual high frequencies.

If we only consider the low-frequency signals (Figure 5.7), although the amplitude is overestimated by the model, the simulations are always highly correlated with the observations, reaching a maximum of ~ 0.8 in simulation DA4.

	Full		Low		High	
	C	RMS	C	RMS	C	RMS
DA1	0.44	0.09	0.55	0.08	0.50	0.05
DA2	0.57	0.07	0.67	0.05	0.66	0.05
DA3	0.58	0.09	0.65	0.07	0.57	0.05
DA4	0.69	0.07	0.78	0.05	0.61	0.05

Table 5.4: Model simulation and observation comparison in terms of mean sea level, where C is the correlation coefficient and RMS is the root mean square error . Column 1 and 2 (Full) refer to the comparison of the mean sea-level signal of observations and simulations, as shown in Figure 5.4. Columns 3 and 4 (Low) shown the results applying a high-frequencies band pass filter to the data (Figure 5.7). Columns 5 and 6 are the results obtained considering only the residual frequencies of the sea-level signals (Figure 5.8).

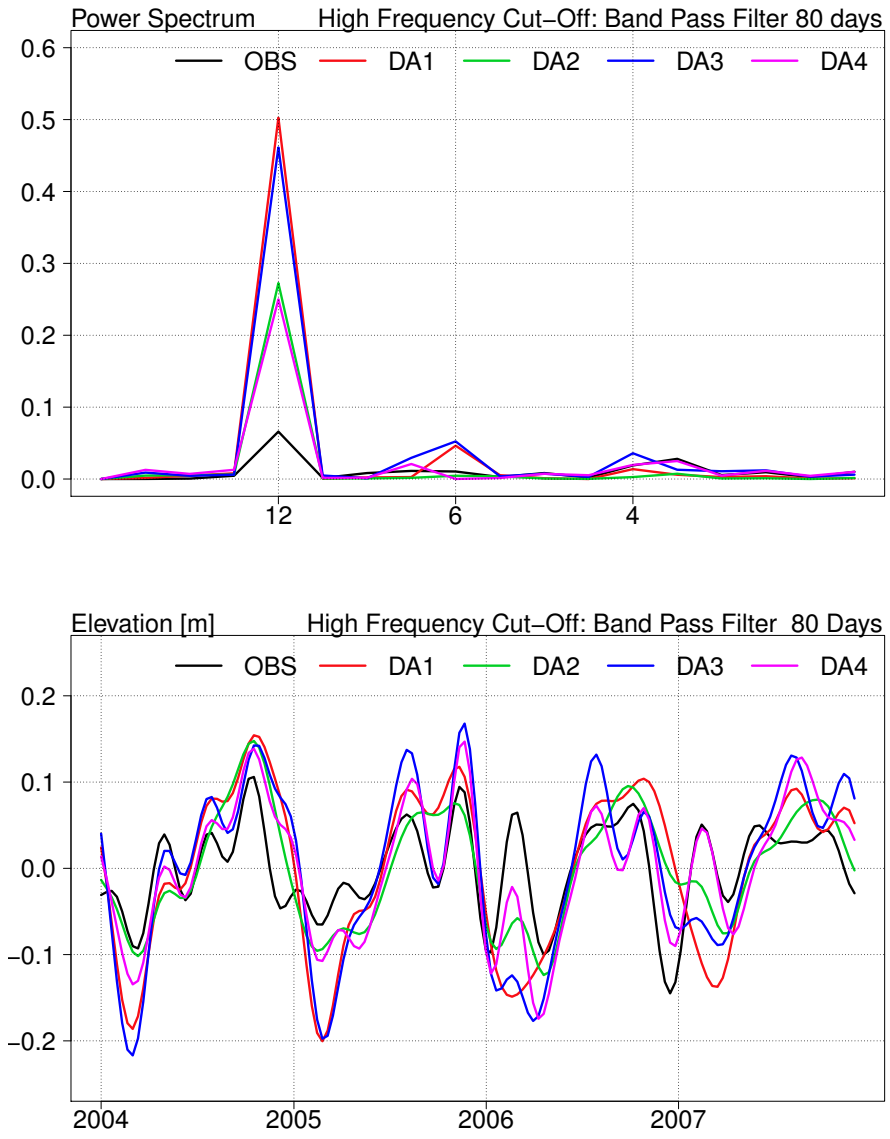

Figure 5.7: Spectral analysis. Top panel: datasets power spectrum, 80-day band pass filter applied. The x-axis is expressed in $months^{-1}$; x-axis indicating the frequency in $months^{-1}$; y-axis energy expressed in m^2. Bottom panel: sea-level signal obtained considering the low frequencies, shown in the top panel. Black solid line refers to the tide-gauge dataset; red (DA1), green (DA2), blue (DA3) and purple (DA4) lines are model simulation datasets.

Looking at the high-frequency signals (Figure 5.8), the amplitude and phase

of the signal is captured very well by DA3 and DA4, which tend underestimate the range of oscillation slightly. In all the cases analysed, the signals are highly correlated, to the order of > 0.5 (Table 5.4).

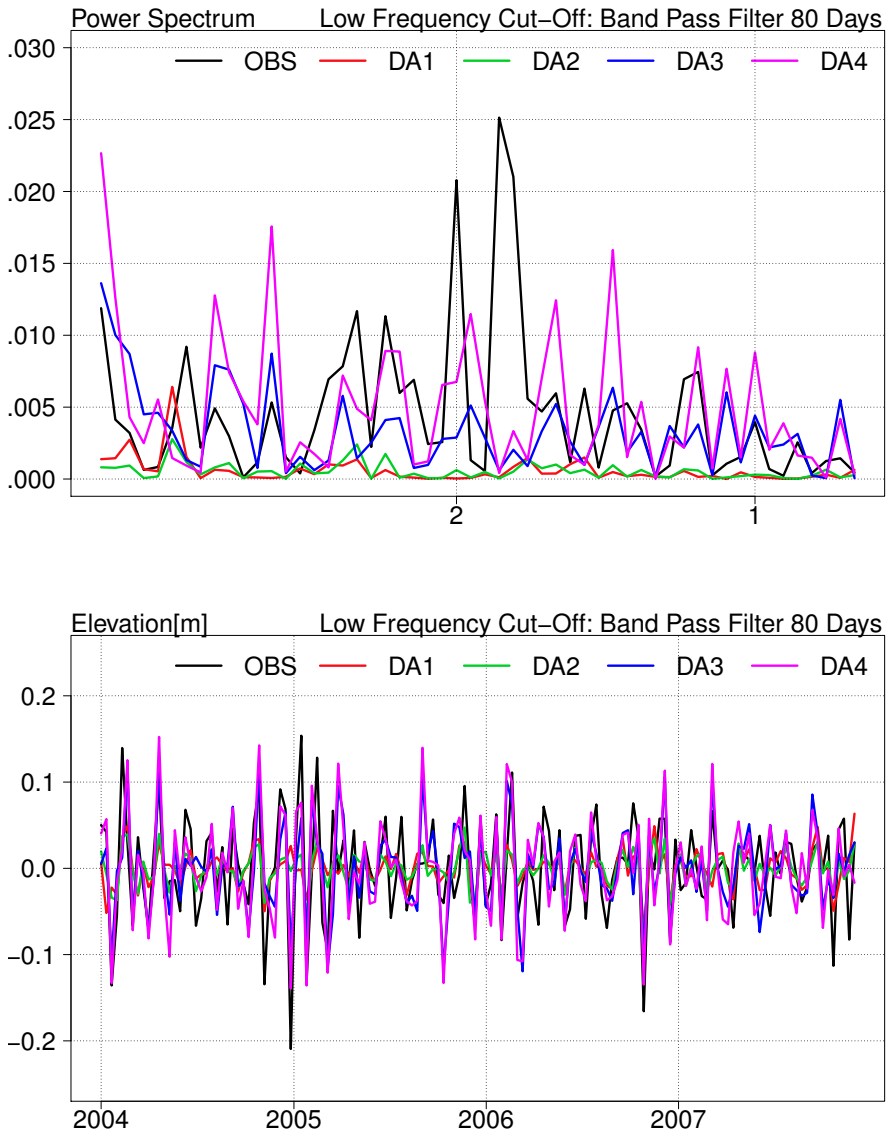

Figure 5.8: Spectral analysis. Top panel: datasets power spectrum, 80-day low pass filter applied. The x-axis indicating the frequency in $months^{-1}$; y-axis the energy expressed in m^2. Bottom panel: mean sea-level signal obtained considering only residual high frequencies shown in the top panel. Black solid line is the tide-gauge dataset, red line represents the DA1 dataset, green line DA2, blue line DA3 and purple line DA4.

The difference of the total energy contents of the simulations is higher for

DA4-DA3 (0.32 m^2) than for DA3 - DA1 (0.21 m^2). This indicates that the time-splitting formulation has slightly better capabilities for resolving the atmospheric effect on the sea-level signal of the OGCM used, probably because it allows a faster response of model variables to forcing variations.

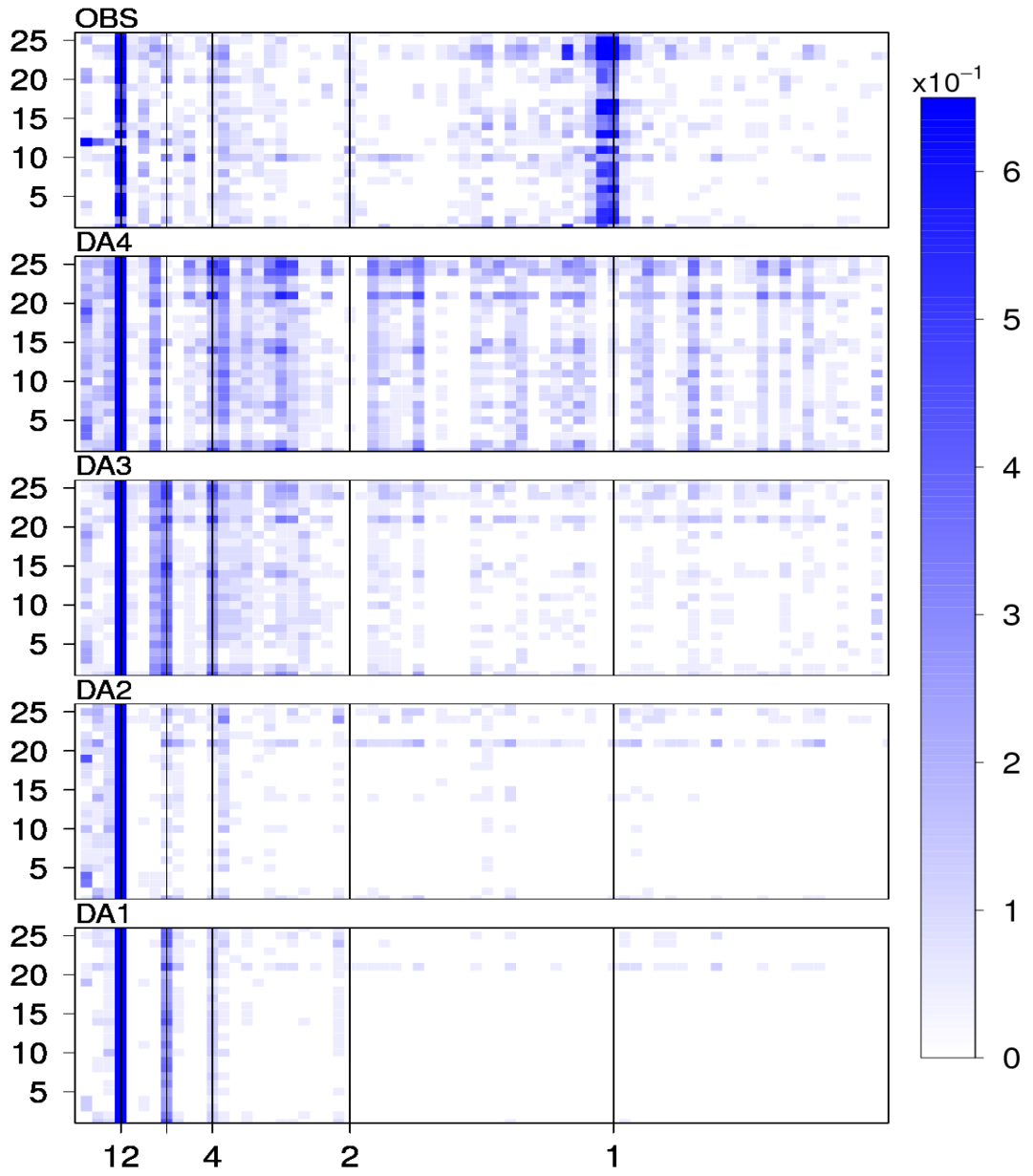

Figure 5.9: Observations and models power spectra. The first panel on the top (OBS) shows tide-guage observations. The others panels from top to bottom show models DA4, DA3, DA2 and DA1. Colours indicate energy expressed as m^2; the x-axis expresses the frequency in $months^{-1}$; the y-axis indicates the station number.

5.7 Summary

The model simulations and the experiments carried out represent a good analysis tool for investigating the atmospheric pressure contribution to the sea-level signal. The comparison with satellite altimetry data at basin scale show model simulations realism in reproduce the sea-level signal. The tide-gauge observations along the coasts of Italy and model simulation time series have been compared in terms of time evolution, amplitude and phase, separating the atmospheric contribution and signals composition (spectrum). The temporal resolution chosen for the data sampling results as being appropriate for achieving the objectives.

The atmospheric pressure effect on sea level represents a frequency-dependent process that acts over a short temporal scale and represents a source of energy for the sea-level signal.

The simulations that adopt the filtered free-surface formulation, filtering out fast temporal-scale processes, have an inferior capability for reproducing the full sea-level signal (DA1), which tends to improve considering atmospheric forcing (DA3) but does not add energy to the smaller time scales.

The simulations that consider time-splitting as a free-surface formulation show a higher skill in capturing the sea-level signal (DA2), but only the combination with surface pressure forcing is capable of adding energy at 1- and 2-month time scales (DA4). Table 5.3 shows that the atmospheric contribution adds energy to the fast frequencies (2-month and 1-month processes), which allows the model (DA4) to reproduce the sea-level signals of the observations better, the energy of which is 30 % explained by high-frequency processes (Table 5.3).

The energy difference between experiments DA4 and DA2 and the difference between DA3 and DA2 indicate that the time-splitting formulation is more capable of capturing the atmospheric pressure effect on the sea-level signal of the Mediterranean Sea.

Chapter 6

Conclusions and future perspectives

In this work, sea-level climate variability has been studied starting from all the most updated observational datasets (tide gauges, satellite altimetry, satellite gravimetry), high-resolution numerical ocean models and ocean re-analysis data. In order to understand in detail the composition of the sea-level signals captured by each data source, specific analysis methods have been developed (Chapter 2) and applied (Chapter 3) to each dataset. The analysis carried out, considered as a whole, allows the quantification of specific contributions (i.e., Chapter 5) to sea-level tendency, trend and time evolution, approaching these issues from decadal (Chapter 2) to centennial (Chapter 3) temporal scales, and from regional (Chapter 4) to local (Chapter 2) spatial scales Low-frequency sea-level variability over a decadal time scale is recorded in a similar way from in-situ and satellite altimetry instruments (comparing the data as coherent signals) in the areas where the continental shelf is the most extended in the Mediterranean (i.e., the Adriatic). The sea-level trend has marked spatial variability, with high positive rates in the Aegean and part of the Levantine basin and the Northern Adriatic, and negative trends in the Ionian Sea. The mean sea-level trend also has a high variability if we consider less than 15 years of data ($2.17 \pm 0.7\ mm\ \ yr^{-1}$ between 1993 and 2010). Over a centennial time period, on the other hand, the trend distribution shows positive rates over the whole basin (except the Ionian). Considering the mean sea-level trend, which results as being stable in the basin if we consider a time period longer than 90 years, shows that no significant trend ($0.1 \pm 0.1\ mm\ \ yr^{-1}$)

is present during the period from 1885 to 2010. The mean sea-level tendency in the Mediterranean basin (from 1985 to 2007) result as being a high-frequency signal ($10^3\ mm\ yr^{-1}$) resulting from the mass and steric contribution variations . The thermosteric component is typically periodic, while the halosteric has an inferior order of magnitude if compared with the others. The mass contribution, divided between water flux and transport at Gibraltar, has the highest orders of magnitude: the delay in the balance of these two processes is at the base of the sea-level stochastic variations that add complexity and uncertainty to the sea-level dynamic. In order to account for the high frequency of the sea-level tendency signal, it is necessary to consider records at a high temporal resolution: it is thus possible to minimize the numerical error that can arise integrating in time the mean sea-level tendency components in order to obtain the mean sea-level time evolution.

One of the main drivers of the Mediterranean ocean dynamic is the NAO. These processes influence the sea level, inducing freshwater flux variations and sea-level pressure anomalies through the inverse barometer effect.

The sea-level response to the atmospheric pressure variations assumes a fundamental importance when low pressure cells establish rapidly, representing the initial phase of the extreme events dynamic. The approach based on numerical models used in Chapter 5 is a valid instrument for quantifying sea-level anomalies associated with atmospheric pressure variations, in terms of both sea-surface elevation and sea-level signal energy.

In general, the methods developed and the analysis performed during this work allow us to understand sea-level variability over long temporal scales, permitting a description of each components contribution to the sea-level signal. This represents a strategy for facing the uncertainties associated with the response of sea-level contributions to climate change.

One of the limits of this study is represented by the total lack of data in the southern part of the basin, which affects the significance of sea-level studies in the Mediterranean basin. Over recent years a new coastal satellite altimetry dataset (Vignudelli *et al.*, 2011) has been calibrated that could in the near future be used to cover this data gap in the Mediterranean; it will in general provide unique information about sea-level coastal dynamics.

Looking at the importance of these processes for understanding sea-level variability over short to medium temporal scales (hourly to daily) in coastal areas, we will in the future focus on sea-level interaction with atmospheric forcings (pressure and winds) and waves, in particular during extreme events, to develop the scientific knowledge to be applied in a future advanced coastal risk management system.

Appendix A

Tide gauge stations in the Mediterranean sea

All the the tide-gauge stations data used in this work are distributed by Permanent Service for Mean Sea Level (PSMSL) as part of the Revised Local Reference (RLR) dataset (Woodworth & Player, 2003). Figure A.1 shows the distribution of tide-gauge stations in the Mediterranean basin. The data are available as annual and monthly means, and time series are reduced to a common datum using tide-gauge datum history provided by the supplying authority. Without the provision of full benchmark datum history information, records are defined as Metric and not as RLR. As reported by PSMSL, detailed relationships at each site between RLR datum, benchmark heights and tide-gauge zero are not normally required by analysts of the dataset, but these are available for most station from the individual station pages. Benchmarks of each tide-gauge station considered are given in Table A.1 (last column). Further documentation about PSMSL data and RLR dataset is available on PSMSL web portal: *http://www.psmsl.org*.

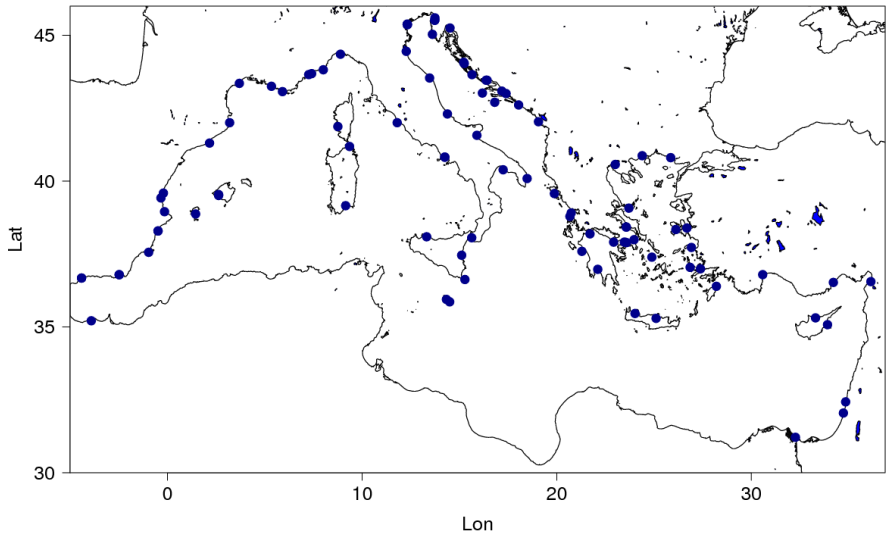

Figure 1: Revised Local Reference tide gauge stations distribution in the Mediterranean basin.

	code	lon	lat	range	years	n.years	complete	benchmark
PORTO CORSINI	270/35	12.28	44.5	1969-1972	4	4	94	-7.9
KOPER	279/2	13.75	45.57	1962-1991	30	29	96	-8.9
ANCONA	270/30	13.48	43.58	1966-1972	7	6	74	-8.6
CATANIA	260/31	15.13	37.5	1960-1971	12	12	100	-11.7
TARANTO	270/6	17.27	40.43	1906-1911	6	6	100	-11.8
CAGLIARI	240/11	9.17	39.2	1896-1934	39	37	93	+7.9
NAPOLI (MANDRACCIO)	250/51	14.27	40.87	1896-1922	27	26	93	-9.5
CIVITAVECCHIA	250/31	11.82	42.05	1896-1922	27	26	94	+11.4
PALERMO	260/11	13.33	38.13	1896-1922	27	25	91	-7.7
BAR	281/11	19.08	42.08	1964-1991	28	27	95	-10.4
PORTO MAURIZIO	250/1	8.02	43.87	1896-1922	27	26	95	-7.6
PALMA	225/1	2.63	39.58	1964-1966	3	3	97	-6.1
LA MADDALENA	240/1	9.37	41.23	1896-1913	18	16	89	-7.7
SOUDHAS	290/97	24.05	35.5	1969-2001	33	32	94	-10.2
LEROS	290/91	26.88	37.08	1969-2010	42	34	79	-9.2
SIROS	290/81	24.92	37.43	1969-2010	42	25	58	-9.2
KHALKIS NORTH	290/34	23.6	38.47	1969-2010	42	37	88	-8.7
ALEXANDROUPOLIS	290/65	25.88	40.85	1969-2010	42	37	88	-9.1
LEVKAS	290/4	20.7	38.83	1969-2010	42	36	84	-8.1
KATAKOLON	290/17	21.32	37.63	1969-2010	42	38	89	-9.6
RODHOS	290/110	28.23	36.43	1969-2010	42	30	69	-8.4
PATRAI	290/14	21.73	38.23	1969-2006	38	33	86	-9.9
MANFREDONIA	270/19	15.92	41.62	1969-1971	3	3	97	-8.9
NAPOLI (ARSENALE)	250/41	14.27	40.87	1899-1922	24	22	91	-8.1
KHALKIS SOUTH	290/33	23.6	38.47	1977-2010	34	27	79	-9.3
ALMERIA	220/41	-2.48	36.83	1977-1997	21	19	89	-
CARTAGENA	220/46	-0.97	37.6	1977-1987	11	10	84	-13.5
NICE	230/81	7.27	43.7	1978-2010	33	29	87	-8.7

TRIESTE	270/61	13.76	45.65	1905-2010	106	100	94	-9.4
VIS-CESKA VILA	280/40	16.2	43.07	1983-1991	9	9	90	-12.6
GAZENICA	280/14	15.27	44.08	1983-1988	6	6	100	-10.1
ZLARIN	280/17	15.67	43.7	1983-1988	6	6	90	-9.3
NORTH SALAMINOS	290/30	23.5	37.95	1984-2000	17	16	89	-8.5
MENTES/IZMIR	310/42	26.72	38.43	1985-2009	25	22	87	-8.7
VENEZIA (PUNTA DELLA SALUTE)	270/54	12.33	45.43	1909-2000	92	87	94	-6.8
BODRUM II	310/46	27.42	37.03	1985-2009	25	21	80	-8.6
ANTALYA II	310/52	30.62	36.83	1985-2009	25	22	85	-7.4
RAFINA	290/32	24	38.03	1986-1989	4	4	96	-10.5
SUCURAJ	280/46	17.2	43.13	1987-2005	19	19	97	-9.7
UBLI	280/56	16.83	42.75	1987-1991	5	5	93	-9.8
VALLETTA	265/1	14.52	35.9	1988-2009	22	20	89	-9.8
L'ESTARTIT	220/81	3.2	42.05	1990-2001	12	12	100	-7
HADERA	320/16	34.88	32.47	1992-2008	17	15	85	-11
MALAGA II	220/32	-4.42	36.72	1992-2009	18	18	95	-7.6
BARCELONA	220/61	2.17	41.35	1992-2007	16	15	92	-9.2
VALENCIA	220/56	-0.33	39.47	1992-2005	14	12	85	-8.7
LUKA KOPER	279/3	13.75	45.57	1992-2003	12	11	92	-
ZADAR	280/13	15.23	44.12	1994-2008	15	15	96	-
TEL AVIV	320/19	34.77	32.08	1996-2009	14	12	86	-9.9
PALMA DE MALLORCA	225/11	2.63	39.55	1997-2009	13	13	94	-6.3
SKOPELOS	290/37	23.73	39.12	1999-2009	11	8	73	-8.7
GIRNE	315/10	33.33	35.35	2000-2003	4	3	58	-
MELLIEHA BAY	265/2	14.35	35.98	2000-2001	2	1	50	-9.9
AJACCIO	232/1	8.77	41.92	2003-2010	8	6	68	-
IBIZA	225/21	1.45	38.92	2003-2009	7	7	98	6.7
CORFU CITY	290/103	19.9	39.62	2004-2010	7	6	85	1.6
SAMOS ISLAND - VATHI	290/105	26.95	37.77	2005-2010	6	6	85	0.4
PLOCE	280/75	17.42	43.05	2006-2008	3	3	100	-4.5

ERDEMLI	310/71	34.25	36.57	2003-2009	7	7	92	-8.7
ISKENDERUN II	310/66	36.18	36.59	2005-2009	5	5	100	-7.6
ALMERIA 2	220/44	-2.48	36.83	2006-2009	4	4	96	3.9
GANDIA	220/58	-0.15	38.99	2007-2009	3	3	78	1.8
SAGUNTO	220/60	-0.21	39.63	2007-2009	3	3	78	3.8
ALICANTE I	220/51	-0.48	38.33	1952-1996	45	32	70	-10.4
PORT SAID	330/1	32.3	31.25	1923-1946	24	24	100	-8.3
SPLIT - GRADSKA LUKA	280/31	16.44	43.51	1954-2008	55	55	100	-10.4
BAKAR	280/11	14.53	45.3	1930-2008	79	68	86	-9.7
THESSALONIKI	290/51	23.03	40.62	1969-2010	42	38	90	-9.2
PIRAIEVS	290/31	23.62	37.93	1969-2002	34	26	76	-21.5
KAVALLA	290/61	24.42	40.92	1969-2010	42	35	82	-8.4
VENEZIA (S.STEFANO)	270/51	12.33	45.42	1872-1920	49	48	98	-9.9
KHIOS	290/71	26.15	38.38	1969-2010	42	38	88	-8.9
POSIDHONIA	290/11	22.95	37.95	1969-2010	42	31	73	-8.6
PREVEZA	290/1	20.77	38.95	1969-2010	42	32	74	-9.3
KALAMAI	290/21	22.13	37.02	1969-2010	42	33	78	-9.5
FAMAGUSTA	315/1	33.95	35.12	1938-1940	3	3	75	-9.1
MALAGA	220/31	-4.42	36.72	1944-2009	66	55	82	-8.1
VILLA SANJURJO	340/4	-3.92	35.25	1944-1949	6	6	99	-9.2
GENOVA	250/11	8.9	44.4	1884-1997	114	90	78	-10.2
MARSEILLE	230/51	5.35	43.3	1885-2010	126	122	97	-8.5
IRAKLION	290/101	25.13	35.33	1984-2010	27	21	75	-8.7
REGGIO CALABRIA	250/61	15.65	38.1	1951-1967	17	14	81	-9.5
SPLIT RT MARJANA	280/21	16.39	43.51	1952-2008	57	57	99	-9.5
DUBROVNIK	280/81	18.06	42.66	1956-2008	53	53	99	-11.3
ROVINJ	280/6	13.63	45.08	1955-2008	54	54	99	-11.9
MONACO (CONDAMINE)	233/11	7.42	43.73	1956-2010	55	20	35	-8.5
VENEZIA (ARSENALE)	270/41	12.35	45.42	1889-1913	25	24	96	-10.5
CAPO PASSERO	260/28	15.3	36.67	1957-1969	13	12	89	-10.6

SETE	230/21	3.7	43.4	1996-2010	15	13	87	-8.7
ALICANTE II	220/52	-0.48	38.33	1960-1997	38	37	97	-10.4
ORTONA	270/26	14.4	42.35	1960-1972	13	7	48	-8.6
TOULON	230/61	5.92	43.12	1961-2010	50	26	52	-10.5
OTRANTO	270/11	18.5	40.13	1961-1970	10	4	40	-9.6

Table 1: Tide gauge stations RLR in the Mediterranean sea, with time series that span a period longer 100 years. Columns 4 ad 5 express the period and the number of years covered by the station data. Columns 6 and 7 show the amout of data available once rmoved the missing data as numbers of yeasr and percentage (%) respectively.Column 8 indicates tide-gauges benchmarks $[m]$.

References

Adani, M., Dobricic, S., & Pinardi, N. 2010. Quality assessment of a 1985-2007 mediterranean sea re-analysis. *Submitted.* 3, 58, 63, 68, 70

Apel, J.R. 1987. *Principles of ocean physics.* Vol. 38. Academic Pr. 59

AVISO, Altimetry. 2010. *Ssalto/duacs user handbook:(m) sla and (m) adt near-real time and delayed time products.* Tech. rept. viii, 12

Bindoff, N.L., Willebrand, J., Artale, V., Cazenave, A., Gregory, J.M., Gulev, S., Hanawa, K., Le Quéré, C., Levitus, S., Nojiri, Y., *et al.* 2007. Observations: oceanic climate change and sea level. 1, 30

Bjornsson, H., & Venegas, S. A. 1997. A manual for eof and svd analyses of climatic data. *Centre for climate and global change research, mcgill university.* 35

Cabanes, C., Cazenave, A., & Provost, C. Le. 2001. Sea level rise during past 40 years determined from satellite and in situ observations. *Science*, **294**(5543), 840–2. 3, 6

Calafat, F. M., & Gomis, D. 2009. Reconstruction of mediterranean sea level fields for the period 1945–2000. *Global and planetary change*, **66**(3-4), 225. 2, 7, 31, 35, 36, 54

Calafat, FM, & Jordà, G. 2011. A mediterranean sea level reconstruction (1950–2008) with error budget estimates. *Global and planetary change.* 31, 32, 38, 55

Candela, J. 1991. The gibraltar strait and its role in the dynamics of the mediterranean sea. *Dynamics of atmospheres and oceans*, **15**(3-5), 267–299. 73

Cartwright, D. E., & Edden, A. C. 1973. Corrected tables of tidal harmonics. *Geophysical journal of the royal astronomical society*, **33**(3), 253–264. 12

Cash, J.R., & Karp, A.H. 1990. A variable order runge-kutta method for initial value problems with rapidly varying right-hand sides. *Acm transactions on mathematical software (toms)*, **16**(3), 201–222. 66

Cazenave, A., & Llovel, W. 2010. Contemporary sea level rise. *Annual review of marine science*, **2**, 145–173. 57

Cazenave, A., Cabanes, C., Dominh, K., & Mangiarotti, S. 2001. Recent sea level change in the mediterranean sea revealed by topex/poseidon satellite altimetry. *Geophysical research letters*, **28**(8), 1607–1610. 7

Cazenave, A., Bonnefond, P., Mercier, F., Dominh, K., & Toumazou, V. 2002. Sea level variations in the mediterranean sea and black sea from satellite altimetry and tide gauges. *Global and planetary change*, **34**(1-2), 59–86. 7

Cazenave, A., Cabanes, C., Dominh, K., Gennero, M. C., & Le Provost, C. 2003. Present-day sea level change: Observations and causes. *Space science reviews*, **108**(1), 131–144. 6

Church, J., Woodworth, P.L., Aarup, T., & Wilson, S. 2010. *Understanding sea-level rise and variability*. Wiley-Blackwell. 2, 3, 30

Church, J. A., & White, N. J. 2011. Sea-level rise from the late 19th to the early 21st century. *Surveys in geophysics*, 1–18. 2, 31

Church, J. A., White, N. J., Coleman, R., Lambeck, K., & Mitrovica, J. X. 2004a. Estimates of the regional distribution of sea level rise over the 1950–2000 period. *Journal of climate*, **17**(13), 2609–2625. 5, 31, 35

Church, J.A., White, N.J., Coleman, R., Lambeck, K., & Mitrovica, J.X. 2004b. Estimates of the regional distribution of sea level rise over the 1950-2000 period. *Journal of climate*, **17**(13), 2609–2625. 32, 37, 38, 54

Church, John A. 2006. A 20th century acceleration in global sea-level rise. *Geophysical research letters*, **33**(1), –01602. 6, 31

Cushman-Roisin. 1994. *Introduction to geophysical fluid dynamics*. Prentice Hall, 200 pp. 60

Demirov, E., & Pinardi, N. 2002. Simulation of the mediterranean sea circulation from 1979 to 1993: Part i. the interannual variability. *Journal of marine systems*, **33**, 23–50. 7, 25

Domingues, C. M., Church, J. A., White, N. J., Gleckler, P. J., Wijffels, S. E., Barker, P. M., & Dunn, J. R. 2008. Improved estimates of upper-ocean warming and multi-decadal sea-level rise. *Nature*, **453**(7198), 1090–1093. 5

Dorandeu, J., & Le Traon, P. Y. 1999a. Effects of global mean atmospheric pressure variations on mean sea level changes from topex/poseidon. *Journal of atmospheric and oceanic technology*, **16**(9), 1279–1283. 16

Dorandeu, J., & Le Traon, P. Y. 1999b. Effects of global mean atmospheric pressure variations on mean sea level changes from topex/poseidon. *Journal of atmospheric and oceanic technology*, **16**(9), 1279–1283. 73, 78

Douglas, B. C., & Peltier, W. R. 2002. The puzzle of global sea-level rise. *Physics today*, **55**(3), 35–41. 6

Ducet, N., Traon, P. Y. Le, & Reverdin, G. 2000. Global high-rp:esolution mapping of ocean circulation from topex/poseidon and ers-1 and-2. *Journal of geophysical research-oceans*, **105**(C8). 10, 11, 17

EEA. 2011. *Sea level rise indicator fact sheet*. Tech. rept. European Environmental Agency. 2

Garcia, D., Chao, B. F., Del R, J., Vigo, I., & Lafuente, J. G. 2006. On the steric and mass-induced contributions to the annual sea level variations in the mediterranean sea. *J. geophys. res*, **111**. 15

Garcia, D., Chao, B. F., & Boy, J. P. 2010. Steric and mass-induced sea level variations in the mediterranean sea revisited. *Journal of geophysical research*, **115**(C12), –12016. 15

Gill, A.E. 1982. *Atmosphere-ocean dynamics*. Vol. 30. Academic Press. 58

Gomis, D., Ruiz, S., Sotillo, M., AlvarezFanjul, E., & Terradas, J. 2008. Low frequency mediterranean sea level variability: The contribution of atmospheric pressure and wind. *Global and planetary change*, **63**(2-3), 215. 6

Greatbatch, R. J. 1994. A note on the representation of steric sea level in models that conserve volume rather than mass. *Journal of geophysical research*, **99**(C6), 12767–12. 14, 57, 63

Griffies, S.M. 2004. *Fundamentals of ocean climate models*. Vol. 518. Princeton University Press Princeton,, USA. 76

Holgate, S. J. 2004. Evidence for enhanced coastal sea level rise during the 1990s. *Geophysical research letters*, **31**(7), –07305. 5

Hurrell, J. W., & Deser, C. 2009. North atlantic climate variability: The role of the north atlantic oscillation. *Journal of marine systems*, **78**(1), 28–41. vi, 72, 75

Hurrell, J.W. 1995. Decadal trends in the north atlantic oscillation: regional temperatures and precipitation. *Science*, **269**(5224), 676. 72

IPCC. 2007. Oceanic climate change and sea level. *Intergovernamentatl panel for climate change*, **Fourth Assessment Report**, –5. 57

Kalnay, E., Kanamitsu, M., Kistler, R., Collins, W., Deaven, D., Gandin, L., Iredell, M., Saha, S., White, G., Woollen, J., *et al.* 1996. The ncep/ncar 40-year reanalysis project. *Bulletin of the american meteorological society*, **77**(3), 437–471. 73

Kaplan, A., Kushni, Y., Cane, M.A., & Blumenthal, M.B. 1997. Reduced space optimal analysis for historical data sets: 136 years of atlantic sea surface temperatures. *Journal of geophysical research-all series-*, **102**, 27–27. 34, 54

Kaplan, A., Kushnir, Y., & Cane, M. A. 2000. Reduced space optimal interpolation of historical marine sea level pressure: 1854–1992. *Journal of climate*, **13**(16), 2987–3002. 30, 35, 36, 37

Klein, M., & Lichter, M. 2009. Statistical analysis of recent mediterranean sea-level data. *Geomorphology*, **107**(1-2), 3–9. 7, 9

Le Traon, P.Y., & Gauzelin, P. 1997. Response of the mediterranean mean sea level to atmospheric pressure forcing. *Journal of geophysical research*, **102**(C1), 973–984. 73

Leuliette, E. W., Nerem, R. S., & Mitchum, G. T. 2004. Calibration of topex/poseidon and jason altimeter data to construct a continuous record of mean sea level change. *Marine geodesy*, **27**(1), 79–94. 6

Levitus, S., Antonov, J. I., Boyer, T. P., & Stephens, C. 2000. Warming of the world ocean. *Science*, **287**(5461), 2225. 5

Liebmann, B., Dole, R. M., Jones, C., Bladé, I., & Allured, D. 2010. Influence of choice of time period on global surface temperature trend estimates. *Bulletin of the american meteorological society*. 26, 27, 50

Madec, G. 2008. Nemo ocean engine. 75

Marcos, M., & Tsimplis, M. N. 2007. Forcing of coastal sea level rise patterns in the north atlantic and the mediterranean sea. *Geophysical research letters*, **34**(18), –18604. 2, 6, 73

Marcos, M., & Tsimplis, M. N. 2008. Coastal sea level trends in southern europe. *Geophysical journal international*, **175**(1), 70–82. 7

Marshall, J., & Plumb, R. A. 2008. *Atmosphere ocean and climate dynamics*. Vol. 1. 61

Masina, S., Di Pietro, P., & Navarra, A. 2004. Interannual-to-decadal variability of the north atlantic from an ocean data assimilation system. *Climate dynamics*, **23**(5), 531–546. 3

Mellor, G. L., & Ezer, T. 1995. Sea level variations induced by heating and cooling: An evaluation of the boussinesq approximation in ocean models. *Journal of geophysical research-all series-*, **100**, 20–20. 13, 14, 58, 63, 79

Meyssignac, B., Calafat, F. M., Somot, S., Rupolo, V., Stocchi, P., Llovel, W., & Cazenave, A. 2011. Two-dimensional reconstruction of the mediterranean sea level over 1970-2006 from tide gauge data and regional ocean circulation model outputs. *Global and planetary change*. 31, 34, 54

Munk, W. 2002. Twentieth century sea level: An enigma. *Proceedings of the national academy of sciences*, **99**(10), 6550. 3

Nicholls, R. J., & Mimura, N. 1998. Regional issues raised by sea-level rise and their policy implications. *Climate research*, **11**, 5–18. 2

Nichols, R. 2004. Coastal flooding and wetland loss in the 21st century: changes under the sres climate and socio-economic scenarios. *Global environmental change*, **14**(1), 69. 2

Oddo, P., Adani, M., Pinardi, N., Fratianni, C., Tonani, M., & Pettenuzzo, D. 2009. A nested atlantic-mediterranean sea general circulation model for operational forecasting. *Ocean science*, **5**, 461–473. 3, 66, 68, 73, 75, 76

Pedlosky, J. 1987. *Geophysical fluid dynamics*. Springer. 58, 61

Pettenuzzo, D., Large, WG, & Pinardi, N. 2010. On the corrections of era-40 surface flux products consistent with the mediterranean heat and water budgets and the connection between basin surface total heat flux and nao (doi 10.1029/2009jc005631). *Journal of geophysical research*, **115**(6). 72, 75

Pinardi, N., & Coppini, G. 2010. Operational oceanography in the mediterranean sea: the second stage of development. *Ocean sci*, **6**, 263–267. 73

Pinardi, N., Allen, I., Demirov, E., de Mey, P., Korres, G., Lascaratos, A., Le Traon, P. Y., Maillard, C., Manzella, G., & Tziavos, C. 2003. The mediterranean ocean forecasting system: first phase of implementation (1998-2001). **21**, 3–20. 75

Pinardi, N., Zavatarelli, M., Crise, A., & Ravioli, M. 2005. *The sea*. Vol. 14. 18, 25

Ponte, R.M., Salstein, D.A., & Rosen, R.D. 1991. Sea level response to pressure forcing in a barotropic numerical model. *Journal of physical oceanography*, **21**(7), 1043–1057. 72

Pujol, M. I., & Larnicol, G. 2005. Mediterranean sea eddy kinetic energy variability from 11 ys of altimetric data. *Journal of marine systems*, **58**(3-4), 121–142. 3, 10, 13, 19, 34

Richman, M.B. 1986. Rotation of principal components. *Journal of climatology*, **6**(3), 293–335. 43

Roullet, G., & Madec, G. 2000. Salt conservation, free surface, and varying levels: a new formulation for ocean general circulation models. *J. geophys. res*, **105**(23), 927–23. 76

Sanchez-Arcilla, A., & Simpson, J. H. 2002. The narrow shelf concept: couplings and fluxes. *Continental shelf research*, **22**(2), 153–172. 18

Somot, S., Sevault, F., & Déqué, M. 2006. Transient climate change scenario simulation of the mediterranean sea for the twenty-first century using a high-resolution ocean circulation model. *Climate dynamics*, **27**(7), 851–879. 73

Sotillo, MG, Ratsimandresy, AW, Carretero, JC, Bentamy, A., Valero, F., & Gonzalez-Rouco, F. 2005. A high-resolution 44-year atmospheric hindcast for the mediterranean basin: contribution to the regional improvement of global reanalysis. *Climate dynamics*, **25**(2), 219–236. 73

Spada, G., Antonioli, A., Cianetti, S., & Giunchi, C. 2006. Glacial isostatic adjustment and relative sea-level changes: the role of lithospheric and upper mantle heterogeneities in a 3-d spherical earth. *Geophysical journal international*, **165**(2), 692–702. 1

Stocchi, P., & Spada, G. 2009. Influence of glacial isostatic adjustment upon current sea level variations in the mediterranean. *Tectonophysics*, **474**(1-2), 56–68. 34

Storch, H. Von, & Zwiers, F. W. 1999. *Statistical analysis in climate research, 484 pp.* Cambridge University Press Cambridge. 35

Traon, P. Y. Le, Nadal, F., & Ducet, N. 1998. An improved mapping method of multisatellite altimeter data. *Journal of atmospheric and oceanic technology*, **15**(2), 522–534. 10

Traon, P. Y. Le, Faugère, Y., Hernandez, F., Dorandeu, J., Mertz, F., & Ablain, M. 2003. Can we merge geosat follow-on with topex/poseidon and ers-2 for an improved description of the ocean circulation? *Journal of atmospheric and oceanic technology*, **20**(6). 10

Tsimplis, M. N., Álvarez-Fanjul, E., Gomis, D., Fenoglio-Marc, L., & Pérez, B. 2005. Mediterranean sea level trends: atmospheric pressure and wind contribution. *Geophysical research letters*, **32**(20), –20602. 6, 73

Tsimplis, MN. 1995. The response of sea level to atmospheric forcing in the mediterranean. *Journal of coastal research*, 1309–1321. 73

Tsimplis, M.N., & Josey, S.A. 2001. Forcing of the mediterranean sea by atmospheric oscillations over the north atlantic. *Geophys. res. lett*, **28**(5), 803–806. 72

Vignudelli, S., Cipollini, P., Gommenginger, C., Gleason, S., Snaith, H. M., Coelho, H., Fernandes, M. J., Lázaro, C., Nunes, A. L., Gómez-Enri, J., *et al.* 2011. Satellite altimetry: sailing closer to the coast. *Remote sensing of the changing oceans*, 217. 94

Wahr, J. W. 1985. Deformation of the earth induced by polar motion. *J. geophys. res*, **90**, 9363–9368. 12

Woodworth, P. L., & Player, R. 2003. The permanent service for mean sea level: an update to the 21 st century. *Journal of coastal research*, **19**(2), 287–295. 9, 32, 96